ROMA TRE
UNIVERSITÀ DEGLI STUDI

Università degli Studi "Roma Tre"

Facoltà di Scienze Matematiche, Fisiche e Naturali
Dottorato di ricerca in Fisica - XXV Ciclo

Accreting Black Holes during cosmic time

Gabriele Melini

Relatore interno
Prof. Fabio La Franca

Relatore esterno
Dr. Fabrizio Fiore
INAF-OAR

*"Now the sky,
it shines a different
kind of blue"*

Contents

Chapter 1

Introduction

1.1 Black Holes and Cosmology

The study of astrophysical black holes (BH) is mainly driven by three different rationales. First of all, the existence of this kind of objects is one of the strongest implications of the theory of General Relativity, and their study can give useful information on strong gravity effects in action.

Secondly, the emission processes, which allow us to detect such a kind of sources, originate from accretion flows or relativistic jets. Both of these mechanisms take place in regions very close to the BH, thus allowing to study not only the physics of matter in extreme conditions, but also radiative effects and relativistic magnetohydrodinamics.

Lastly, BH affect the formation and evolution of the structures they live in, like galaxies, groups and clusters, and therefore play a key role in a broader cosmological context.

This tight link between BH activity and galaxy evolution has been indicated by several discoveries:

- the observation of a supermassive BH (SMBH) in most of the nearby bulge-dominated galaxies (see e.g. Gebhardt et al. 2000; Ferrarese &

Merritt 2000; Marconi & Hunt 2003, and references therein);

- the growth of SMBH happen mainly during active phases, and therefore most local bulge galaxies should have passed an active phase in their lifetime (see Soltan 1982; Marconi et al. 2004);

- the evolution of active BH (Ueda et al. 2003; Hasinger, Miyaji & Schmidt 2005; La Franca et al. 2005) and of star-forming galaxies (Cowie et al. 1996; Franceschini et al. 1999) have a very similar shape.

Models constrained from evolving optical and X-ray luminosity functions gave encouraging results, predicting some of the observed trends in AGN. However, the overestimation of the space density of low-luminosity sources, along with other observational evidences, suggest that a significant fraction of accreting BH (as high as 50%) is missed by current surveys.

All these pieces of evidence imply that the realization of a complete census of accreting black holes and constraining their *feedback* action on the host galaxies are key steps towards the understanding of the galaxy formation and evolution.

1.2   Thesis Outline

This Ph.D. Thesis is devoted to the study of accreting BH from a cosmological point of view, and is organized as follows. A brief introduction on AGN structure and evolution is given in Chapter 2. In Chapter 3 the creation of the two main data sets used in the following works is discussed, and the two final samples are presented.

In Chapter 4 a measure of the probability distribution function of the *radio loudness* of AGN is present. I have worked on this topic during the first months of my Ph.D. work.

The main subject that I have dealt with is the measure of the density of highly obscured AGN from mid-infrared selected samples, that is discussed in Chapter 5.

Since this analysis has been performed after the measure of the probability distribution function discussed in Chapter 4, we were not able to include the results on the density of Compton thick AGN sources in the previous work. During my three Ph.D. years I have collaborated to other research projects. The study of the relationship between radio luminosity and X-ray luminosity in AGN discussed in Chapter 4 has been carried on in collaboration with Andrea Bonchi and extended to the $K-$band luminosity to a *fundamental plane* relation. These studies have been recently published in the MNRAS; the paper is presented in Appendix A.

I have also taken part in several observing proposals with major telescopes and instruments (like VLT ISAAC and SINFONI, LBT-LUCIFER, TNG), working personally on the preparation of the observing runs, i.e. defining the samples and preparing the finding charts and the run scripts for observations in service mode. The proposals in which I have been involved are presented in Appendix B.

Throughout this work, a flat cosmological model with $H_0 = 70$ km s^{-1}, $\Omega_M = 0.3$ and $\Omega_\Lambda = 0.7$ has been assumed. Further details on the cosmological and cosmographic definitions adopted in this work are given in Appendix C.

Chapter 2

Active Galactic Nuclei

This Chapter aims at providing a very brief introduction on the physics of AGN, and their evolution in the context of galaxy formation and evolution models. A more detailed discussion can be found in Peterson (1997) and Krolik (1998) textbooks. For the evolutionary topics, see also Merloni & Heinz (2012).

2.1 Basic concepts

With *Active Galactic Nuclei* (AGN) are usually described galaxies with energetic phenomena in their nuclei, or central regions, that cannot be clearly and directly attributed to stellar activity. *Sefyert galaxies* and *quasars* represent the largest subclasses of AGN; the fundamental difference between these two classes is the amount of emitted radiation: while in a Seyfert galaxy the luminosity of the central source at visible wavelengths is comparable to the luminosity of the whole galaxy, in a quasar the central source may be up to 100 times brighter.

There are some characteristic features that are usually present in an AGN, although not necessary at the same time, including:
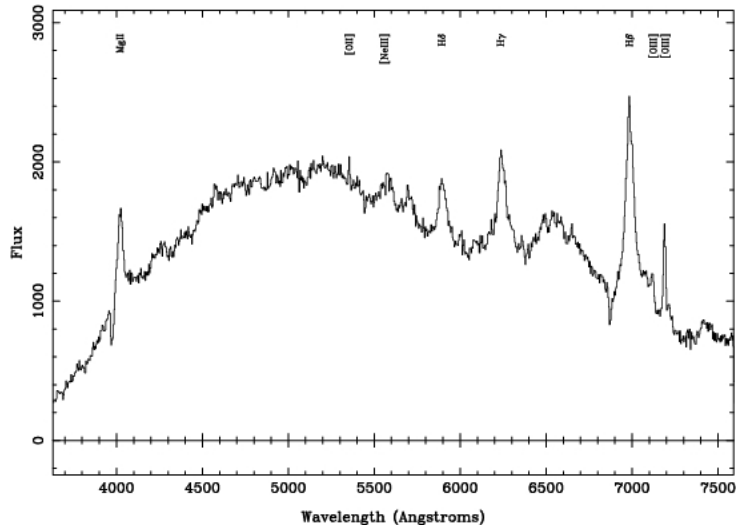
Figure 2.1: Optical spectrum of a typical Seyfert 1 (from Hawkins 2004).

- small, unresolved angular size;

- nuclear broad-band emission, over a wide portion of the electromagnetic spectrum;

- strong nuclear emission lines, mainly found in the infrared and optical/UV part of the spectrum;

- variability, both in the continuum emission and in the emission lines, especially in the X-rays;

- higher degree of polarization ($0.5 - 2\%$) with respect to the normal galaxies.

AGN have been classified on the basis of their emission in the optical, X-ray and radio band. In the optical/UV band, the classification is based on the shape of the emission lines; it is possible to distinguish between two main groups:
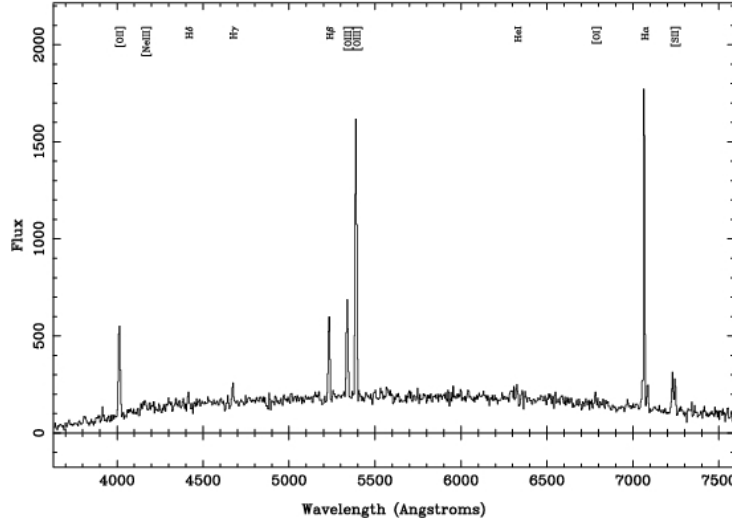
Figure 2.2: Optical spectrum of a typical Seyfert 2 (from Hawkins 2004).

Broad-line emission galaxies (or *Type-1* AGN, AGN1) show two separate emission line systems: broad lines corresponding to permitted transitions (e.g. Lyα, CIV, MgII, Balmer hydrogen lines) in a gas with $v \gtrsim 10^4$ km s^{-1}, and narrow lines corresponding to forbidden transitions (e.g. [NeIV], [NeV], [OII], [OIII]) in an ionized gas with low density ($n_e = 10^3 - 10^6$ cm^{-3}) and $v \simeq 10^2$ km s^{-1}. An example of a typical spectrum of a Type-1 AGN is shown in Figure 2.1.

Narrow-line emission galaxies (or *Type-2* AGN, AGN2) are only characterized by narrow emission lines, from both permitted and forbidden transitions. In Type-2 AGN the continuum emission is weaker with respect to the continuum seen in Type-1 AGN, and is almost flat. Figure 2.2 shows an example of a typical spectrum of a Type-2 AGN.

In the X-rays the absorption effect is weaker than in the optical/UV band, but it is still able to induce variations in the spectrum. The obscuration in the X-ray band is usually parametrized in term of the *column density* (N_H), which

represents the number density per unit area of hydrogen-equivalent atoms integrated along the line of sight. The presence of this material induces a flattening in the low energy part of the X-ray spectrum; the cutoff energy depends on the N_H value, and increases for increasing N_H. AGN with $N_H < 10^{22}$ cm^2 are usually defined as *unobscured* (or *unabsorbed*) AGN, while AGN with $N_H > 10^{22}$ cm^2 are defined as *obscured* (or *absorbed* AGN). The latter are further divided in two classes of absorption. The observed, absorbed flux F_{obs} can be written as

$$F_{\mathrm{obs}}(\lambda) = F_{\mathrm{int}}(\lambda)e^{-\tau}, \qquad (2.1)$$

where F_{int} is the intrinsic, unabsorbed flux and τ is the *optical depth*:

$$\tau = \int \sigma_{\mathrm{T}} \cos\theta\, n(r)\mathrm{d}r = N_H \sigma_\tau, \qquad (2.2)$$

where the integral is defined along the line of sight, $n(r)$ is the number density, θ the angle to the normal and $\sigma_{\mathrm{T}} = 6.65 \times 10^{-25}$ cm^{-2} the Thomson cross-section. If $\tau > 1$, the source becomes optically-thick, and is opaque to the optical/UV and X-ray photons. This happens when $N_H \gtrsim 1/\sigma_\tau$ ($\sim 10^{24}$ cm^{-2}); sources with $N_H > 10^{24}$ cm^{-2} are therefore defined as *Compton-thick* AGN, while absorbed sources with $N_H < 10^{24}$ cm^{-2} are usually defined as *Compton-thin* AGN.

At radio wavelength, AGN have been divided in two main groups, depending on the intensity of their radio emission. A fraction of $\sim 10\%$ of the AGN population is defined as *radio-loud*, while the remaining sources are *radio-quiet*. However, the criterion used to distinguish between these two classes is not well defined.

2.2   Inner structure

The most bright AGN may emit *bolometric* (emitted across the whole electromagnetic spectrum) luminosities as high as 10^{48} erg s^{-1}, in a volume that

is significantly smaller than a cubic parsec. The fundamental question about AGN is then how this great amount of energy is generated. It is widely accepted that the central engine of AGN consists in a supermassive black hole surrounded by an accretion disk, where the material in gravitational infall dissipates its kinetic energy. This accretion disk is then heated to high temperatures, and is thus responsible of most of the observed radiation.

It is possible to estimate the mass of the SMBH by assuming that the accreting material is a fully-ionized hydrogen gas, as well as isotropy and stability of the central source. The radial component of the gravitational force acting on an electron-proton pair, with masses m_e and m_p respectively, is:

$$F_{\text{grav}} = -\frac{GM(m_p + m_e)}{r^2} \simeq -\frac{GMm_p}{r^2},\tag{2.3}$$

where M is the mass of the central source. For high energy production rates, the radiation pressure due to Thomson electron scattering become important on the accreting gas. The radial component of the outward force on a single electron due to radiation pressure is given by

$$F_{\text{rad}} = \sigma_T \frac{L}{4\pi r^2 c},\tag{2.4}$$

where L is the luminosity of the source. To avoid disintegration of the source, the outward radiation force must be balanced by the inward gravitational force. Therefore, the luminosity of the source must not exceed a maximum allowed value, the *Eddington luminosity* (L_E):

$$L_E = \frac{4\pi G c m_p M}{\sigma_T} \simeq 1.26 \times 10^{38} \frac{M}{M_\odot} \text{ erg s}^{-1}.\tag{2.5}$$

If we consider sources with $L_{\text{bol}} = 10^{46} - 10^{48}$ erg s^{-1}, a central mass of $10^8 - 10^{10} \ M_\odot$ is obtained from Equation 2.5.

Another key question concerns how efficiently the accreted mass is converted into radiated energy. The rate at which energy is emitted by the nucleus is

$$L = \epsilon \dot{M} c^2,\tag{2.6}$$

where ϵ is the *radiative efficiency* and $\dot{M} = \mathrm{d}M/\mathrm{d}t$ is the *mass accretion rate*. The potential energy of a mass m at a distance r from the central source of mass M is $U = GMm/r$, so the luminosity of the source can be written as:

$$L \simeq \frac{\mathrm{d}U}{\mathrm{d}t} = \frac{GM\dot{M}}{r}. \tag{2.7}$$

Combining Equations 2.6 and 2.7 we obtain:

$$\epsilon = \frac{GM}{c^2 r} = \frac{1}{2}\frac{R_\mathrm{S}}{r}, \tag{2.8}$$

where we have introduced the *Schwarzschild radius* $R_\mathrm{S} = 2GM/c^2$. The bulk of the emission of the optical/UV emission from the accretion disk is believed to be produced at $r \sim 5R_\mathrm{S}$. Therefore, this simple calculation suggest that $\epsilon \simeq 0.1$. With this radiative efficiency, a relatively low accretion rate is requested to fuel even a fairly high luminosity source (e.g. $\dot{M} \sim 2\,M_\odot\,\mathrm{yr}^{-1}$ for $L \sim 10^{46}\,\mathrm{erg\,s}^{-1}$). However, the value of the radiative efficiency depends on how the accretion actually occurs, though $\epsilon \simeq 0.1$ is a fairly good approximation.

2.3   Continuum emission

The AGN *spectral energy distribution* (SED) is quite complex, and spans a very wide range of wavelengths, from radio to $\gamma-$rays. At a first order approximation, it can be described with a power-law:

$$F_\nu \propto \nu^{-\alpha}, \tag{2.9}$$

where the *energy index* α is usually found in the range $\alpha = 0 - 1$.

As an example, Figure 2.3 shows typical SED of a Seyfert galaxy, a radio-loud quasar and a radio-quiet quasar. The gap in the UV part of the spectrum, between 912 Å (the *Lyman continuum edge*) and ~ 100 Å is due to absorption by neutral hydrogen in our own Galaxy, which makes any detection impossible at these wavelengths.
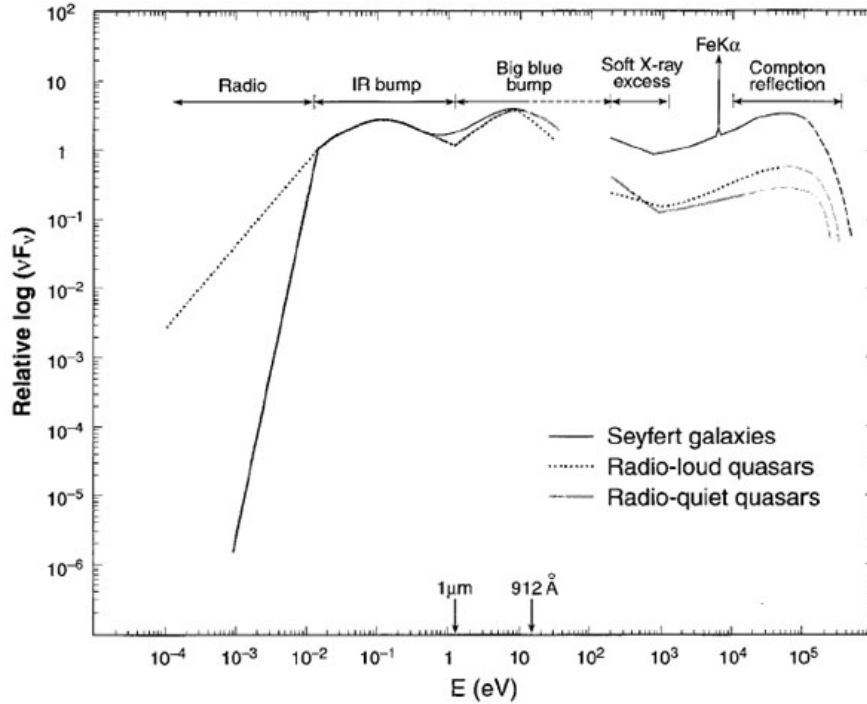
Figure 2.3: SED from radio to X-rays of a Seyfert galaxy, a radio-loud quasar and a radio-quiet quasar (from Koratkar & Blaes 1999).

While a power-law representation is a reasonable description of the SED when looking over several decades of frequency, a deeper analysis reveals many features, suggesting that the continuum emission is produced by different processes in different regions of the spectrum.

A great amount of energy is emitted in a feature that dominates the spectrum at wavelengths shorter than 4000 Å and extends beyond 1000 Å, the so called *big blue bump*. In the X-ray region, AGN spectra usually show a sharp rise with decreasing photon energy, the *soft X-ray excess*, that may be the high energy end of this feature. The big blue bump is attributed to a thermal emission with $T \sim 10^5$ K. As a first order approximation, we can assume

that the accretion disk radiates locally like a blackbody:

$$B_\nu = \frac{2h\nu^3}{c^2} \frac{1}{e^{h\nu/kT(r)} - 1}, \tag{2.10}$$

where $T(r)$ is the disk temperature at a distance r from the center. Under the assumption that the disk is geometrically thin (and optically thick), it is possible to obtain the total specific luminosity of the disk by integrating over the full range of radii:

$$L_\nu = \frac{4\pi^2 h\nu^3 \cos i}{c^2} \int_{R_{in}}^{R_{out}} \frac{r\,dr}{e^{h\nu/kT(r)} - 1}, \tag{2.11}$$

where i is the inclination angle of the disk to the plane of the sky, and R_{in} and R_{out} are the inner and outer boundaries of the disk, respectively.

At low frequencies, $h\nu \ll kT(R_{out})$, the emission follows the Rayleigh-Jeans approximation (i.e. $B_\nu \propto \nu^2$), while in the high-frequency regime the Wien law holds (i.e. $B_\nu \propto \nu^3 e^{-h\nu/KT}$). The thermal spectrum at intermediate frequencies, where indeed most of the energy is emitted, can be also approximated in a simple fashion, by assuming $R_{out} \gg R_{in}$. This approximation holds when there is a wide range of temperatures in the disk; otherwise, the emitted spectrum should look fairly close to a single-temperature blackbody spectrum. If we further assume that $R_{in} \simeq R_S$ and $R_{out} \to \infty$, we obtain from Equation 2.11 that $L_\nu \propto \nu^{1/3}$. An important prediction of this simple model is that the UV radiation and the optical radiation are emitted mostly in different parts of the disk.

The infrared continuum has probably a thermal origin, as supported by several pieces of evidence. Most AGN show a local minimum in their SED around 1 μm, which may represent the transition region between the hot thermal emission from the accretion disk and a cooler ($T \lesssim 2000$ K) thermal emission. Hot dust grains in the nuclear regions have indeed a temperature around 2000 K; higher temperatures should induce sublimation of dust

grains. This temperature limit allows to explain the constancy of the frequency where the infrared spectrum is weakest with a Wien cut-off of a 2000 K blackbody.

Some observations show that the far infrared spectrum decreases rather sharply at higher wavelength, with a spectral index $\alpha \lesssim -2.5$. A thermal spectrum can produce a cut-off this sharp because the emitting efficiency of dust grains has a strong dependence on the frequency ($Q_\nu \propto \nu^\gamma$, with $\gamma \sim 2$). Therefore, the emitted spectrum can have a very strong frequency dependence, $F_\nu \propto \nu^{2+\gamma}$.

The mid infrared part of the spectrum is also characterized by several emission bands from Polycyclic Aromatic Hydrocarbons (PAH). PAH are carbon-based molecules that are excited in the regions of star formation, and have characteristic infrared bands at 3.29, 6.2, 7.7, 8.7, 11.3 and 12.7 μm; other weaker features are present at other wavelengths, in the range $3 - 15$ μm. Silicates also play an important role at mid infrared wavelengths: bands around 10 and 18 μm are often observed in obscured AGN and high infrared luminosity galaxies.

The X-ray emission accounts for typically $\sim 10\%$ of the bolometric luminosity of AGN. With its rapid variability, on timescales of the order of a day, it provides a probe of the innermost regions of the source. Historically, the X-ray region of the SED has been divided in *soft* X-rays ($\sim 0.1 - 2$ keV), *hard* X-rays ($\sim 2 - 100$ keV), due to the different technologies used in the observations. In X-ray astronomy, SEDs are usually fitted in photons per keV rather than in energy per unit frequency, $P_E \propto E^{-\Gamma} \propto \nu^{-\Gamma}$ [photons s^{-1} keV^{-1}]; in units of energy flux we have:

$$F_\nu \propto \nu^{-\Gamma+1} \propto \nu^{-\alpha}, \tag{2.12}$$

where α is called *energy index* and $\Gamma = \alpha + 1$ is called *photon index*. Figure 2.4 shows the average total X-ray spectrum of a Type-1 AGN, as well as the
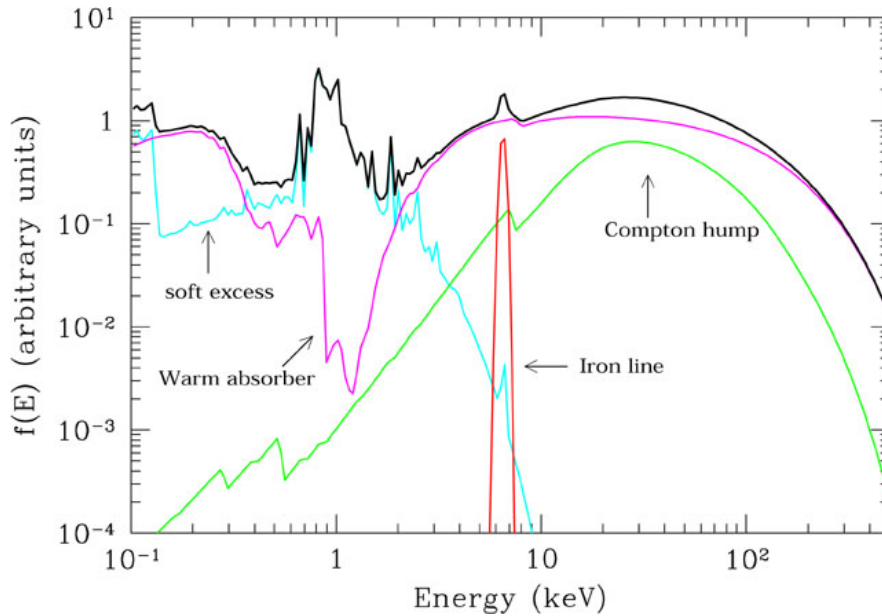
Figure 2.4: Average total X-ray spectrum (thick black line) of a Type-1 AGN. Thin lines
show the main components of the spectrum, as labeled (from Risaliti & Elvis 2004).

various components that contribute to the spectrum. Soft X-ray region is
usually well fitted with a power law with $\alpha \gtrsim 1$, while in the hard X-ray
region a flatter slope ($\alpha \sim 0.7 - 0.9$) is required. At higher energies, fits to
the X-ray spectrum of Seyfert galaxy suggest a high-energy cut-off around
a few hundreds keV. At even higher energies, only blazar-type sources (i.e.
those with a strong beamed component) have been observed.

The origin of the X-ray emission is ascribed to inverse-Compton scattering
of low energy photons by more energetic electrons. The basic idea is that the
optical/UV photons emitted from the accretion disk are scattered to higher
energies by hot (probably relativistic) electrons in a corona surrounding the
disk (this process is usually called *Comptonization*).

In addition to the basic power-law described above, AGN spectra show sev-
eral indipendent features. As already discussed, in the soft X-ray region

many AGN show a soft excess, usually explained as the Comptonized Wien tail of the big blue bump. At low energies ($h\nu \lesssim 2$ keV), absorption of heavy elements with column densities around $\sim 10^{22}$ cm^{-2} are also often observed; these are commonly referred to as *warm absorbers*. In the high energy region ($h\nu \gtrsim 10$ keV) AGN spectra rise above the power-law spectrum. This feature is attributed to Compton reflection of high energy photons on a lower energy electron gas, perhaps the disk itself.

The radio continuum has clearly a non-thermal origin, and it is associated to synchrotron emission. There are at least two pieces of evidence for a non-thermal emission. The spectral index is almost flat, but it becomes progressively steeper at shorter wavelengths. This behavior is characteristic of optically thick sources that undergo continued injection of higher energy electrons. Low energy cutoffs, attributable to synchrotron self-absorption, are detected in some sources, with a frequency dependence weaker than expected ($F_\nu \propto \nu^{5/2}$). This dependence, as well as the flatness of the spectral index, are usually explained with the complexity of the source structure.

The specific intensity I_ν of a radio source at a given frequency can be determined by measuring the flux and angular size of the source. It is possible to associate to the source an equivalent temperature $T_{\rm B}$ (the *brightness temperature*), defined as the temperature that the source would have if it was indeed radiating like a blackbody. At radio wavelengths, the Rayleigh-Jeans approximation holds for any temperature, so for an optically thick thermal source the intensity is given by the Planck function B_ν for $h\nu \ll kT$:

$$I_\nu = \frac{F_\nu}{\pi\theta^2} = B_\nu = \frac{2kT_{\rm B}}{\lambda^2}, \tag{2.13}$$

where F_ν is the observed flux at a frequency $\nu = c/\lambda$ and θ is the angular size of the source. Measurements of F_ν and θ for several compact extragalactic radio sources constrain $T_{\rm B}$ in the range $10^{11} - 10^{12}$ K, which clearly rules out a thermal origin for radio emission.
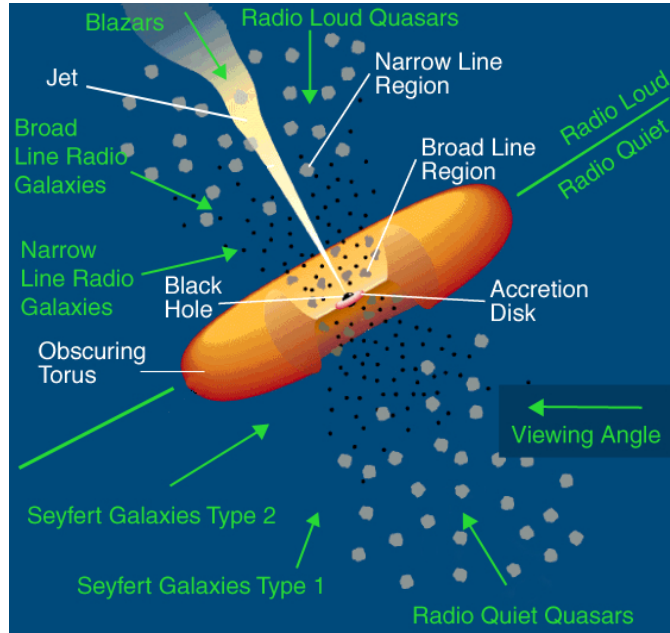
Figure 2.5: The Unified Model of AGN. Green arrows show the lines of sight associated with each class of object (from Urry & Padovani 1995).

2.4   The Unified Model of AGN

The presence of both strong high ionization and low ionization narrow lines is common to both types of AGN, and with similar line ratios. This suggested that all AGN are powered by the same intrinsic engine and led to the formulation of the standard Unified Model for AGN (Antonucci 1993; Urry & Padovani 1995). In this scenario, the observed differences between Type-1 and Type-2 AGN arise from orientation dependence, while the basic source structure remains the same. There is indeed abundant evidence that AGN have axisymmetryc structure, and thus radiates anisotropically. The observed properties of a particular source thus depend on the location of the observer.

The current paradigm is built around a central engine, that consists of an

accretion disk surrounding a supermassive ($M \gtrsim 10^6 \ M_\odot$) black hole. Relativistic jets emerge from the central region along the disk axis, emitting Doppler-boosted radiation via synchrotron emission and inverse Compton scattering mechanisms. The broad lines observed in Type-1 AGN are thought to be produced in dense ($n_e \gtrsim 10^9 \ \mathrm{cm}^{-3}$) gas regions nearby the central source (within a few thousands gravitational radii), where the influence of the gravitational field of the BH is strong. On parsec scales, the entire system in enshrouded in a dusty torus that is opaque to most of the electromagnetic radiation. The torus plays a key role in the framework of the Unified Model, since it allows the direct observation of the central region (including the BLR) only along particular directions. Narrow lines are generated in distant (on torus scale), rarefied gas regions, where the gravitational influence from the BH is less intense.

Therefore, an observer looking at the AGN on the torus plane (i.e. edge-on) has the view of the innermost regions (that produce the optical/UV and soft X-ray continuum) and of the BLR obstructed by the intercepting material. Only narrow emission lines are directly visible in this case. An observer looking along the axis has instead a direct view of both the BLR and the NLR, as well as the accretion disk continuum emission (Figure 2.5).

One of the most convincing evidences in favor of this model is the detection of broad optical lines in the polarized spectra of Type-2 AGN. This suggests that the BLR is still present in Type-2 nuclei, but is actually hidden from our line of sight due to the obscuring material. However, the emitted light is scattered in our direction from material distributed on scales larger than the absorbed. Such reflected light is very weak compared to the light of the galaxy, but it has a high degree of polarization, and therefore can be detected in the polarized spectrum.

Although this simple model has allowed to explain much of the complex AGN phenomenology, there is evidence supporting that additional effects are
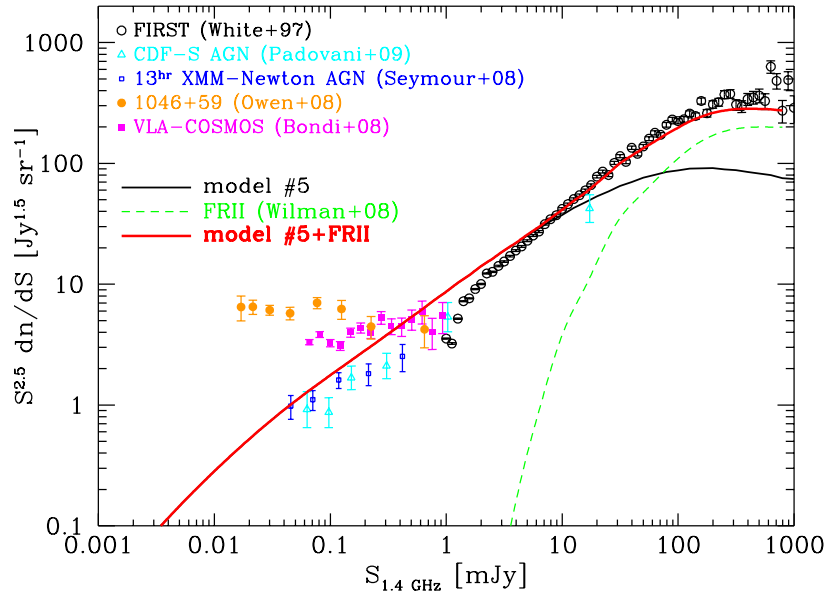
Figure 2.6: Differential Euclidean radio counts at 1.4 GHz from several data releases (from La Franca, Melini & Fiore 2010).

requested to explain the differences between Type-1 and Type-2 AGN, like the discovery of Type-2 sources without broad optical lines in the polarized spectrum.

2.5   Number counts and luminosity function

In order to describe how the AGN population has changed during cosmic time, several statistical technique have been employed. The simplest observational tool that can be used to describe the evolution of a sample of objects are the *number counts*. By number counts one typically means the surface density in the sky of a given class of sources as a function of the limiting flux of the observations.

More information can be drawn from the *luminosity function* (LF), defined

as the number of sources per unit volume and luminosity with luminosity in the range between L and $L + \mathrm{d}L$:

$$\Phi(L) = \frac{\mathrm{d}N}{\mathrm{d}V\mathrm{d}L.} \tag{2.14}$$

Let us assume that the local universe is Euclidean and filled with sources with LF $\Phi(L)$. Sources with luminosity L can be observed out to a distance $r = (L/4\pi S)^{1/2}$, being S the limiting flux of the observations. The number counts of sources over the solid angle Ω, are then:

$$N(>S) = \int_{L_{\mathrm{min}}}^{\infty} \frac{1}{3}\Omega r^3 \Phi(L)\mathrm{d}L = \frac{1}{3}\frac{\Omega}{(4\pi)^{3/2}}S^{-3/2}\int_{L_{\mathrm{min}}}^{\infty} L^{3/2}\Phi(L)\mathrm{d}L, \tag{2.15}$$

where $L_{\mathrm{min}}(r)$ is the faintest luminosity that can be observed over a flux limit S out to a distance r_{max}. Therefore, the slope of the cumulative number counts of a (non-evolving) class of objects in an Euclidean universe is fixed to $-3/2$.

In a more general case, the correct relativistic expression for number counts differs from Equation 2.15, due to cosmological effects. Radiation emitted at frequency ν' is observed at a redshifted frequency $\nu = \nu'/(1+z)$, and therefore the observed flux density depends on the shape of the spectrum of the source. Moreover, curvature effects modify the volume element per unit redshift, making it smaller at increasing z.

The simplest general approach to describe the evolution of a LF is by defining two functions $f_d(z)$ and $f_l(z)$ that take into account the evolution of the number density and luminosity respectively:

$$\Phi(L, z) = f_d(z)\Phi(L/f_l(z), z = 0). \tag{2.16}$$

In the *pure luminosity evolution* (PLE; Mathez 1976) scenario, the comoving number density of sources is constant (so $f_d = \mathrm{cost}$), but luminosity varies with cosmic time; in the *pure density evolution* (PDE; Schmidt 1968) case,
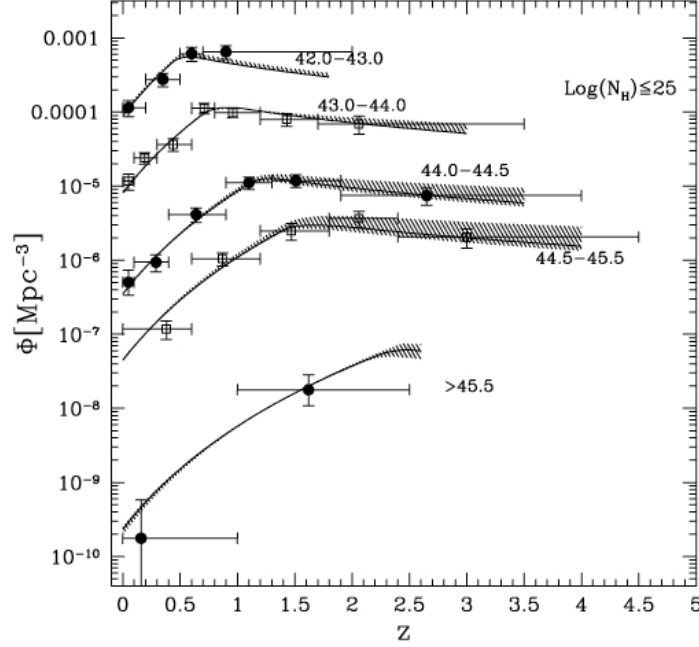
Figure 2.7: The space density of AGN as a function of redshift in different luminosity bins. Solid lines show the best-fit values in LDDE model with evolving N_H depending on L_X and z (from La Franca et al. 2005).

the shape of the LF and the source luminosity are fixed ($f_l = $ cost), while the comoving density of sources of any luminosity varies.

While the PDE model fails to describe the observed quasar number counts and overpredicts the CXRB, the PLE model tends to overpredict the number of SMBH with $M > 10^{10} M_\odot$. Therefore, more complex models have been developed throughout the years. The most accurate description of the overall evolution of the LF comes from deep X-ray surveys. While for optically selected quasar the PLE model still provide a good fit of the data, the *luminosity dependent density evolution* (LDDE) model is invoked to describe the evolution of the X-ray LF (Ueda et al. 2003; see also Hasinger, Miyaji & Schmidt 2005 for soft X-ray selected AGN). As in the PDE model, the

redshift evolution of the LF is described as

$$\frac{\mathrm{d}\Phi(L_X, z)}{\mathrm{d}\log L_X} = \frac{\mathrm{d}\Phi(L_X, z = 0)}{\mathrm{d}\log L_X} e(L_X, z), \qquad (2.17)$$

where the local LF is usually represented with a power-law with two different indexes, for low and high luminosities:

$$\frac{\mathrm{d}\Phi(L_X)}{\mathrm{d}L_X} = \begin{cases} AL_*^{\gamma_1-\gamma_2} L_X^{-\gamma_1} & L_X \leq L_* \\ AL_X^{-\gamma_2} & L_X > L_*. \end{cases}, \qquad (2.18)$$

and the evolution factor $e(z)$ is defined as:

$$e(z) = \begin{cases} (1+z)^{p_1}, & z \leq z_c(L_X), \\ e(z_c)[(1+z)/(1+z_c(L_X))]^{p_2}, & z > z_c. \end{cases} \qquad (2.19)$$

The z_c parameter represent the redshift at which the evolution stops. The parameters p_1 and p_2 characterize the rate of the evolution and the rate of counterevolution for $z > z_c$ respectively.

The LDDE model is obtained by introducing a luminosity dependence of z_c, assumed to be a power-law (La Franca et al. 2005):

$$z_c(L_X) \begin{cases} z_c^*, & L_X \geq L_a, \\ z_c^*(L_X/L_a)^\alpha, & L_X < L_a. \end{cases} \qquad (2.20)$$

It has been shown that (a) the peak of the AGN space density moves to smaller redshift with decreasing luminosity, and (b) the rate of evolution from the local universe to the peak redshift is slower for less luminous AGN (*downsizing*; see Figure 2.7). It appears that SMBH generally grow in an "anti-hierarchical" fashion, i.e. while more massive SMBH ($10^{7.5} - 10^9 \ M_\odot$) in rare, luminous AGN could grow efficiently at $z = 1 - 3$, smaller SMBH in more common, less luminous AGN had to wait longer to grow ($z < 1.5$).

There is also strong evidence on the redshift and luminosity dependence of the fraction of obscured ($N_H > 10^{22} \ \mathrm{cm}^{-2}$) AGN: it has been shown that this

fraction increases with decreasing luminosity (Ueda et al. 2003; La Franca et al. 2005; Treister & Urry 2005) and increasing redshift (La Franca et al. 2005; Treister & Urry 2006; Hasinger 2008).

Attempts to constrain models for galaxy formation and evolution from the optical and X-ray luminosity functions were made in the last decade by several authors (see e.g. Granato et al. 2001, 2004; Di Matteo, Springel & Hernquist 2005; Menci et al. 2004, 2005). The predictions of these models are in good agreement with some of the observations, like the downsizing trend; however, they overestimate by a factor of ~ 2 the space density of low-luminosity, Seyfert-like AGN at $z = 1.5 - 2.5$.

2.6   X-ray surveys and the X-ray background

As already mentioned in Section 2.3, AGN are powerful X-ray emitters. The discovery of the cosmic X-ray background (CXRB; Giacconi et al. 1962) opened up a privileged window for the study of the energetic phenomena associated with accretion onto black holes.

The X-ray sky is almost dominated by the AGN population, due to the relative weakness of the other X-ray emitters (mostly X-ray binaries, but also magnetically active stars, cataclysmic variables), at least down to the faintest fluxes probed by current X-ray telescopes. The goal of reaching a complete census of evolving AGN has therefore been intertwined with that of fully resolving the CXRB into individual sources.

In the last decade, the launch of modern X-ray telescopes like *Chandra* (NASA) and *XMM-Newton* (ESA) has enabled strong observational progress. Sensitive imaging spectroscopy in the $0.5 - 10$ keV band with up to $50 - 250$ times the sensitivity of previous missions, as well as high quality positional accuracies (up to $\sim 0.3 - 1''$ for *Chandra*) were made available for X-ray astronomy studies. Deep extragalactic surveys have probed the X-ray sky
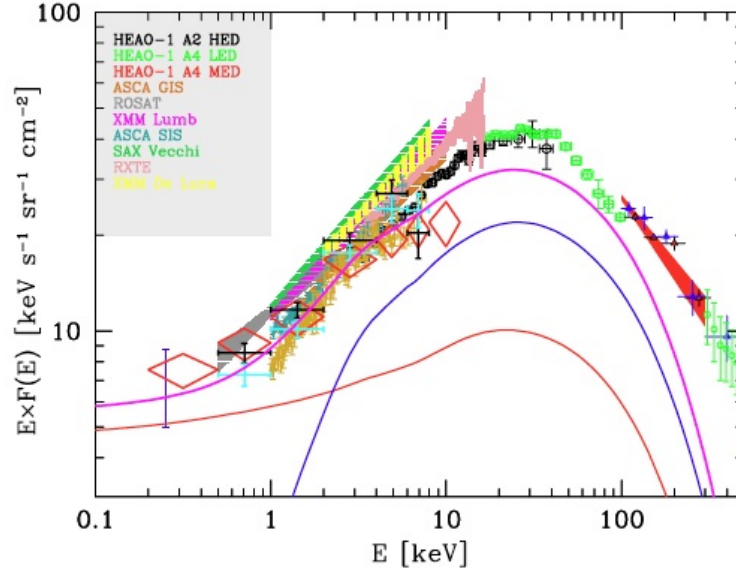
Figure 2.8: Observed spectrum of the extragalactic CXRB from several X-ray satellites data. The solid magenta line shows the prediction of the Gilli, Comastri & Hasinger (2007) model for AGN (unobscured + Compton-thin) and galaxy clusters; red and blue solid lines represent the contribution from unobscured and Compton-thin AGN respectively (from Gilli, Comastri & Hasinger 2007).

down to extremely faint fluxes (as low as $\sim 10^{-17}$ erg s^{-1} cm^{-2} in the $0.5 - 2$ keV band and $\sim 10^{-16}$ erg s^{-1} cm^{-2} in the $2 - 8$ keV band), thus making available large source samples for statistical X-ray source population studies.

With these deeper and larger X-ray surveys that have been performed, a new generation of synthesis model for the CXRB has been developed (see Gilli, Comastri & Hasinger 2007; Treister, Urry & Virani 2009). These new models have progressively reduced the uncertainties in the N_H absorption distribution, providing an almost complete census of the unobscured and moderately obscured AGN populations. These sources dominate the X-ray counts in the lower energy band, where almost all the CXRB radiation has

been resolved into individual sources.

However, at the peak energy of the CXRB (around ~ 30 keV), only a small fraction ($\sim 5\%$) of the emission has been resolved into individual sources. CXRB synthesis models ascribe a substantial fraction of this unresolved emission to Compton-thick AGN. Gilli, Comastri & Hasinger (2007) model requires that a population of Compton-thick AGN as large as that of Compton-thin AGN should exist to fit the residual background emission. Still, the redshift and luminosity distribution of these sources is essentially unknown, due to their faintness even at hard X-ray energies. The quest for the physical characterization of this missing AGN population represents one of the last current frontiers of the study of AGN evolution.

2.7   SMBH growth in galaxies

In the early 1990s, deep optical surveys of star-forming galaxies began to probe the cosmological evolution of the rate at which stars are formed within galaxies, thus providing robust constraints for models of galaxy formation and evolution (see e.g. Madau et al. 1996). It was soon clear that the QSO (optical) luminosity density and the *Star Formation Rate* (SFR) density evolved in a similar fashion, being much higher in the past, with a broad peak around $z \sim 2$ (Boyle & Terlevich 1998).

Direct measures of the SMBH masses can be obtained from stellar dynamics or spectral analysis of circumnuclear dust and gas. However, it has been possible to perform these measures only for a small (~ 50) number of SMBH, due to limitations induced by spatial resolution. With these measures available, it has been observed that the SMBH mass (M_{BH}) correlates tightly with some structural parameters of the host galaxy, like the host spheroid mass (Kormendy & Richstone 1995; Marconi & Hunt 2003), luminosity (Magorrian et al. 1998) and stellar velocity dispersion (Ferrarese & Merritt 2000;

Gebhardt et al. 2000).

Direct or indirect (from scaling relations) knowledge of the SMBH masses allows to test the classical "Soltan argument" (Soltan 1982), according to which the local mass budget of SMBH in galactic nuclei should be accounted by integrating the overall energy density released by AGN, assuming an appropriate radiative efficiency parameter. The total accreted mass can be computed as a function of redshift:

$$\rho_{\text{BH}} = \int_z^{z_s} \dot{\rho}_{\text{BH}}(z) \frac{\mathrm{d}t}{\mathrm{d}z} \mathrm{d}z, \tag{2.21}$$

where the black hole accretion rate density $\dot{\rho}_{\text{BH}}(z)$ is given by:

$$\dot{\rho}_{\text{BH}}(z) = \frac{1-\epsilon}{\epsilon c^2} \int \Phi(L_{\text{bol}}, z) \mathrm{d}L_{\text{bol}}, \tag{2.22}$$

where $\Phi(L_{\text{bol}}, z)$ and $L_{\text{bol}} = \epsilon \dot{M} c^2$ represent the bolometric LF and the bolometric luminosity respectively.

This computation has been performed either using the CXRB as a "bolometer" to derive the total energy density released by the accretion process (Fabian & Iwasawa 1999), or by considering evolving AGN luminosity functions (Yu & Tremaine 2002; Marconi et al. 2004; Merloni & Heinz 2008). This approach represents a major success of the standard paradigm of accreting black holes as AGN power-sources, as the radiative efficiencies requested in order to explain the local relic population are within the range $\epsilon = 0.06-0.20$, predicted by standard relativistic accretion disc theory.

These evidences suggest that a tight link should exist between SMBH growth and host galaxy evolution. Many processes have been proposed which could forge this direct connection, including galaxy major mergers, star formation winds and AGN-driven outflows. From a physical point of view, these *feedback* mechanisms by which AGN can regulate the growth of their host galaxies can be distinguished into two main modes.

The first mode is associated with the phases of fast SMBH growth in bright AGN. Star formation and SMBH growth are fueled by the same cool gas located in the inner regions of the galaxy. The fast, explosive energy injection from the central source can heat and disperse this gas, thus quickly terminating both star formation and SMBH growth. In this scenario (*quasar mode* feedback; see e.g. Menci et al. 2008), the triggering of such bright phases is thought to be related to galaxy mergers, in which cold gas is injected. The quasar mode efficiency must be proportional to the AGN fraction (i.e. the AGN luminosity function versus the galaxy luminosity function) and to how efficiently the AGN energy is released into the interstellar medium.

The second mode is related to the numerous, long-lived, low-luminosity AGN, that accrete hot gas coming from the halo's hot atmosphere continuously during cosmic time. This accretion happens at very low rates ($\sim 10^{-5} \ M_\odot \ \mathrm{yr}^{-1}$) in an inefficient regime, where the cooling of the central source is dominated by advective processes rather than radiation. The contribution of this accretion rate is too small to contribute significantly to the bolometric output of the AGN. However, these sources can still drive powerful, collimated outflows in the form of relativistic jets, which can perturb mechanically the surrounding gas (*radio mode* feedback; Croton et al. 2006; Bower et al. 2006). This feedback action has been observed in several systems; by combining radio (synchrotron jet emission) and *Chandra* X-ray (hot, bremsstrahlung-emitting intracluster medium) images, it has been observed that these jets are capable of excavate cavities in the intracluster gas on sub-galactic scales (e.g. McNamara et al. 2000). The radio mode efficiency depends on the total accreted mass (and then to the SMBH mass function).

Both these feedback modes are then capable to release energy directly in the environment from which the SMBH grows: the cooling, star-forming gas in the central region of the galaxy. This energy transfer not only reduces the rate at which the gas cools and form stars, but it also reduce the rate of accretion

onto the SMBH. Feedback from AGN has been included in recent semi-analytical models of galaxy evolution to switch off star formation in most massive galaxies, thus reproducing both the observed shape of the galaxy LF and the red, early type, passive evolving nature of the local massive galaxies. Quasar mode feedback is usually invoked to quench star formation at higher redshift, while radio mode feedback is assumed to suppress the cooling flows in massive galaxies at late times, thus maintaining the gas in a hot, tenuous state.

Chapter 3

Data set

3.1   Introduction

A full comprehension of the BH-galaxy co-evolutionary process requires the simultaneous measure, in large samples of sources, of four key parameters that characterize the AGN phenomena. These four parameters are:

- the SMBH mass, M_{BH};

- the host galaxy mass, M_*,

and the two time derivatives of the former quantities:

- the BH accretion rate, $\dot{M}_{\mathrm{BH}}$;

- the star formation rate, $\mathrm{SFR} = \dot{M}_*$.

All these quantities can be inferred from observations in different bands: M_{BH} can be derived from measures of the optical luminosity and broad emission line widths, $\dot{M}_{\mathrm{BH}}$ is directly related to the X-ray luminosity (by the means of a bolometric correction factor), M_* can be obtained from optical/infrared SED fitting and the SFR from the measure of the UV or far infrared luminosity of the host galaxy, and from narrow emission lines in optical spectra.

Other useful information comes from high resolution imaging (host galaxy morphology) and lensing studies (dark matter halo mass), and from radio emission, which traces the relativistic particle output of the BH and plays a key role in the measure of the kinetic output of AGN.

To measure all the above quantities, complete samples, with spectroscopic and multiwavelength photometric data, are necessary. As discussed in Section 2.6, the selection of AGN samples at X-ray wavelengths does not suffer from contamination from not active sources, like in the optical and infrared bands. Moreover, current X-ray surveys are capable to select efficiently low luminosity AGN and moderately obscured sources. Therefore, X-ray selected samples, coupled with multiwavelength data, are commonly used to study the bolometric output of BH in the majority of AGN. In evolutionary studies, both large and deep surveys are usually employed, in order to obtain an optimal coverage of the redshift-luminosity space.

Only a handful of Compton-thick sources are included in X-ray selected samples. However, thanks to the dust reprocessing of the UV/optical emission, it is possible to recover these sources in mid infrared samples. At these wavelengths, the contamination from passive but bright galaxies (like star forming galaxies) is much stronger; selection criteria based on the emission in other bands are then employed to distinguish between normal and obscured active galaxies.

In this Chapter we present the data sets that have been generated to perform the measures described in this work. In Section 3.2 the mid-infrared sample that has been built to measure the density of Compton-thick AGN is presented, along with the match and identification issues and the SED fitting. In Section 3.4 we show the X-ray sample, with full 1.4 GHz radio coverage, that has been generated in order to perform the measures discussed in Chapter 4 and Appendix A.

3.2 The 24 μm selected data set

3.2.1 The COSMOS survey

COSMOS (Scoville et al. 2007) is a deep and wide extragalactic survey designed to probe the correlated evolution of galaxies, star formation, AGN and dark matter with large scale structure over a large redshift range ($z < 6$). The survey covered an area of about 2 deg^2 (Figure 3.1) near the equatorial plane, centered in $(\alpha, \delta) = (10^h 00^m 28.6^s, 02°12'21'')$, in a field devoid of bright X-ray, UV or radio sources, and where the galactic extinction is low ($E_{B-V} \simeq 0.02$) and uniform with respect to other equatorial fields. Extensive multiwavelength ground or space-based observations have been performed, spanning the entire electromagnetic spectrum. More than 2×10^6 galaxies have been detected by COSMOS with a high completeness over a magnitude limit $I_{AB} < 26.0$.

All these properties make the COSMOS data-set the best possible choice for evolutionary studies. Details on the catalogs used in this work will be given in the following section.

Mid-infrared data

The COSMOS field was observed by *Spitzer* onboard instruments at near-infrared wavelenghts (with the InfraRed Array Camera, IRAC) and at mid-infrared wavelenghts (with the Multiple Imaging Photometer for *Spitzer*, MIPS).

The 24 μm observations my MIPS have been carried out during two different observational programs. The first one (GO2) was carried out in 2006 January over an area of ~ 4 deg^2 centered on COSMOS, with a median integration time of 80 s per pixel; the second deeper observations (GO3) were performed in 2007 over an area of ~ 3 deg^2 using the MIPS slow scan mode (see Sanders
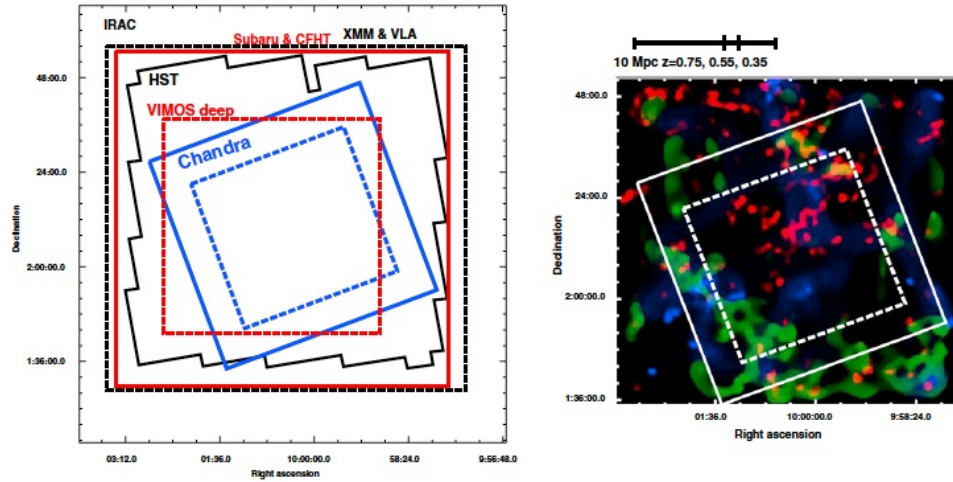
Figure 3.1: Left panel: map of the COSMOS field showing the coverage at various wavelengths: IRAC 3.6 μm (background image); *Chandra* (blue), *HST* (black solid), Subaru, CFHT & zCOSMOS bright (red solid), zCOSMOS deep (red dashed), XMM & VLA (black dashed). MIPS observations cover an area two times larger. Right panel: large scale structure seen in galaxy distribution in the COSMOS field; the C-COSMOS field outline is shown as the white square (from Elvis et al. 2009).

et al. 2007 for details). Across the 2 deg^2 COSMOS area, the combination of the GO2 and GO3 observations give a median integration time of ~ 3360 s per pixel. The final COSMOS MIPS GO2+GO3 24 μm catalog has been presented by Le Floc'h et al. (2009). It contains a total of 39413 sources down to a flux limit of 60 μJy with a completeness of about 75%.

X-ray data

Both ESA *XMM-Newton* and NASA *Chandra* X-ray satellites had devoted several observational time to complete X-ray surveys of the COSMOS field. In this work, data from the *Chandra*-COSMOS survey (C-COSMOS, Elvis et al. 2009) have been used.

The C-COSMOS survey cover the central 0.9 deg^2 of the COSMOS. A total

of 36 ACIS-I 50 ks pointings took place in two main blocks, 2006 December to 2007 January and 2007 April to June, for a total observing time of 1.8 Ms. These pointings have been carried out following a heavily overlapped grid; this strategy has allowed to cover a large area to a well-defined exposure and uniform flux limit. An almost uniform exposure time of ~ 185 ks has been achieved for the 0.9 deg^2 area.

The authors have also released a point source catalog from the C-COSMOS survey. It contains 1761 X-ray sources detected in at least one band, down to a flux limit of 2×10^{-16} erg s^{-1} cm^{-2} in the soft $(0.5 - 2$ keV$)$ band and of 7.3×10^{-16} erg s^{-1} cm^{-2} in the hard $(2 - 10$ keV$)$ band.

Creation of the main 24 μm selected COSMOS sample

The sample has been generated starting from the previously described 24 μm MIPS GO2+GO3 catalog from Le Floc'h et al. (2009). We have first looked for the optical/NIR counterparts of the 24 μm sources in the K-band; this resulted to be a good trade-off between a) the PSF quality and b) the proximity to the 24 μm band. Therefore, in order to properly identify the correct $K-$band counterparts, the 24 μm sources have been cross-correlated with the $K-$band catalog from McCracken et al. (2010), using the likelihood ratio (LR) technique as described by Sutherland & Saunders (1992, see also Ciliegi et al. 2003; Brusa et al. 2007).

The likelihood ratio is defined as the ratio between the probability that a source is the true counterpart and the corresponding probability that is, instead, a background object (Sutherland & Saunders 1992):

$$LR = \frac{q(m)f(r)}{n(m)}, \tag{3.1}$$

where, in our case, $q(m)$ is the expected probability distribution of the counterparts as a function of the apparent K-band magnitude m, $f(r)$ is the

probability distribution of the positional errors among the two catalogs, assumed to be a two-dimensional Gaussian, and $n(m)$ is the surface density of background sources with $K-$band magnitude m.

To estimate $q(m)$ we have subtracted the expected number of $K-$band background objects $n(m)$ from the observed total number of objects nearby the positions of the 24 μm sources; we have used a value of $r = 0.6''$ (1σ), that maximize the fraction of identifications, minimizing the number of spurious IDs.

In the case of multiple possible counterparts, additional information is required to discriminate between each individual counterpart. To this purpose the reliability for object j being the true counterpart is used (Ciliegi et al. 2003):

$$\text{Rel}_j = \frac{(LR)_j}{\sum_i (LR_i) + 1 - Q},\tag{3.2}$$

where the sum is over all the N possible counterparts and Q represents the probability that the counterpart is brighter than the magnitude limit of the K-band counterparts catalog.

We have tested several LR thresholds in order to minimize the fraction of both not identified sources and of spurious identifications. The best possible choice turned out to be $LR = 0.1$, for which we found 1.8% of spurious identifications and a fraction of 7.4% of not identified sources.

We can define two new quantities depending on LR: the reliability ratio R between the sum over all the reliabilities for all possible counterparts over LR and the total number of sources above the same threshold:

$$R(LR) = \frac{\sum_j \text{Rel}_j(LR)}{N(> LR)},\tag{3.3}$$

and the completeness ratio C between sum over all the reliabilities for all possible counterpart above LR and the total number of sources for which
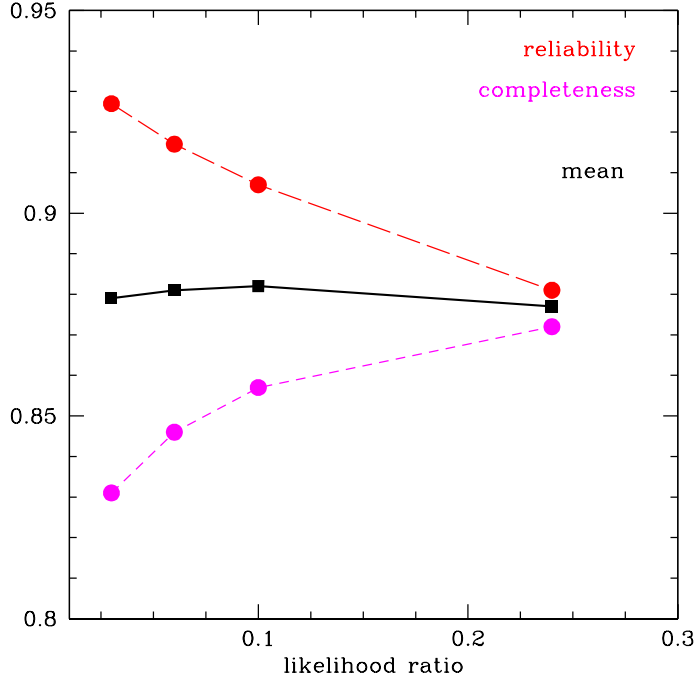
Figure 3.2: Reliability (red) and completeness (magenta) for several values of the likelihood ratio LR (see text). The black solid curve represents the mean value between R and C.

the likelihood ratio technique has been applied:

$$C(LR) = \frac{\sum_j \mathrm{Rel}_j(LR)}{N}. \tag{3.4}$$

A good choice of the LR threshold should maximize the mean value between R and C. For $LR = 0.1$, we found $R = 0.857$ and $C = 0.907$, with a mean value of 0.882. Smaller values have been found for different LR threshold, e.g. $R = 0.872$, $C = 0.881$ (mean value 0.877) for $LR = 0.24$, and $R = 0.846$, $C = 0.917$ (mean value 0.881) for $LR = 0.06$. Therefore, assuming a threshold of $LR = 0.1$ also gives a maximum in the mean value between R and C (Figure 3.2).

With this assumption, a single $K-$band counterpart has been found for the

majority (86.4%) of the 24 μm sample. The remaining sources have either two (12.7%), or three or more (0.9%) possible counterparts. We have decided to reject all the sources with three or more identifications. For the sources with a double identification, we computed the ratio R_d between the two LR values and decided to accept an identification if R_d was greater than a certain threshold $R_\mathrm{d_{th}}$. In order to chose the best $R_\mathrm{d_{th}}$ value a Monte Carlo simulation has been performed. We measured the number of spurious identifications as a function of $R_\mathrm{d_{th}}$ assuming the observed distribution of magnitudes and distances between the $K-$band counterparts and the 24 μm sources (affected by a random distribution of positional errors). Eventually we fixed the threshold to the value $R_\mathrm{d_{th}} = 10$, corresponding to a 95% probability that the chosen counterpart is the true one. All the double identifications with $R_\mathrm{d} > 10$ (or $R_\mathrm{d} < 0.1$) were selected and flagged as good identifications; similarly, all the counterparts in the range $R_\mathrm{d} = 0.1 - 10$ were flagged as bad double identifications.

Results

We have limited our analysis in the 0.9 deg^2 area covered by *Chandra* observations (see Figure 3.1) and conservatively selected the 24 μm sources having fluxes brighter than 80 μJy. When adopting these limits, we found a reliable $K-$band counterpart for a fraction of 86.6% of the selected 24 μm sources; for the remaining 13.4% of the sources, a $K-$band counterpart is not available, because, as discussed in the previous section, (a) we did not found a counterpart within the error box, (b) we found a counterpart, but it did not pass the cut in LR, (c) we found three or more possible counterparts.
In total to 14 977 24 μm sources with $F_{24\ \mu\mathrm{m}} > 80$ μJy it was assigned a $K-$band counterpart. 14 954 of these $K-$band identified sources have been cross-correlated with the multi-photometric catalog (CFHT u^*, Subaru B_J, V_J, g^+, r^+, i^+, z^+, UKIRT J, CFHT K, 3.6, 4.5, 5.8 and 8.0 μm IRAC

bands) from Ilbert et al. (2009). According to Ilbert et al. (2009) all these sources have a photometric redshift determination. We have looked in the latest COSMOS spectroscopic redshift catalog (Salvato et al. in preparation) if spectroscopic redshifts were available for this sample. We adopted the spectroscopic redshifts for both those sources with a reliable ($> 99\%$) determination (3606), and for those sources (304) having a less secure spectroscopic redshift but a similar photometric redshift (within 15%). The 23 sources not included in the multi-photometric catalog by Ilbert et al. (2009) were excluded from our analysis.

3.2.2 The GOODS survey

Overview

The Great Observatories Origins Deep Survey (GOODS; Dickinson 2001; Giavalisco et al. 2004) is a survey project based on the observations of two separated fields of 10×15 arcmin each, centered of the Hubble Deep Field North (HDFN) and the *Chandra* Deep Field South (CDFS), respectively.
The available data set includes images taken from several satellite observatiories: optical band images from the HST, mid infrared from *Spitzer*, UV from *GALEX*, and X-ray from *Chandra* and *XMM-Newton*. Observations from ground based facilities have been also carried on (see Giavalisco et al. 2004, for details), as well as spectroscopic follow-ups (Cimatti et al. 2002; Cowie et al. 2004; Vanzella et al. 2005).
The GOODS southern (GOODS-S) pointing has been the target of extensive observation with ESO telescopes, carried on in the spirit of public surveys. Near infrared observations with the VLT-ISAAC infrared imager have been performed, leading to a final area covered by Ks images of ~ 140 arcmin^2 to a 1σ limiting depth of typically $26 - 27$ mag/arcsec^2 in the AB scale. Therefore, the GOODS-S survey is characterized by a unique combination of
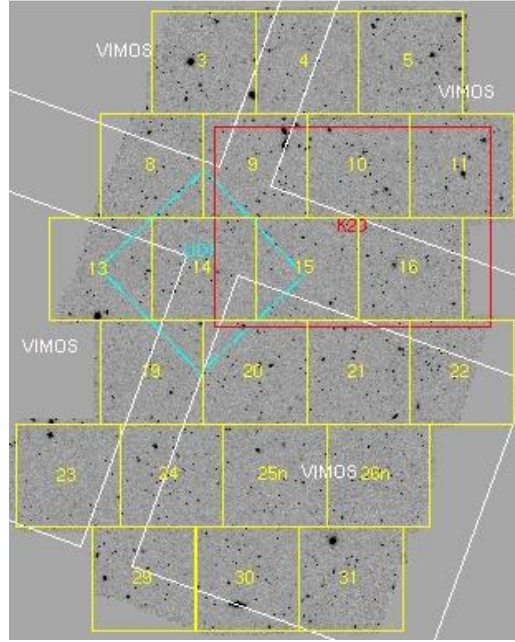
Figure 3.3: Layout of the GOODS-MUSIC field (from Grazian et al. 2006).

depth and size in the near infrared band.

The GOODS-MUSIC catalog

GOODS-MUSIC (Grazian et al. 2006; Santini et al. 2009) is a project that aims to create a multiwavelength catalog with spectroscopic and photometric information for galaxies included in a large area in the GOODS-S field where deep near infrared observations performed with ESO-VLT are available.

This catalog has entirely been realized using public data, and spans the wavelength range between 0.3 and 24 μm, for a total of 15 photometric bands. The field covered by the survey has an area of ~ 143.2 arcmin^2.

The galaxies have been selected in three different bands (z, K, and IRAC 4.5 μm), with a completeness level of 90% for $z < 26$, $Ks < 23.8$ and $m_{4.5\ \mu m} < 23.5$ in the AB-magnitude scale. A cross-correlation with spectro-

scopic catalogs available to date was performed, allowing to assign a spectroscopic redshift to over 3000 sources in the catalog.

The final catalog contains 15208 sources, including 209 known stars ad 61 AGN. The authors also applied a photometric redshift code to the data set, and showed that the comparison with spectroscopic redshifts available is quite good, with an average scatter of 0.05.

The mid-infrared 24 μm fluxes were derived from MIPS images. The source extraction has been performed using the z-band position as a prior to detect the 24 μm position for each source, taking advantage of the much higher resolution of the ACS-*HST* camera with respect to the MIPS image (PSF$\sim 0.12''$ for ACS vs $\sim 5.2''$ for MIPS). A total of 3313 sources were detected in the 24 μm band, while for the other 11841 the catalog contains only a 1σ upper limit.

The whole area surveyed by GOODS-MUSIC catalog is contained in the Chandra Deep Field South (CDFS) field. The CDFS is the deep *Chandra* X-ray survey performed to date, and covers an area of ~ 464.5 arcmin^2. The observations consist of 54 ACIS-I pointings, that have been taken between 1999 October and 2007 November (for the first 23; Alexander et al. 2003; Luo et al. 2008) and, more recently, between 2010 March and 2010 July (for the last 31 pointings), for a total exposure time of 4 Ms (Xue et al. 2011).

The CDFS 4 Ms X-ray catalog contains 740 sources detected in at least one band. This catalog reaches extremely faint X-ray flux limit in both soft ($0.5-2$ keV, 9.1×10^{-18} erg s^{-1} cm^{-2}) and hard ($2-8$ keV, 5.5×10^{-17} erg s^{-1} cm^{-2}) bands.

In the sample used for this work, the 1852 sources with a 24 μm flux brighter than 20 μJy have been included. This selection allows to avoid the contamination from spurious detection that may be included in the GOODS-MUSIC catalog down to very faint fluxes (a detailed discussion of this topic can be found in Magnelli et al. 2011). 1546 sources out of 1852 have a K-band

counterpart; for 1509 out of these 1546 sources, a redshift measurement is also available, either spectroscopic (734) or photometric (775). The remaining 37 K-band detected sources do not have a secure redshift determination. For 306 of the 24 μm selected sample a K-band counterpart was not found. A redshift is available for 114 sources (82 secure spectroscopic redshifts and 32 photometric redshifts), while the remaining 192 sources do not have any redshift estimation.

3.2.3   SED fitting

Highly obscured AGN are usually characterized by a strong mid infrared luminosity, due to the dust reprocessing of the UV emission, but, relatively faint UV, optical and near infrared emission (see Fiore et al. 2009, and references therein). The nuclear contribution to the whole galaxy spectral energy distribution (SED) has a minimum at 1 μm and grows towards higher wavelengths; the peak of the AGN contribution is seen at lower wavelengths with respect to the galaxy (stellar) contribution. We therefore chose the rest-frame 5.8 μm band in order to maximize the AGN contribution to the whole SED.

Starting from a sample of 24 μm selected galaxies, we define the 5.8 μm luminosity as

$$L_{5.8} = \nu_{5.8} L_{\nu_{5.8}} = \nu_{5.8} 4\pi d_L^2(z) F_{24} K_{24,5.8}(z) \tag{3.5}$$

where $K_{24,5.8}(z)$ is the K-correction matrix between 24 and 5.8 μm.

In order to obtain accurate 5.8 μm luminosities for the whole infrared-selected sample, we fitted the observed photometric measurements using a library of 46 empirical template SED (see Salvato et al. 2009; Fiore et al. 2009, and references therein).

The SED fitting has been carried out by fixing the redshift to the already available spectroscopic or photometric estimates and using the IRAC (3.6,

4.5, 5.8 and 8.0 μm) and 24 μm bands, increasing the uncertainties on the first three IRAC bands up to 0.5 mag, in order to weight more the 8.0 and 24 μm bands during the fit. This approach provides good results at redshifts larger than 0.35 (since at $z > 0.35$ the rest-frame 5.8 μm luminosity is emitted at wavelengths larger than 8 μm).

The SED fitting procedure described in this section has been performed using the fitting code LePHARE from S. Arnouts and O. Ilbert (Arnouts et al. 1999; Ilbert et al. 2006). LePHARE (Photometric Analysis for Redshift Estimate) is a set of FORTRAN programs to compute photometric redshift using SED fitting techniques. The package is composed of three parts:

- a preliminary phase used to select the SED models library and the set of filters used, and to compute a matrix of template magnitudes; all these operations are carried out separately using stand-alone programs;

- the main phase, which computes the photometric redshifts using a simple χ^2 routine;

- the last module, that allows to generate realistic multicolor catalogs taking into account observational effects.

The SED library has been built with a total of 46 empirical templates (Figure 3.4). Our library is based of the SED templates presented in Salvato et al. (2009), which contains templates from SWIRE, including elliptical and spiral galaxies, starbursts, ULIRG, low-luminosity AGN and QSO (from Polletta et al. 2007), and a set of hybrid templates constructed by combining an AGN SED (TQSO1 and QSO2 templates) and a host galaxy SED (starburst and S0 template) and varying the ratio between both component (from 90:10, 80:20, ... , to 10:90). This library has been integrated with other empirical and synthetic templates from Fiore et al. (2008), and 4 new starburst templates
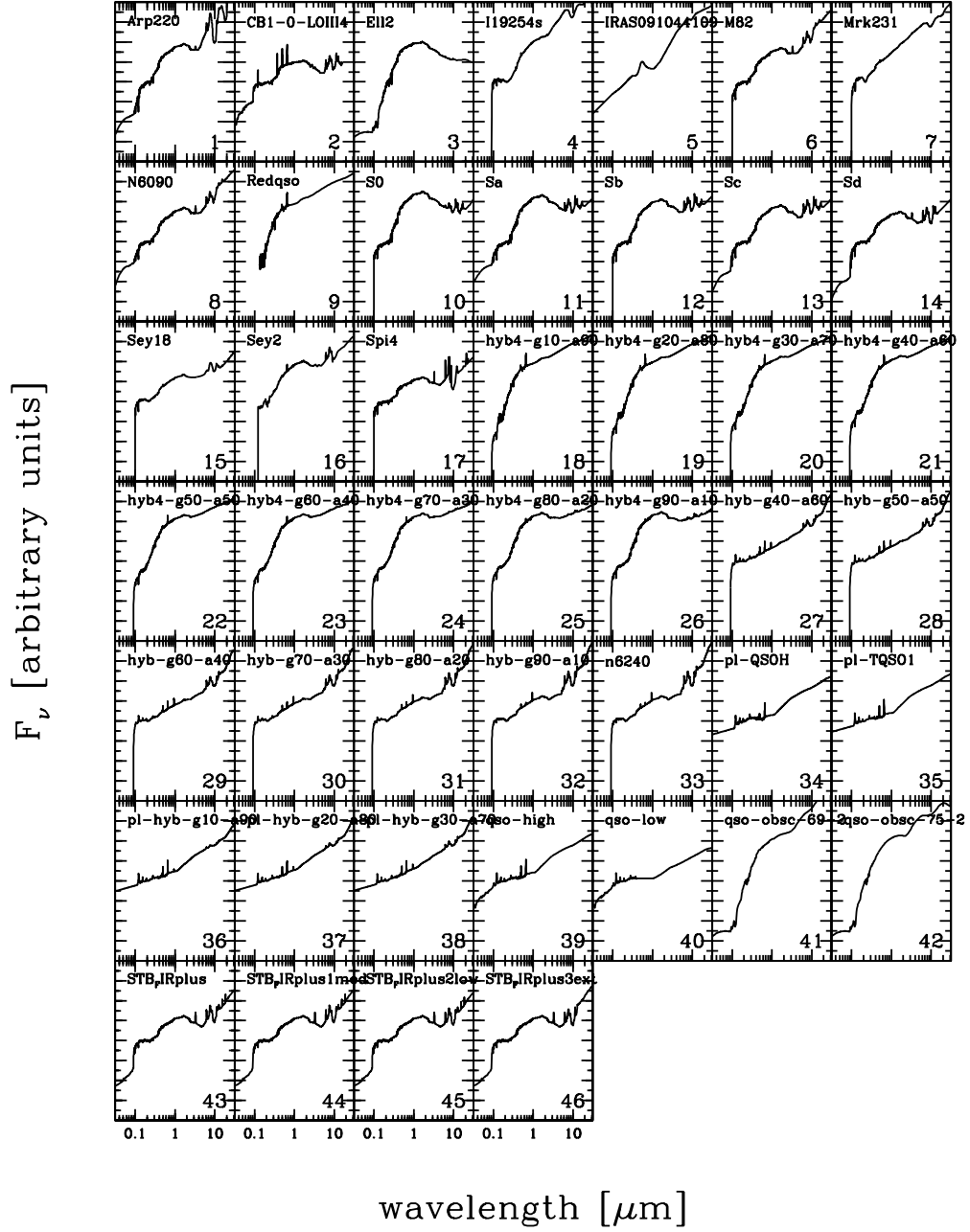
Figure 3.4: Library of the 46 empirical template SED used in the fitting routine.

(models 43-46 in Figure 3.4; Sacchi 2008), with a higher flux at wavelengths $\lambda > 10\mu$m.

Once the SED library and the set of filters have been defined and the matrix of template magnitudes has been generated, the main fitting routine can be invoked. Since in this computation only the 5.8 μm luminosities have to be found, input values for the redshift of each galaxy have been given to the code as a prior and have been fixed to the observed values. The output produced by the fitting code includes the 5.8 μm luminosity and the best-fit SED template for each source.

3.3 The mid infrared LF

The accuracy of the 5.8 μm luminosity estimations is a critical issue of this part of the work. Before proceeding in the analysis, we have carried out several tests to probe the accuracy of these estimations.

The main of these checks has been the capability of our COSMOS data-set to reproduce the infrared luminosity function of galaxies. The result of this computation is worth a brief discussion; it should be noted, however, that the estimation of the infrared LF of galaxies is a topic that goes beyond the aims of this thesis.

In order to compute the number density of galaxies we have divided our data-set in several $L_{5.8} - z$ bins. In each of these bins, we have made use of the classical $1/V_{max}$ method (Schmidt 1968).

Let us suppose that in a $L_{5.8} - z$ bin there are N sources within $L_{5.8} \pm \Delta L$ and $z \pm \Delta z$. For each of these sources, we define the comoving volume $V_{\mathrm{co},i}$:

$$V_{\mathrm{co},i} = \Delta\Omega_i[V'_{\mathrm{co}}(z + \Delta z) - V'_{\mathrm{co}}(z - \Delta z)], \qquad (3.6)$$

where V'_{co} is the comoving volume per unit solid angle (see Appendix C.11). When the survey flux limit cuts across the bin, the limits on redshift (Δz)

must be adjusted to reflect the range within which that particular object could have been found, given its luminosity. The resulting volume is called the *accessible volume*. The volume density of the sources is then given by the following expression:

$$N(L, z) = \sum_{i=1}^{N} \frac{1}{2\Delta L V_{\mathrm{co},i}}. \qquad (3.7)$$

When the survey limit does not cut across the bin, $2\Delta L$ is the full luminosity width of the box; when it does, it is the range of luminosities within which the i-th object could have been found.

Using this technique, we have computed the volume density of 24 μm selected sources in our sample. The results of this computation are shown in Figure 3.5. We compared our results with the estimations from Rodighiero et al. (2010). These authors made use of a combination of 24 μm selected data from *Spitzer* observations in the VIMOS VLT Deep Survey (VVDS-SWIRE) and GOODS areas, and presented a set of mid infrared and bolometric luminosity functions up to redshift $z = 2.5$, in the 8, 12, 15 and 24 μm bands. Although 5.8 μm band was not available, the 8 μm luminosity function, due to its proximity, resulted to be a good approximation for a comparison with our estimates.

The blue points in Figure 3.5 represent the 8.0 μm luminosity function data points from Rodighiero et al. (2010). It should be noted that these points are not measured in luminosity bins coincident with ours, although very similar; for this reason, we reported in Figure 3.5 the mean luminosity for each of the $L_{8.0}$ bins from Rodighiero et al. (2010). This comparison shows that our data fairly well reproduces the trends in the luminosity function and confirms the good accuracy of the SED fitting procedure that has been built.
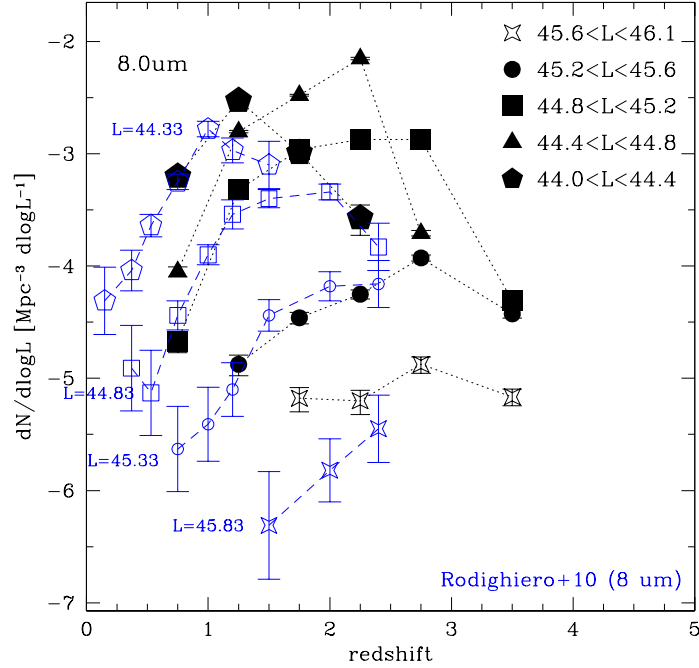
Figure 3.5: Number density at 5.8 μm of 24 μm selected galaxies in the COSMOS sample (black points). Blue points represent the estimations from Rodighiero et al. (2010) in the 8 μm band.

3.4 X-ray/radio matched data-set

As our objective, described in Chapter 4, is to use the distribution of the ratio between the AGN radio and $2 - 10$ keV luminosities in order to estimate the kinetic (radio) luminosity of the X-ray selected AGN, we had to measure a radio emission which was as much as possible causally linked (contemporary) with the observed X-ray activity (accretion). We then decided to measure the radio fluxes in a region as closest as possible to the AGN, therefore minimizing the contribution of objects like the radio lobes in FRII sources (Fanaroff & Riley 1974). For this reason we built up a large data-set of X-

ray selected AGN (where redshift and N_H column densities estimates were available) observed at 1.4 GHz with a $\sim 1''$ typical spatial resolution (in our cosmology $1''$ corresponds, at maximum, to about 8 Kpc at $z \sim 2$; see Appendix C).

3.4.1   The bright sample

In order to build up a large unbiased bright AGN (low redshift) sample, we joined the AGN samples recently generated from the *SWIFT* and *IN-TEGRAL* missions with the sample published by Grossan (1992) using the *HEAO*-1 data. In the case of sources in common, priority was given first to the *SWIFT* data and then to the *INTEGRAL* ones and lastly to the sample of Grossan (1992).

The radio information was obtained via cross-correlation with the 1.4 GHz radio data taken from the FIRST VLA survey (Becker, White & Helfand 1995). The FIRST images have $1.8''$ large pixels, a typical rms sensitivity of 0.15 mJy and a resolution of $5''$. In the case of no radio detection a 5σ upper limit of 0.75 mJy was adopted. The large area NVSS (Condon et al. 1998) and SUMSS/ATCA (Mauch et al. 2003) radio surveys have positional uncertainties significantly larger than FIRST and therefore were not used in our analysis.

SWIFT

The *SWIFT* sample we used is composed by 121 sources with high galactic latitude ($|b| > 15°$) and detected with $14 - 195$ keV fluxes brighter than 10^{-11} erg s^{-1} cm^{-2} (Tueller et al. 2008). All but one of the 121 sources have a redshift and an optical spectroscopic classification available (Tueller et al. 2008). 44 out of the 121 sources have been observed by FIRST. We limited our analysis to the 40 sources with $2 - 10$ keV unabsorbed X-ray luminosity

higher than 10^{42} erg s^{-1}: there are 18 broad optical emission line type 1 and 1.5 AGN (AGN1/1.5), 13 narrow emission line type 2 AGN (AGN2), 2 galaxies and 7 BL Lac in this sub-sample. In this and in all the other samples, all the BL Lac were excluded from our analysis as their radio fluxes are strongly amplified by the boosting of the relativistic radio jets. Therefore the AGN sample we used is composed by 33 sources in total (28 detected by FIRST). N_H column densities measures were provided by Tueller et al. (2008).

INTEGRAL

We tried to complement the *SWIFT* data with the catalog of 46 sources detected by *INTEGRAL* at a 5σ significancy level by Beckmann et al. (2006). However, after removing two sources without N_H measurements (from Sazonov et al. 2007), and 21 sources already included in the *SWIFT* sample, we ended with 18 sources which were not covered by the FIRST radio observations. Therefore, no source from the *INTEGRAL* catalog from Beckmann et al. (2006) was included in our analysis.

Grossan

The bright sample was eventually complemented with the sample of the $HEAO-1$ sources described by Grossan (1992) as revised by Brusadin (2003). Brusadin (2003) investigated, from the total sample of Grossan (1992), those 74 sources with $2-10$ keV fluxes brighter than 2×10^{-11} erg s^{-1} cm^{-2} . For 52 of these 74 sources the original optical counterparts were observed in the hard X-rays by at least one among the *ASCA*, *Beppo-SAX* and *XMM-Newton* satellites. All the counterparts resulted to be real hard X-ray sources and a new estimate of the N_H column densities were derived. We used in this work a sub-sample of 66 objects, from the sample of Brusadin (2003),

for which reliable measure of the N_H column densities were available.

Forty-one out of these 66 sources are not included in the *SWIFT* sample, and ten (10 AGN1/1.5) of them were observed by FIRST and have $2 - 10$ keV X-ray unabsorbed luminosities higher than 10^{42} erg s^{-1}. Nine out of these last ten sources were also detected in the radio band by FIRST.

In summary, the bright sample contains 43 X-ray sources (28 AGN1, 13 AGN2, 2 galaxies; once the BL Lac were excluded) observed in the 1.4 GHz radio band by FIRST, with 37 detections.

3.4.2   The *ASCA* surveys: AMSS and ALSS

Two samples from the *ASCA* satellites were included in this work. The first one comes from the *ASCA* Large Sky Survey (ALSS), a contiguous 7 deg^2 strip in the North Galactic Pole region (Ueda et al. 1999). We selected a sample with a limiting $2-10$ keV flux of 1×10^{-13} erg s^{-1} cm^{-2} from Akiyama et al. (2000). This sample contains 30 AGN (25 AGN1, 5 AGN2), as well as two clusters, one star and one object without spectroscopic identification, which were excluded from our analysis. All the 30 AGN were observed by FIRST, while nine were detected.

3.4.3   HBSS

We used the 67 sources of the *XMM-Newton* Hard Bright Sensitivity Survey (HBSS; Della Ceca et al. 2004) with $4.5 - 7.5$ keV fluxes brighter than 7×10^{-14} erg s^{-1} cm^{-2} (which corresponds to a $2 - 10$ keV limit of 3.5×10^{-13} erg s^{-1} cm^{-2} if a spectral index $\alpha = 0.7$, where $F_\nu \propto \nu^{-\alpha}$, is assumed). A subsample of 62 sources were used in our analysis after the exclusion of 2 stars, one cluster and 2 sources without a spectroscopic identification. Thirty-two sources were observed by FIRST (23 AGN1, 9 AGN2), while 6 were detected.

3.4.4 *XMM*-COSMOS

Data products from the COSMOS survey were also included in this part of our work. We used the XMM-Newton X-ray catalog by Cappelluti et al. (2009) with a limiting 2-10 keV flux of $\sim 3 \times 10^{-15}$ erg s^{-1} cm^{-2} and cross-correlated it with the spectroscopic identifications by Trump et al. (2009) and Brusa et al. (2010), and the photometric redshift estimates from Ilbert et al. (2009) and Salvato et al. (2009). The N_H measures were derived by our analysis of the hardness ratios.

The radio data were obtained from Schinnerer et al. (2007). In order to allow a uniform radio coverage (with 1.4 GHz rms of 15 μJy) the central 1 deg^2 squared area with limits $9^h 58^m 40^s < \alpha < 10^h 2^m 40^s$ and $1°42' < \delta < 2°42'$ was used. In this area the X-ray catalog contains 712 sources: 677 are extragalactic with a redshift measure available and $2 - 10$ keV luminosity higher than 10^{42} erg s^{-1}; 389 have a spectroscopic redshift (186 AGN1, 52 AGN2, 71 emission line galaxies, ELG, 32 normal passive galaxies, GAL, 48 no class), while 288 have only a photometric redshift estimate available. We used all the radio detections with 1.4 GHz flux limits brighter than 75 μJy (5σ) and used the same threshold as an upper limit for all the remaining sources even though lower flux detections were available in some cases. In total 141 out of the 677 sources, contained in our selected region of the COSMOS field, were detected in the 1.4 GHz radio band.

3.4.5 ELAIS-S1

In the European Large Area *ISO* Survey field S1 (ELAIS-S1) we used the catalogue of the *XMM-Newton* sources published by Puccetti et al. (2006), which reaches a $2 - 10$ keV flux limit of 2×10^{-15} erg s^{-1} cm^{-2}. The spectroscopic identifications and classifications provided by Feruglio et al. (2008) and Sacchi et al. (2009) were used, while the 1.4 GHz radio data (with a

5σ limit of 150 μJy) were taken from Middelberg et al. (2008). The whole sample contains 421 extragalactic sources with a redshift measure available and $2-10$ keV luminosity higher than 10^{42} erg s^{-1}: 240 have been identified and classified spectroscopically (116 AGN1, 34 AGN2, 68 ELG, 22 GAL), while 181 have a photometric redshift available. Forty-five out of these 421 AGN were detected at 1.4 GHz above the 150 μJy limit.

3.4.6 CLANS

In the *Chandra* Lockman Area North Survey (CLANS) field the X-ray data were taken from Trouille et al. (2008), which also publish the spectroscopic and photometric redshift measures. Our sample consists of the sources with SNR>3 detections in the hard $2-8$ keV band and included in the circular area centered in $(\alpha, \delta) = (10^h46^m, 59°01')$ with a radius of 0.32 deg. This area contains 139 extragalactic sources with a redshift measure available and $2-10$ keV luminosity higher than 10^{42} erg s^{-1}: 113 sources were spectroscopically identified (58 AGN1, 34 AGN2, 16 ELG, 5 galaxies), while 29 sources have a photometric redshift available. The N_H measures were derived from the analysis of the hardness ratio.

Radio data were obtained from Owen & Morrison (2008). We conservatively modeled the spatial dependence of the (5σ) radio flux limits, which vary from 18.5 μJy in the central region up to 59.2 μJy near the edges. Sixty-nine out of the 139 sources were radio-detected.

3.4.7 CDFS

In the *Chandra* Deep Field South the subsample of the GOODS-S X-ray sources from the catalog of Alexander et al. (2003) was used. The whole sample consists of the 94 point like extragalactic sources over a $2-10$ keV flux limit (at the aim point) of 2.6×10^{-16} erg s^{-1} cm^{-2} with a redshift

measure available and a $2 - 10$ keV luminosity higher than 10^{42} erg s^{-1}. Spectroscopic identifications for 69 sources, as well as 25 photometric redshifts, were obtained from Brusa et al. (2009b). Twenty-nine sources were identified as AGN (17 AGN1, 12 AGN2), 39 as ELG and one as a galaxy. The radio data were taken from Miller et al. (2008) and have a 1.4 GHz 5σ flux limit of 70 μJy. Twelve sources were radio-detected.

3.4.8 CDFN

In the *Chandra* Deep Field North we used the 296 $2 - 8$ keV X-ray sources detected within the GOODS-N area with a $2 - 10$ keV flux limit (at the aim point) of 1.4×10^{-16} erg s^{-1} cm^{-2} by Alexander et al. (2003). To convert the $2 - 8$ keV fluxes in the $2 - 10$ keV band a spectral index $\alpha = 0.4$ were assumed. The spectroscopic identifications were taken from Trouille et al. (2008). The sample consists of 162 extragalactic sources with a redshift measure available and $2 - 10$ keV luminosity higher than 10^{42} erg s^{-1}: 104 sources were spectroscopically identified (16 AGN1, 20 AGN2, 46 ELG, 22 galaxies), while 50 sources have a photometric redshift; eight other spectroscopical redshift were retrieved from literature. N_H absorption values were obtained from the analysis of the hardness ratio.

The radio information were obtained from the new data reduction from Biggs & Ivison (2006) of the 1.4 GHz VLA observation of Richards (2000). Forty-five out of the 162 extragalactic sources were identified in the 1.4 GHz band over a (5σ) flux limit of 45 μJy.

3.4.9 The final sample

The cross correlation of the X-ray and radio catalogs was carried out inside a region with $5''$ of radius (almost less than or equal to the size of the central part of a galaxy like ours), following a maximum likelihood algorithm as
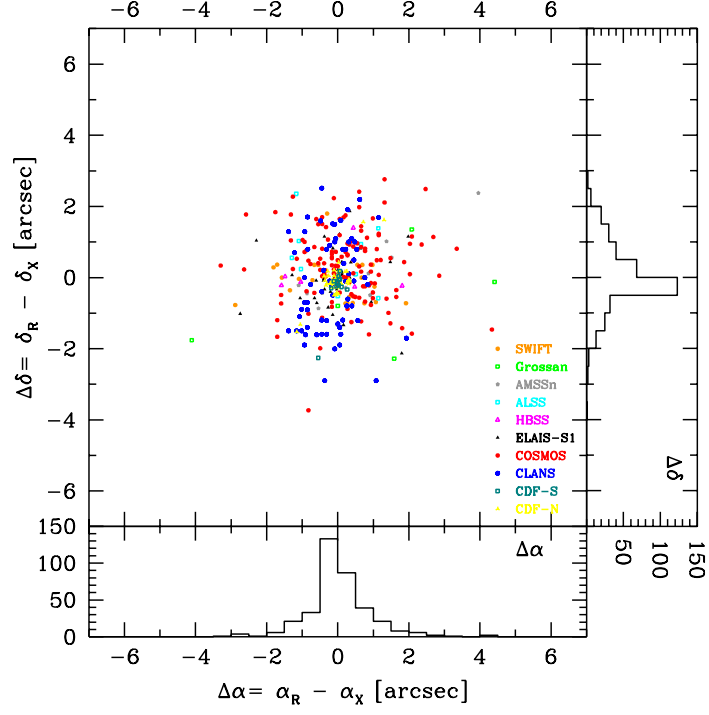
Figure 3.6: Distribution of the off-sets between the cross-correlated radio and X-ray sources

described by Sutherland & Saunders (1992) (see also Ciliegi et al. 2003, and Section 3.2.1).

In Figure 3.6 we show the off-sets between the X-ray and radio positions of the whole sample. These resulted to have a root mean square (rms) of 1.4″. Therefore we expect to have (properly) preferentially included compact FRI radio sources in our cross-correlation and have excluded most of the contribution of the (especially bright) extended FRII radio lobes from our analysis (see Section 4.2.4 for a discussion on the contribution of the excluded FRII sources to the radio counts).

The total AGN sample was built up from a compilation of complete (i.e. with almost all redshift and N_H measures available) hard (mostly $2 - 10$ keV) X-

ray selected samples, with unabsorbed $2 - 10$ keV luminosities higher than 10^{42} erg/s.

3.5 Summary

3.5.1 The mid-infrared sample

The whole 24 μm sample that has been built as described in Section 3.2 consist in 16 409 mid infrared selected galaxies: 14 903 sources from COSMOS with $F_{24} > 80$ μJy and 1506 sources from GOODS with $F_{24} > 20$ μJy. The distribution of the sources on the 5.8 μm luminosity-redshift plane is shown in Figure 3.7.

For both subsamples, a cross-correlation with the X-ray catalogs using a matching radius of $1.5''$ has been carried out; 926 sources from COSMOS resulted to have an X-ray counterpart, as well as 265 GOODS sources. Thus, 1191 24 μm sources out of 16 409 have an X-ray counterpart.

For both X-ray detected and undetected sources in the sample, the number of background-subtracted counts within 5 arcsec from the position of the infrared sources and the exposure times are known.

3.5.2 The radio/X-ray matched sample

In summary, the radio observed hard X-ray selected extragalactic sample discussed in Section 3.4 contains 1641 sources with both redshifts (either spectroscopic or photometric) and N_H column densities measured, and with unabsorbed $2 - 10$ keV luminosities higher than 10^{42} erg s^{-1}. Other X-ray samples, such as HELLAS2XMM (Fiore et al. 2003; Cocchia et al. 2007), the XMM/Lockman Hole (Brunner et al. 2008) and the XMM Medium Survey (Barcons et al. 2007), were not included in our work because unbiased, homogeneous and dedicated radio 1.4 GHz observations were not available.

In our final sample, 1003 sources have N_H higher than 10^{22} cm^{-2} (hereafter defined "X-ray absorbed"). 375 (23%) sources were detected in the 1.4 GHz radio band. See Table 3.1 for a summary of the main properties of all samples used. In Figure 3.8 we show the (5σ) radio 1.4 GHx flux limits of each survey as a function of their deepest $2-10$ keV X-ray flux limits.

The distribution of the de-absorbed X-ray luminosity of all sources (distinguished according to radio detection and X-ray absorption classes) as a function of redshift is shown in Figure 3.9.

Table 3.1: The X-ray/radio sample.

Sample	$N_{1.4}$[a]	N_X[b]	$N_{1.4}/N_X$	$F_{1.4}$[c]	F_X[d]	$F_{1.4}/F_X$
Bright	37	43	0.86	750	2×10^{-11}	-6.3
AMSS	11	43	0.26	750	3×10^{-13}	-4.5
ALSS	9	30	0.30	750	1×10^{-13}	-4.0
HBSS	6	32	0.19	750	3.5×10^{-13}	-4.5
COSMOS	141	677	0.21	75	3×10^{-15}	-3.5
CLANS	69	139	0.50	19	3×10^{-15}	-4.1
ELAIS-S1	45	421	0.11	150	2×10^{-15}	-3.0
CDF-S	12	94	0.13	70	2.6×10^{-16}	-2.4
CDF-N	45	162	0.28	45	1.4×10^{-16}	-2.3
Total	375	1641	0.23	...	...	...

[a]number of AGN detected at 1.4 GHz

[b]number of X-ray AGN observed at 1.4 GHz

[c]1.4 GHz flux limit in μJy

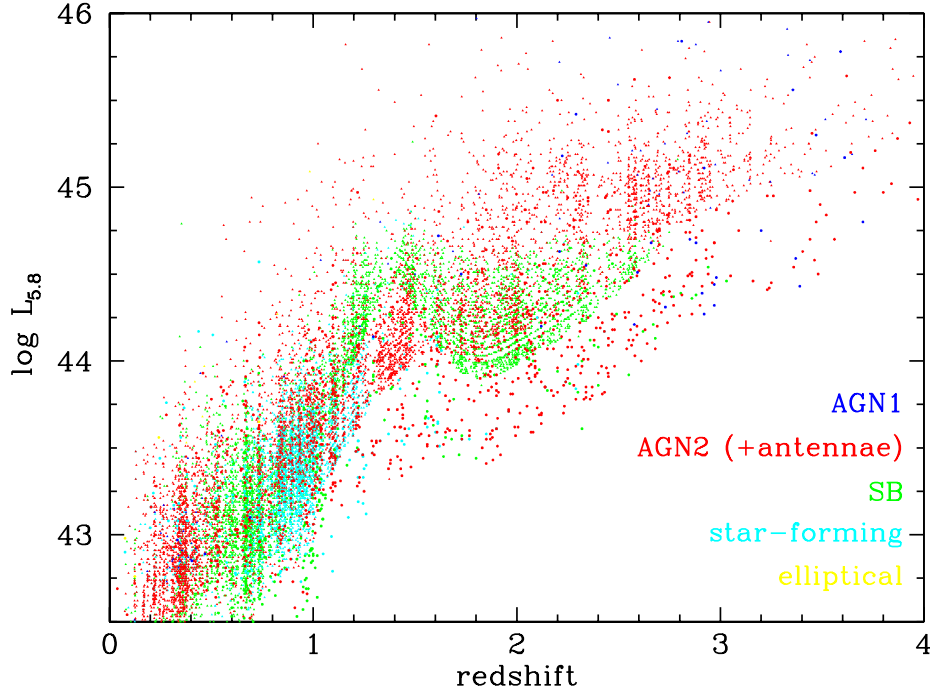[d]$2-10$ keV flux limit in erg s^{-1} cm^{-2}

Figure 3.7: Distribution of the 24 μm selected sources in the $L_{5.8} - z$ space. Different template models used for SED fitting are indicated with different colors.
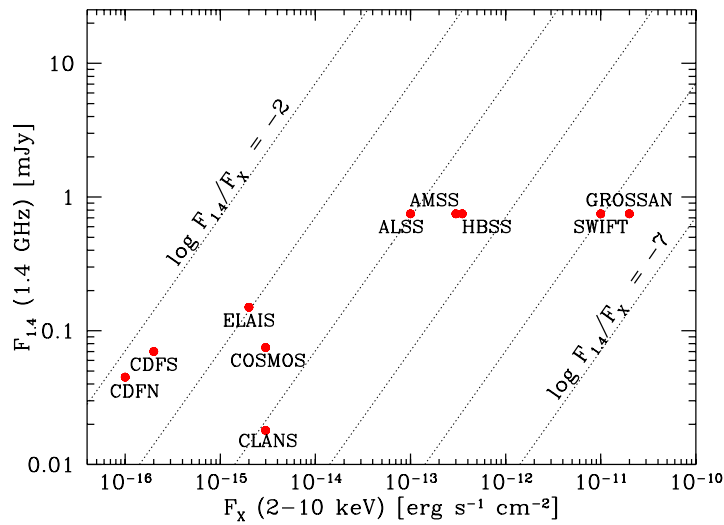

Figure 3.8: Lower 1.4 GHz flux limits as a function of the lower $2 - 10$ keV flux limits of the samples. Dashed lines show the loci with equal $\nu F_\nu (1.4 \text{ GHz})/F(2 - 10 \text{ keV})$ ratio as shown by the labels.
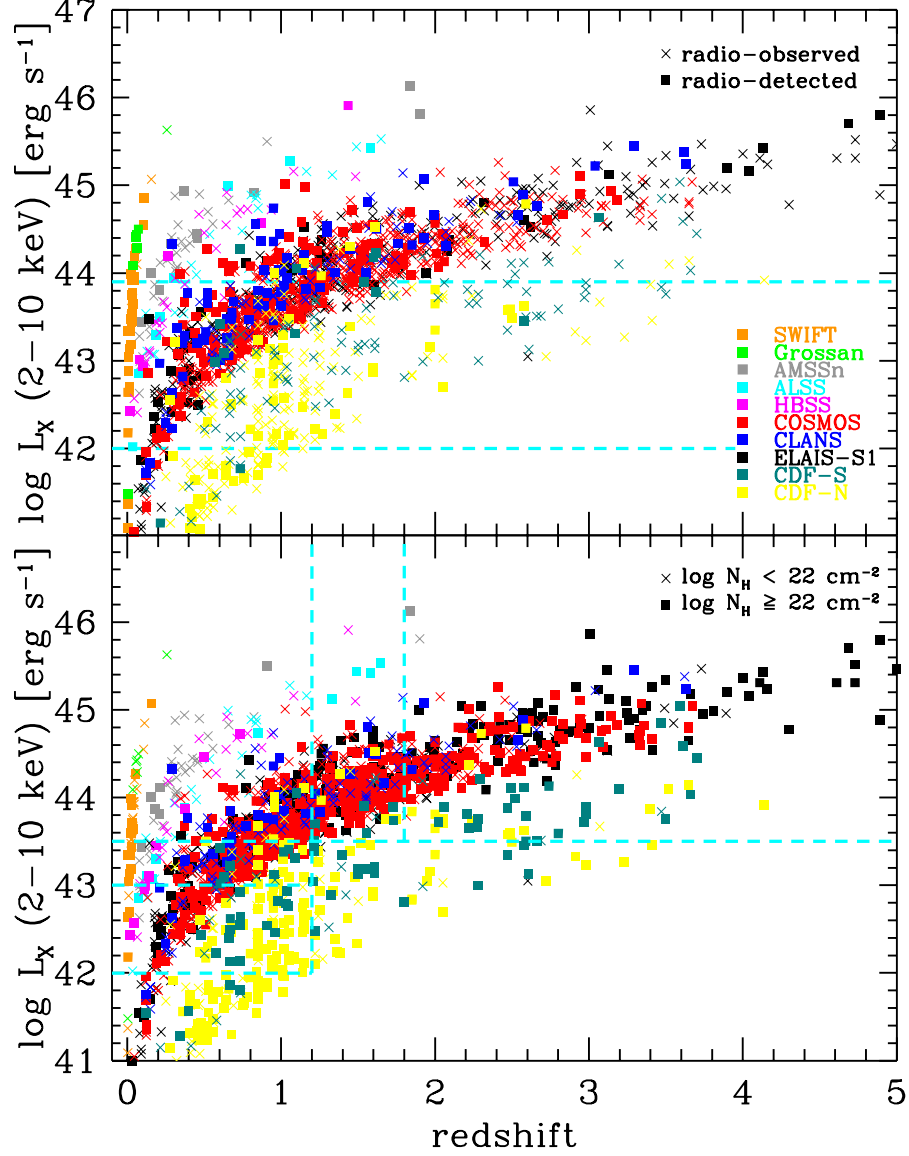
Figure 3.9: $2 - 10$ keV luminosity versus redshift for all AGN observed at 1.4 GHz used in this work. Top panel: observed (crosses) and detected (filled squares) sources at 1.4 GHz are shown; the dashed lines show the two regions used to measure the R_X distribution at $R_X < -4$ (see Chapter 4). Bottom: unabsorbed (crosses) and absorbed (filled squares) sources are shown; the dashed lines show the five regions used to measure the R_X distribution at $R_X > -4$.

Chapter 4

Radio loudness distribution and kinetic LF

4.1 Introduction

In the last few years, feedback from AGN has been invoked and included in semi-analytical models (SAMs), in order to quench the star formation in the most massive galaxies (see Section 2.7). However, it is still not completely clear how these feedback processes actually happen, i.e. if the feedback is at work mainly during luminous AGN phases (the *quasar mode*; see Menci et al. 2008), or if it proceeds continuously during the cosmic time at a low rate (the *radio mode*; Croton et al. 2006). In the latter scenario, the feedback process is assumed to be related to a low, uninterrupted and constant matter accretion rate onto the SMBH, coming from a quiescent inflow of gas coming from the halo's hot atmosphere (Monaco, Salucci & Danese 2000; Croton et al. 2006; Bower et al. 2006).

Even though this accretion rate is too small to contribute significantly to the bolometric output of AGN, it can drive powerful outflows of particles in relativistic jets, thus releasing significant amount of energy into the environment

in which the BH grows: the cooling, star-forming gas in the central region of the galaxy. These jets are also responsible for the large cavities in the intracluster medium that have been revealed in the X-rays (e.g. McNamara et al. 2000); it is then possible to derive the *kinetic power* of a radio source from the mechanical work (pdV) done by the jets to inflate these cavities (see Best et al. 2006; Bîrzan et al. 2008).

The aim of this work was to estimate the AGN kinetic power linking the AGN radio emission to the accretion rate related to the AGN activity (the luminous phase). A very useful ingredient is the measure of the probability distribution function $P(R_X)$ of the ratio R_X between the AGN radio and intrinsic $2 - 10$ keV luminosities:

$$R_X = \frac{\nu L_\nu (1.4 \text{ GHz})}{L_X (2 - 10 \text{ keV})}. \tag{4.1}$$

This probability distribution can be convolved with the X-ray LF in order to obtain a measure of the radio 1.4 GHz LF. If one further assumes a relation between radio and kinetic luminosities, it is possible to convert this radio LF into a kinetic LF.

4.2   Distribution of L_R/L_X ratio

Using the radio/X-ray matched data set described in Section 3.4, we searched for a functional fit of the probability distribution function of R_X, as a function of the X-ray luminosity, L_X, and the redshift: $P(R_X|L_X, z)$. The method is based on the comparison, through χ^2 estimators, of the observed and expected numbers of AGN (in the $L_X - z - R_X$ space) obtained by taking into account the observational selection effects (i.e. the radio flux limits) of each sample. Once a probability distribution function $P(R_X|L_X, z)$ is assumed, the number of expected AGN in a given bin of the $L_X - z - R_X$ space is the result of the sum, over the number of all AGN contained in the
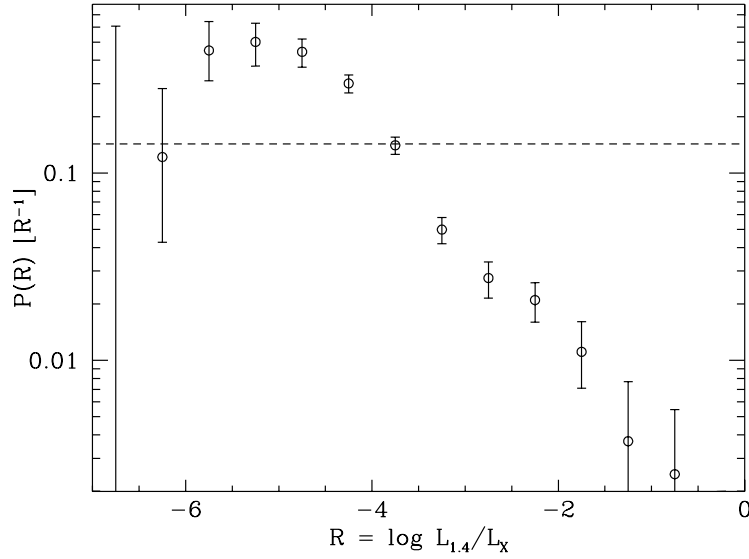
Figure 4.1: Probability distribution function of R_X for the full sample under the assumption of a flat distribution (dashed line).

$L_X - z$ bin, of the expected number of AGN contained in that bin of R_X, by taking into account the radio flux limits on each source. This method reproduces the observations and consequently properly takes into account both the radio detections and the upper limits (see La Franca et al. 1994; La Franca & Cristiani 1997; La Franca et al. 2002, 2005, for similar applications).

4.2.1 The fit

As a first test we assumed a constant (flat) probability distribution function of R_X in the range $-7 < R_X < 0$ (see Figure 4.1). This distribution, although different from the true one, allows to see which is the shape of the average true distribution via the analysis, in each bin, of the deviations of the observed numbers of AGN from the expected ones. Figure 4.1 shows that the average distribution function is asymmetrical with a long tail at large R_X values.

Table 4.1: Best fit parameters

Model	N	γ_R	γ_L	R_C	α_L	α_z	χ^2/d.o.f.	$P(\chi^2)$
1 - box	...	...	...	...	...	...	670.17/12	0
2 - no dep	1.0620	0.476	1.93	-4.313	...	...	46.73/20	6.4×10^{-4}
3 - dep z	1.0899	0.467	1.69	-4.319	...	0.028	41.98/19	0.020
4 - dep L	1.0652	0.429	1.70	-4.386	0.056	...	30.19/19	0.049
5 - dep L,z	1.0230	0.369	1.69	-4.578	0.109	-0.066	22.77/18	0.200
1σ errors		$+0.040$ -0.031	$+0.18$ -0.31	$+0.110$ -0.086	$+0.019$ -0.025	$+0.024$ -0.016		

After several trials, we found that the probability distribution function distribution of R_X is, indeed, asymmetrical, showing a maximum at $R_X = R_0$, where the median is located. At R_X larger than R_0 the distribution is fairly well represented by a Lorentz function having width γ_r, which provides a shallow decline at large R_X values, while at R_X smaller than R_0 the exponent 2 of the Lorentz function is better substituted by an exponent 4 which gives a wider shoulder at $R_X \lesssim R_0$ and then a steep decline at even lower R_X. The width of the left $(R_X < R_0)$ part of the distribution is controlled by the γ_l parameter. Therefore the probability distribution function $P(R_X|L_X, z)$ is expressed by the following formula:

$$P(R_X) = \begin{cases} \dfrac{N}{A\pi\gamma_l\left[1+\left(\frac{R_0(L_X,z)-R_X}{\gamma_l}\right)^4\right]} & (R_X < R_0) \\ \\ \dfrac{A\ N}{\pi\gamma_r\left[1+\left(\frac{R_X-R_0(L_X,z)}{\gamma_r}\right)^2\right]} & (R_X \geq R_0), \end{cases} \quad (4.2)$$

where, in order to obtain a continuous function at $R_X = R_0$ results $A = \sqrt{\gamma_r/\gamma_l}$, and the parameter N is constrained by the probability normalization requirement:

$$\int P(R_X|L_X, z)dR_X = 1. \quad (4.3)$$

For $0.3 \leq z \leq 3.0$ and $42.2 \leq \log L_X \leq 47.0$, we allowed to vary, as a function of L_X and z, the position of the maximum (median) R_0 of the distribution, according to the following formula:

$$R_0 = R_C \left[\alpha_L(\log L_X - 44) + 1\right] \left[\alpha_z(z - 0.5) + 1\right]. \tag{4.4}$$

At redshifts and luminosities outside these ranges, R_0 was kept constant, equal to the values assumed at the limits of the ranges.

In Table 4.1 the results of the fits carried out using this parameterization are reported. Confidence regions of each parameter were obtained by computing χ^2 at a number of values around the best-fit solution, while leaving the other parameters free to float (see Lampton et al. 1976). The 68% confidence regions quoted correspond to $\Delta\chi^2 = 1$.

The solution without dependences on both the luminosity and the redshift is rejected by the χ^2 test, while the solutions either depending only on luminosity or redshift provide barely acceptable fits to the data. A fairly good fit to the data (20% χ^2 probability) is instead provided by the solution #5 where both a dependence on the luminosity and the redshift is allowed. However, it should be noted that the parameter of the redshift dependence, α_z, is different from zero only at 3σ confidence level.

The data and the shape of the best fit #5 probability distribution function are shown in Figure 4.2, while the corresponding dependences of R_0 on L_X and z are shown in Figure 4.4. In Figure 4.3 we show the shape of the best fit #5 probability distribution function in different bins of X-ray luminosity and redshift, with evidence (the continuous lines) to the part which is actually constrained by the data.

4.2.2 Dependence on N_H

We did not find any significant dependence of the $P(R_X|L_X, z)$ distribution on the N_H column densities. The sample was divided into absorbed ($N_H >$
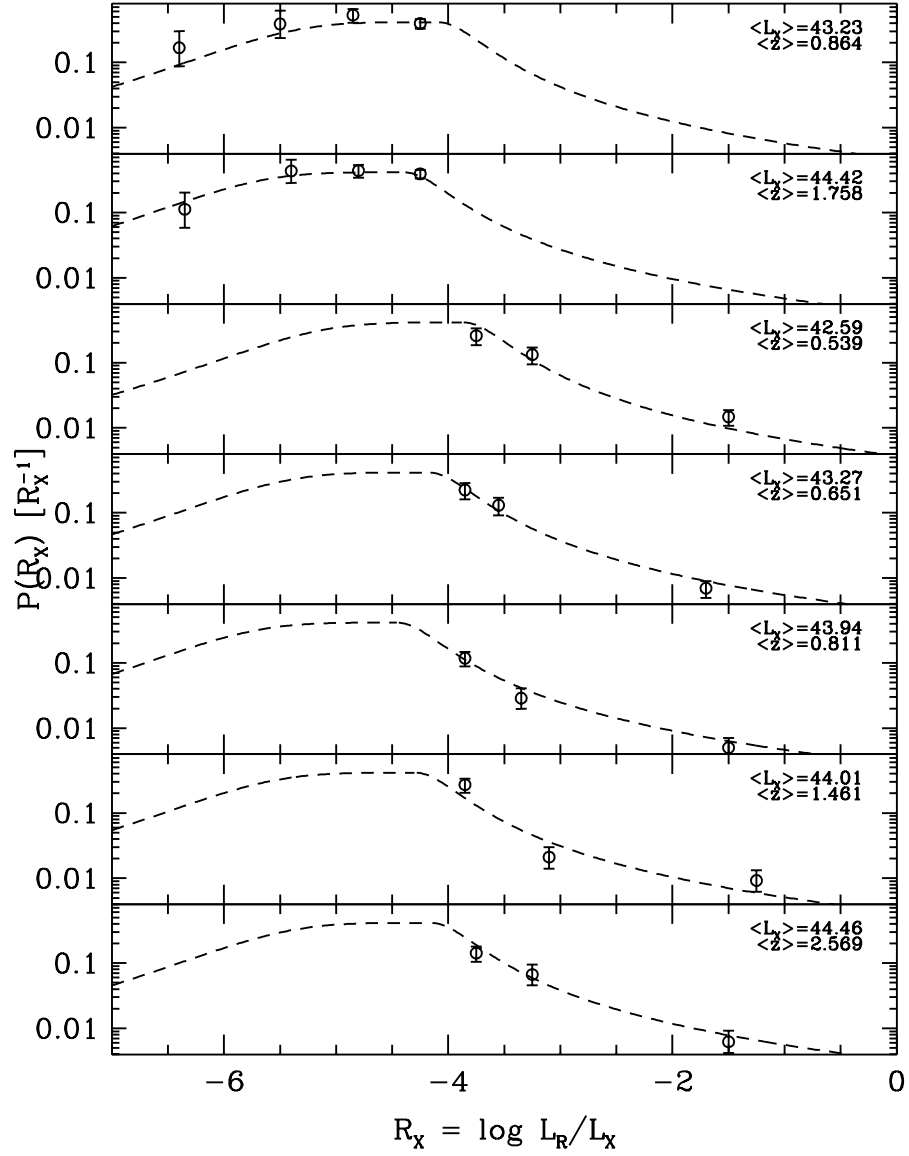
Figure 4.2: Probability distribution function of R_X in seven $L_X - z$ bins. The open circles represent the data points described in Section 4.2.1, while the dashed lines show (in each bin) our best-fit solution #5 (see Table 4.1).
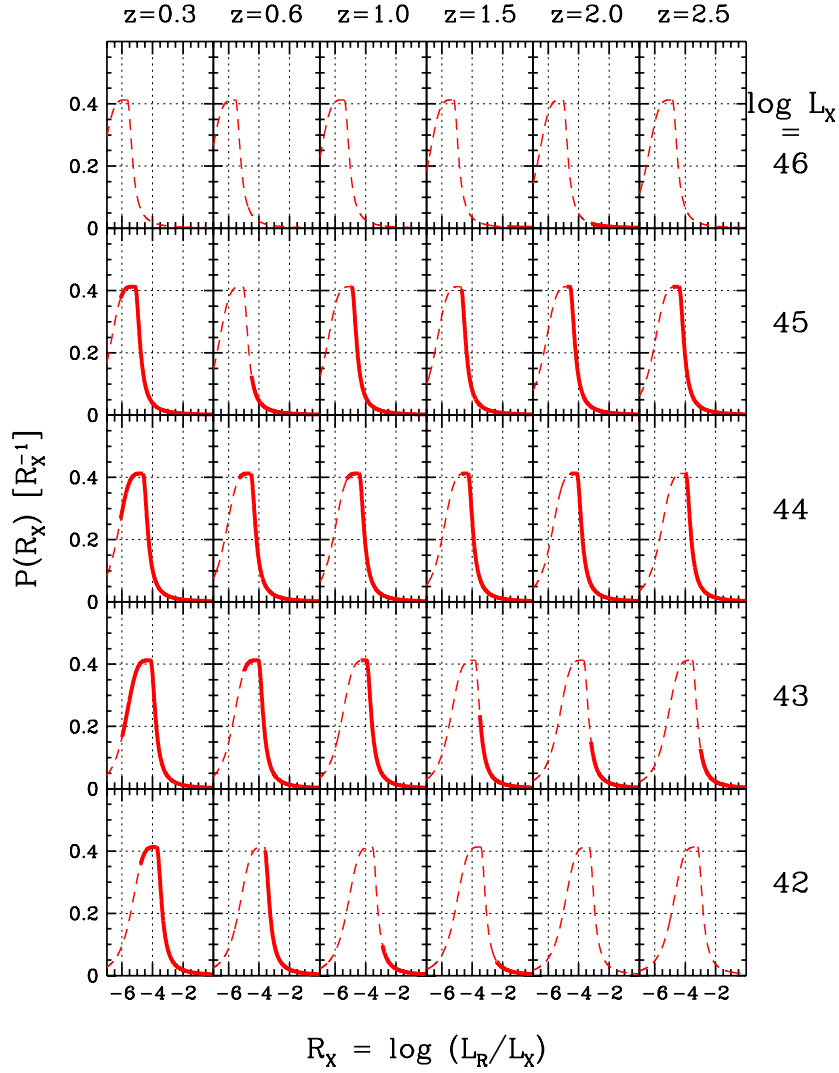
Figure 4.3: Probability distribution function in different $L_X - z$ bins, as computed in our best-fit solution #5. The solid line shows the range of R_X where the fit is constrained by the data, while the dashed line shows where the distribution is extrapolated.

10^{22} cm^{-2}) and unabsorbed AGN. For both sub-samples the χ^2 test on the best fit solution #5 (even with a different sampling in order to always observe
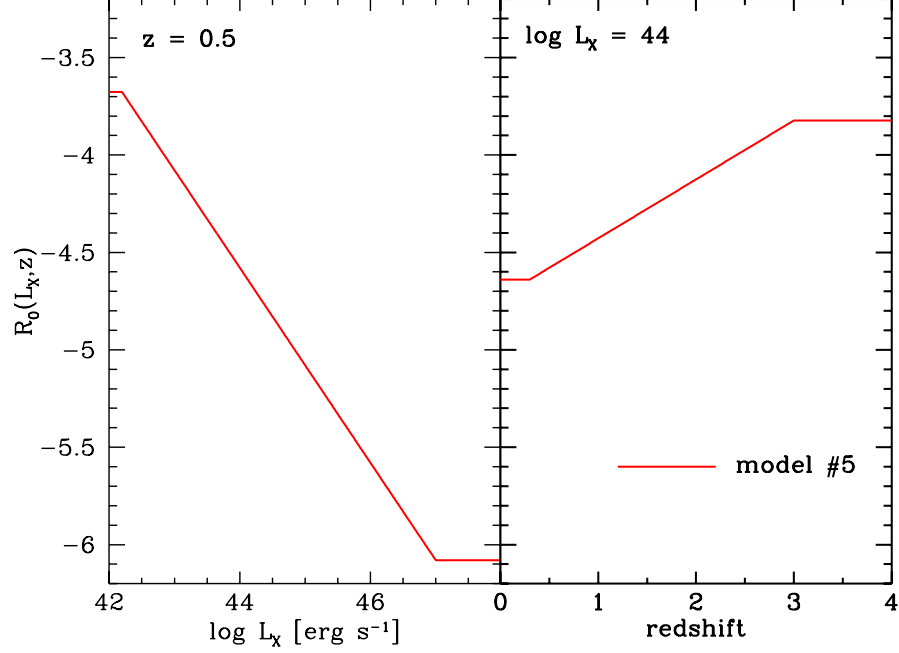
Figure 4.4: Dependence of the position of the median R_0 of the probability distribution function on L_X (left) and z (right) as computed in our best-fit solution #5 (red line).

at least 10 objects in each bin) provided probabilities larger than 10% (up to 70%), and was then not able to reject our best fit distribution. This result is in agreement with the analysis of the X-ray absorption properties of the faint radio sources of the CDFS by Tozzi et al. (2009).

4.2.3   The $L_R - L_X$ relation

We compared our measure of the probability distribution function of R_X with previous measures on the relationship between the AGN radio and X-ray luminosities. In Figure 4.5 we show the 1.4 GHz luminosity as a function of the intrinsic $2 - 10$ keV luminosity for all the sources of our sample. Our analysis differs from many previous studies where single general log-log linear

relations were derived. In these studies, even when the presence of censored data, or data with errors in both axes (see e.g. La Franca et al. 1995), were taken into account, it was assumed the presence of a symmetrical (usually Gaussian) distribution of the deviations from the best fit relation, which were attributed to an intrinsic scatter. Our method, instead, by taking into account all the censored data, allows to measure the *shape* of the distribution
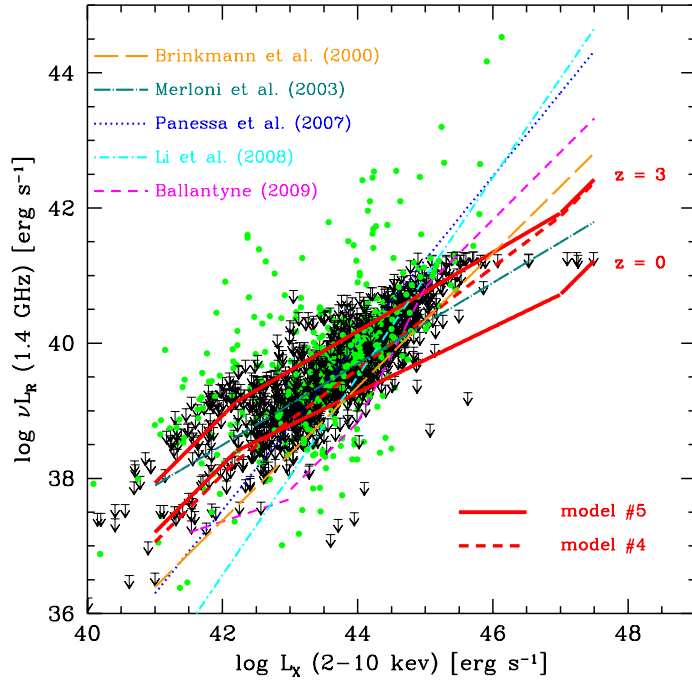

Figure 4.5: 1.4 GHz luminosity versus $2-10$ keV luminosity for all AGN in our sample. Radio detections are indicated by green dots, while radio upper limits are indicated by black arrows. The expected dependence from fit #5 (red continuous line) for $z = 0$ and $z = 3$ and from fit #4 (red dashed line) are shown and compared with Brinkmann et al. (2000, orange), Panessa et al. (2007, blue), Ballantyne (2009, magenta) $L_X - L_R$ relations and with Merloni, Heinz & Di Matteo (2003, green) and Li, Wu & Wang (2008, cyan) fundamental plane relations.

of the intrinsic scatter and its possible dependences on other variables (such as the luminosity and redshift in our case).

In Figure 4.5 we compare our best fit solution #5 with the relations derived by other authors such as Brinkmann et al. (2000) in the soft $0.5 - 2$ keV band (an X-ray spectral index α=0.7 was assumed to convert the $0.5 - 2$ keV luminosities into $2 - 10$ keV luminosities), Merloni, Heinz & Di Matteo (2003), Panessa et al. (2007), Li, Wu & Wang (2008) and Ballantyne (2009, for the radio quiet AGN) in the $2 - 10$ keV band. The relations by Merloni, Heinz & Di Matteo (2003) and Li, Wu & Wang (2008) were derived from their measure of the AGN fundamental plane (i.e. including also a dependence on the BH mass), assuming a fixed BH mass of 10^8 $M_\odot$.

As our measured distribution function is asymmetrical and depends on the redshift, the comparison is not straightforward (in Figure 4.5 we plot the position of the median R_0 of the distribution at redshifts 0 and 3). It results that our best fit solution #5 of the dependence of the 1.4 GHz luminosity on the $2 - 10$ keV luminosity is flatter than obtained in previous works. Our fitted relation corresponds to a power-law $L_R \propto L_X^\alpha$ with indexes $\alpha = 0.48$ and $\alpha = 0.58$ at redshifts 0 and 3, respectively. The relations fitted by the other authors have instead a wide range of power-law indexes ($0.6 \lesssim \alpha \lesssim 1.5$), systematically steeper than our result. This difference is partly caused by our new method used to measure the $L_R - L_X$ relation but it is also caused by our introduction (and measure) of a dependence on the redshift of the average R_X values. In fact, as shown in Figure 4.5, our solution #4, obtained without the inclusion of a redshift dependence, results in a steeper slope, having a power-law index $\alpha = 0.75$.

Figure 4.5 also shows that the fundamental plane by Merloni, Heinz & Di Matteo (2003) has a power-law index ($\alpha = 0.60$) close to our best fit estimate ($\alpha = 0.48 - 0.58$), and for BH masses of 10^8 $M_\odot$ is located between our best fit relations at redshift 0 and 3. In the fundamental plane estimate by Merloni,
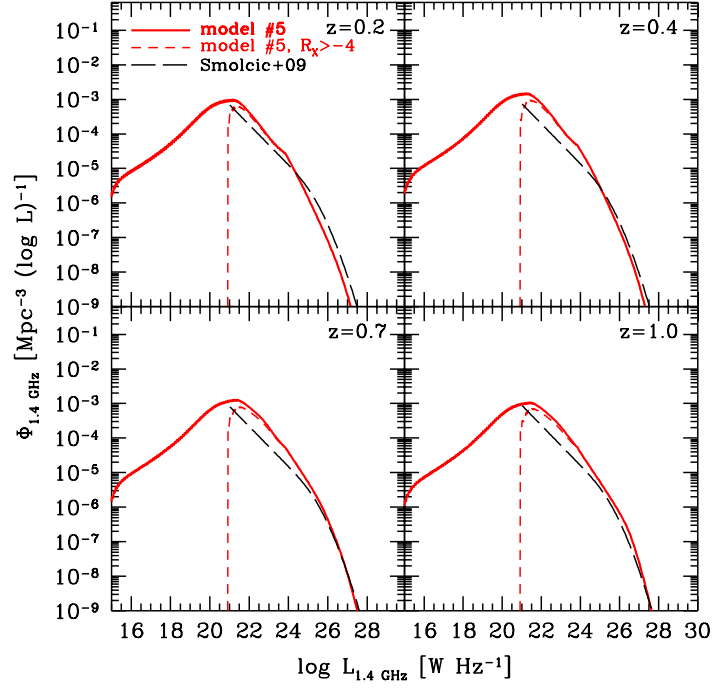
Figure 4.6: Predicted 1.4 GHz LF according to fit #5 for 4 redshift values (red continuous lines). The red dashed lines show the part of the LF reproduced by the $P(R_X)$ distribution for $R_X > -4$. The radio LF as estimated by Smolčić et al. (2009) is also reported (black dashed lines).

Heinz & Di Matteo (2003) R_X has also a dependence on the BH mass of the type $R_X \propto 0.78 \log M_{\rm BH}$. This implies that our estimates at redshift 0 and 3 are roughly similar to the fundamental plane measures for BH masses of 10^7 and 10^9 $M_\odot$, respectively. Therefore, as in our (and all flux limited) samples, high redshift AGN are on average more luminous, and thus probably host on average more massive BH, we can infer that our measure of the increase with the redshift of the median of the R_X distribution is qualitatively in agreement with the AGN fundamental plan measures where an increase of the average R_X with the BH masses is observed.

4.2.4　Sanity checks

The 1.4 GHz luminosity function

We verified if the measured probability distribution function of R_X, once convolved with the $2 - 10$ keV luminosity function, properly reproduces (taking into account the uncertainties) independent previous measures of the 1.4 GHz LF, $\Phi_R(L_{1.4}, z)$.

We used the $2 - 10$ keV luminosity function, $\Phi_X(L_X, z)$, as measured by La Franca et al. (2005), and modified by allowing a steep exponential decline of the AGN density at redshifts larger than $z = 2.7$, as measured by Brusa et al. (2009a). As discussed in La Franca et al. (2005), the density of Compton-thick AGN with $\log N_H = 24 - 26$ cm^{-2} was assumed to be equal to the density of the Compton-thin AGN with $\log N_H \leq 24$ cm^{-2} (this assumption resulted to properly reproduce the cosmic X-ray background). The X-ray LF can be converted into a radio LF by the formula:

$$\Phi_R(L_{1.4}, z) = \int P(R_X | L_X, z) \Phi_X(L_X, z) \mathrm{d} \log L_X. \qquad (4.5)$$

The X-ray LF was integrated starting from an X-ray luminosity $\log L_X = 41$ erg s^{-1}. The predicted radio LF is shown in Figure 4.6 and compared with the 1.4 GHz radio LF measured by Smolčić et al. (2009).

As discussed in Smolčić et al. (2009), this radio LF includes (like in our measure of the distribution of R_X) mostly the FRI sources. Although also affected by the uncertainties on the measure of the X-ray LF by La Franca et al. (2005), our best fit #5 of the probability distribution function of R_X provides a fairly good reproduction of the FRI radio luminosity function.

Contamination from star-forming galaxies

As a result of this computation, our estimate of the distribution of R_X allows to predict the AGN FRI radio LF at luminosities smaller than $L_{1.4} =$

10^{21} W Hz^{-1}, never probed before. However, at these low radio luminosities the AGN could be overwhelmed by the radio emission of the hosting galaxy because during periods of strong star formation activity the supernovae remnants accelerate cosmic rays which radiate synchrotron emission in local magnetic fields.

According to Ranalli, Comastri & Setti (2003), strong star forming galaxies ($\sim 10^2$ $M_\odot$ yr^{-1}) have about 10^{42} erg s^{-1} $2 - 10$ keV luminosities, and, in general, in all star forming galaxies a linear relation between the 1.4 GHz radio and the $2 - 10$ keV luminosities is observed, which corresponds to a value $R_X \simeq -2.0$. At face value this would imply that for the lowest luminosity AGN ($\log L_X \simeq 42 - 43$ erg s^{-1}) most of our measure of the $P(R_X)$ distribution (which spans in the range $-7 < R_X < -1$) could be contaminated if the hosting galaxies are undergoing a strong star formation activity.

However, as shown in Figure 4.3, at low R_X values the $P(R_X)$ distribution is mostly measured from AGN with $\log L_X = 43 - 45$ erg s^{-1}, and redshift lower than $z \sim 0.5$. At these low redshifts it is very unlikely for galaxies to harbor a star formation stronger than ~ 10 $M_\odot/$yr^{-1} (Elbaz et al. 2007; Noeske et al. 2007), which roughly corresponds to an emission in the $2 - 10$ keV band of $\log L_X \sim 41$ erg s^{-1} (Ranalli, Comastri & Setti 2003). Therefore, for example, in a low redshift AGN with $\log L_X \sim 44$ erg s^{-1}, having an hosting galaxy whose star formation emits a $2 - 10$ keV luminosity of $\log L_X \sim 41$ erg s^{-1}, the corresponding radio emission (having an intrinsic $R_X \simeq -2.0$) can contaminate our measure of the R_X distribution only for R_X values smaller than -5.

We can then conclude that only at the lowest R_X values ($\lesssim -5$) our measure of the $P(R_X)$ distribution is potentially affected by a contamination from the radio emission due to the star formation activity of the AGN hosting galaxies.

Integral radio counts

We used the previously computed radio LF (Equation 4.5) to derive the expected integral counts $N(>S)$ from the following equation:

$$N(>S) = \frac{1}{4\pi} \int \frac{\mathrm{d}v}{\mathrm{d}z} \mathrm{d}z \int_{Sk(z)4\pi d_l^2(z)}^{L_{max}} \Phi(L_{1.4}, z) \mathrm{d}\log L_{1.4}, \qquad (4.6)$$

where $k(z) = (1+z)^{\alpha_R - 1}$ (with $F_\nu \propto \nu^{-\alpha_R}$ and $\alpha_R = 0.5$) is the radio K-correction, $d_l(z)$ the luminosity distance, and the integral counts are measured in sr^{-1} units.

The predicted radio counts are shown in Figure 4.7. As our measured distribution of R_X represents only the FRI population (see discussion in Section 3.4), in order to reproduce the total radio counts, the contribution derived from the LF of the FRII population (as measured by Wilman et al. 2008) was added. The reproduced counts are in good agreement with the observations. At 1.4 GHz fluxes below 1 mJy the euclidean radio counts flatten, due to the appearance of the population of the star forming galaxies. In this context, it is matter of discussion which is the fraction of the AGN at these fluxes. Our results agree with recent estimates of the AGN contributions to the sub-mJy radio counts from Seymour et al. (2008) and Padovani et al. (2009). Similar results (at these fluxes) have also been obtained from semi-empirical simulations of the extragalactic radio counts by Jarvis & Rawlings (2004), Wilman et al. (2008) and Ballantyne (2009).

4.3   The kinetic luminosity function

Once the radio LF of the FRI sources is measured (Equation 4.5 and Figure 4.6), in order to derive the kinetic mechanical luminosity function (KLF) and its evolution, we should convolve the 1.4 GHz LF with a relation which converts the radio luminosity $L_{1.4}$ into a mechanical power L_K.
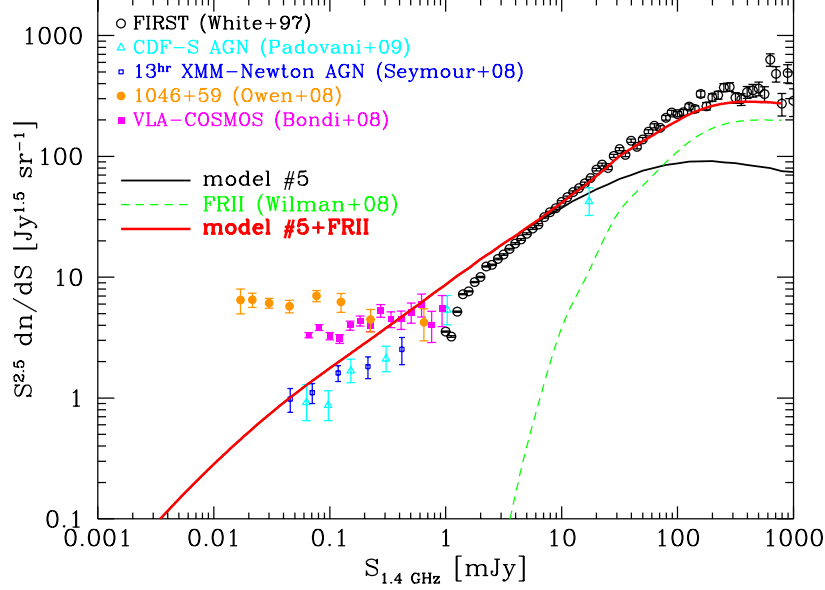
Figure 4.7: Euclidean differential 1.4 GHz radio counts. The black line shows the expected counts according to the convolution between the $P(R_X)$ distribution (fit #5) and the X-ray LF from La Franca et al. (2005); the green dashed line shows the counts produced by the FRII sources (from Wilman et al. 2008); the red line represents the sum of these two contributions. Radio counts measures from FIRST (White et al. 1997, black circles), VLA-COSMOS (Bondi et al. 2008, magenta squares) and Owen & Morrison (2008, orange squares) are also reported, as well as the AGN counts estimated by Seymour et al. (2008, blue squares) and Padovani et al. (2009, cyan triangles).

In the last decade, several authors have worked on the estimate of this relation (Willott et al. 1999; Bîrzan et al. 2004, 2008; Best et al. 2006; Heinz, Merloni & Schwab 2007; Merloni & Heinz 2008). Following the discussion of Cattaneo & Best (2009) we used two different estimates which are representative of two different luminosity regimes. At high radio luminosities (above $\sim 10^{25}$ W Hz^{-1}), Willott et al. (1999) used the minimum entropy density that the plasma radio lobes must have in order to emit the observed
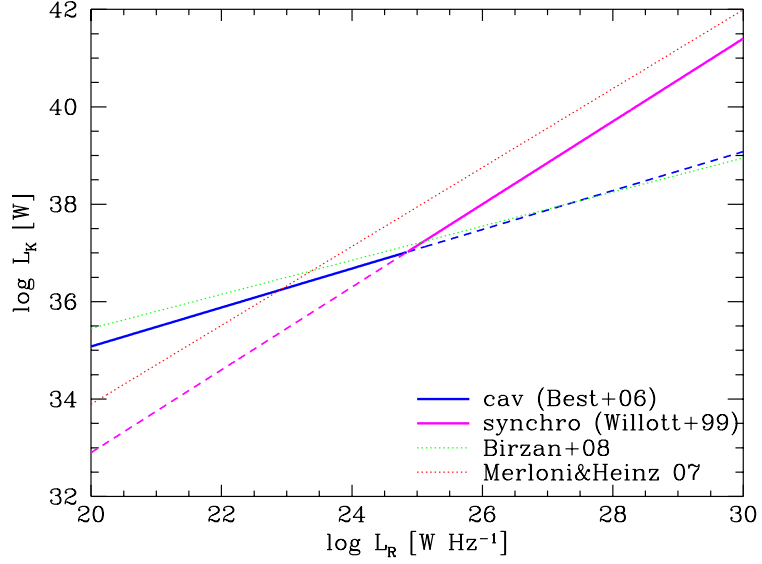
Figure 4.8: Kinetic LF as a function of the radio luminosity as estimated by Willott et al. (1999, magenta), Best et al. (2006, blue), Merloni & Heinz (2007, red) and Bîrzan et al. (2008, green). The continuous lines show the relations that have been used in our work (see Section 4.3).

synchrotron radiation and obtained (see Figure 4.8):

$$L_K = 1.4 \times 10^{37} \left(\frac{L_{1.4\,GHz}}{10^{25}\ \text{W Hz}^{-1}} \right)^{0.85} \text{W}. \tag{4.7}$$

A second approach is to infer L_K from the mechanical work that the lobes do on the surrounding hot gas. The expanding lobes of relativistic synchrotron-emitting plasma open cavities (of volume V) in the ambient thermal X-ray emitting plasma. The minimum work in inflating these cavities is done for reversible (quasi-static) inflation and equals pV, where p is the pressure of the ambient gas. Best et al. (2006) derived a relation between radio and mechanical luminosity based upon this estimate for the energy associated with these cavities, combined with an estimate of the cavity ages from the buoyancy timescale (from Bîrzan et al. 2004). Comparing the mechanical

luminosities of 19 nearby radio sources that have associated X-ray cavities with their 1.4 GHz monochromatic radio luminosities leads to a relation

$$L_K = 1.2 \times 10^{37} \left(\frac{L_{1.4 \ GHz}}{10^{25} \ \text{W Hz}^{-1}} \right)^{0.40} \text{W},$$ (4.8)

which is better suited for low luminosities (below $L_{1.4} \sim 10^{25}$ W Hz^{-1}) and is close to the estimate by Bîrzan et al. (2008, see Figure 4.8). Using a similar method, Merloni & Heinz (2008) obtained at high radio luminosities, a relation similar to the one by Willott et al. (1999) but with about $0.5 - 1$ dex higher kinetic luminosities (see Figure 4.8).

In this work (as in Cattaneo & Best 2009) we used Equation 4.7 at high luminosities (above $L_{1.4} \sim 10^{25}$ W Hz^{-1}) and Equation 4.8 at lower luminosities. Using these relations, once derived the radio LF from the X-ray LF and the R_X distribution according to Equation 4.5, we can estimate the kinetic LF, $\Phi_K(L_K, z)$, by the formula

$$\Phi_K(L_K, z) = \frac{\text{d}N(L_K, z)}{\text{d}V \text{d} \log L_K} = \Phi_{1.4}(L_{1.4}(L_K), z) \frac{\text{d} \log L_{1.4}}{\text{d} \log L_K},$$ (4.9)

while the bolometric radiative LF, $\Phi_{\text{rad}}(L_{\text{bol}}, z)$, is derived from the X-ray LF, via the bolometric correction $L_{\text{bol}} = K_X(L_X)L_X$, by

$$\Phi_{\text{rad}}(L_{\text{bol}}, z) = \frac{\text{d}N(L_{\text{bol}}, z)}{\text{d}V \text{d} \log L_{\text{bol}}} = \Phi_X(L_X(L_{\text{bol}}), z) \frac{\text{d} \log L_X}{\text{d} \log L_{\text{bol}}},$$ (4.10)

where for $K_X(L_X)$ we used the relation from Marconi et al. (2004). Both the, so derived, kinetic and radiative (bolometric) LF are shown in Figure 4.9, while in Figure 4.10 the kinetic power density, $L_K \Phi_K(L_K, z)$, as function of the kinetic luminosity is shown.

By integrating in luminosity the above derived kinetic and radiative (bolometric) LF it is possible to estimate the dependence of the AGN mechanical and radiative power per unit cosmic volume as a function of redshift,

$$\Omega_K(z) = \int L_K(L_{1.4})\Phi_{1.4}(L_{1.4}, z)\text{d} \log L_{1.4},$$ (4.11)
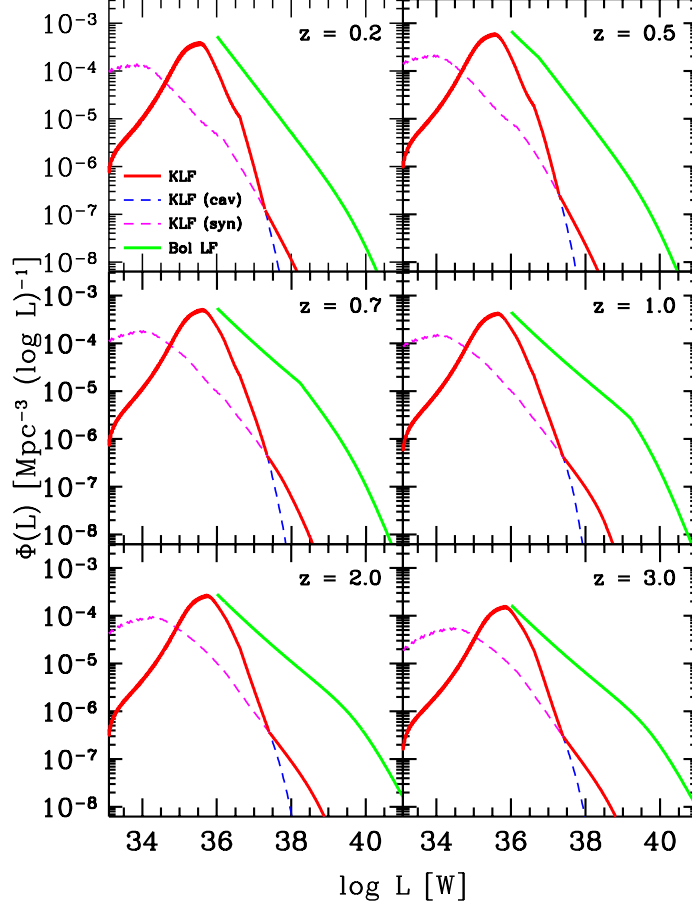
Figure 4.9: Bolometric radiative (green) and kinetic AGN LF. Blue and magenta dashed lines show the kinetic LF predicted using the $L_R - L_K$ relations from Willott et al. (1999) and Best et al. (2006) respectively. The red line is the result obtained using the combination of the two relations at high and low luminosities as described in Section 4.3.

and

$$\Omega_{\mathrm{rad}}(z) = \int L_{\mathrm{bol}}(L_X)\Phi_X(L_x, z)\mathrm{d}\log L_X, \tag{4.12}$$

which are shown in Figure 4.11. As both the above equations depend on the X-ray luminosity function (see Equation 4.5) the integral lower limit was
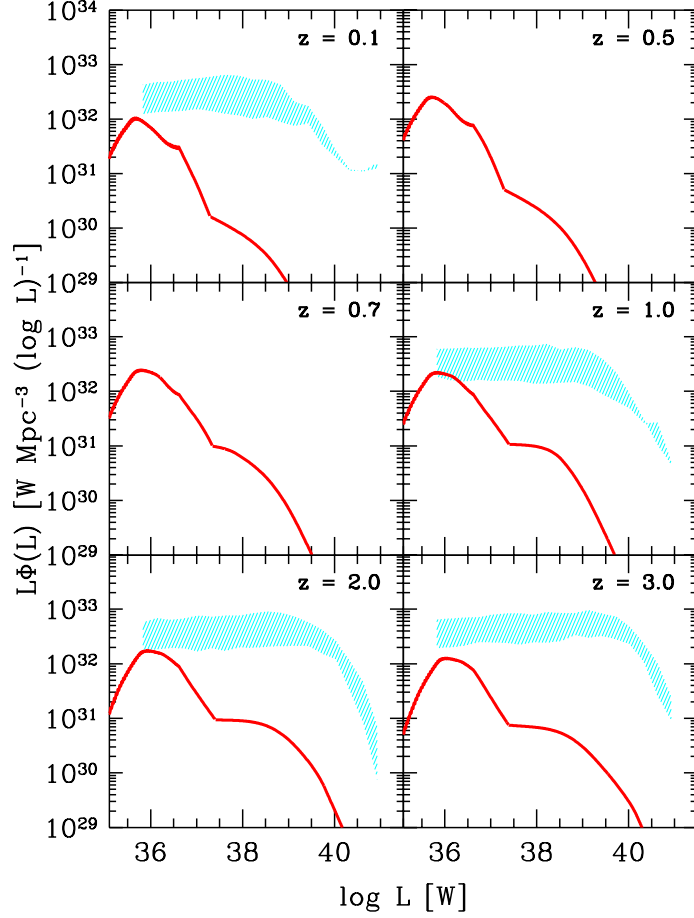
Figure 4.10: Kinetic power density as a function of the kinetic luminosity according to fit #5 (red line). The results by Merloni & Heinz (2008) are shown by a cyan shaded area.

$\log L_X = 41$ erg s^{-1} which corresponds to a lower limit of $\log L_{\mathrm{bol}} \simeq 35.5$ W for Equation 4.12 and, according to the R_X distribution and the relation between $L_{1.4}$ and L_K (Equation 4.8) to a lower limit of $\log L_K \simeq 34.5$ W for Equation 4.11.

The resulting kinetic power density would not change if, at all luminosities, the conversion of the radio into kinetic luminosity by Best et al. (2006,
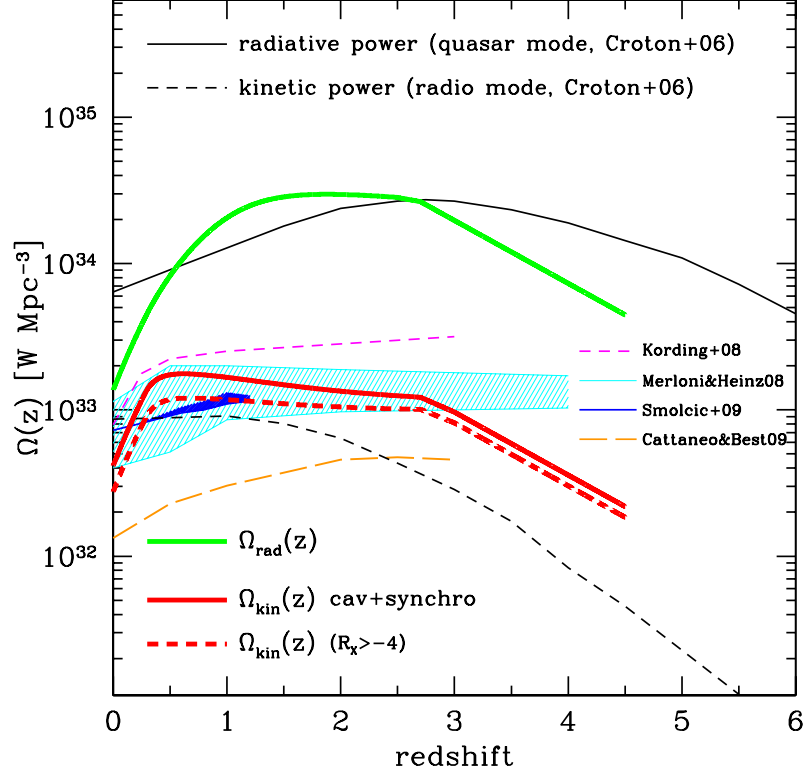
Figure 4.11: Radiative (green) and kinetic (red) power density as a function of redshift. The red dashed line represents the result if only the $R_X > -4$ (i.e. the more radio-loud) objects are used. Kinetic luminosity density estimations from Körding, Jester & Fender (2008, magenta), Cattaneo & Best (2009, orange), Merloni & Heinz (2008, cyan shaded area) and Smolčić et al. (2009, blue shaded area) are reported, as well as kinetic and radiative (i.e. radio and quasar modes) power densities used in the model of Croton et al. (2006, black dashed and continuous lines respectively).

Equation 4.8) only would be used, while a factor $4 - 6$ lower values would be obtained using the relation from Willott et al. (1999, Equation 4.7), only. As shown in Figure 4.9 this difference is caused by the steep drop off of the 1.4 GHz radio LF at luminosities higher than $\log L_R \sim 25$ W (see Figure
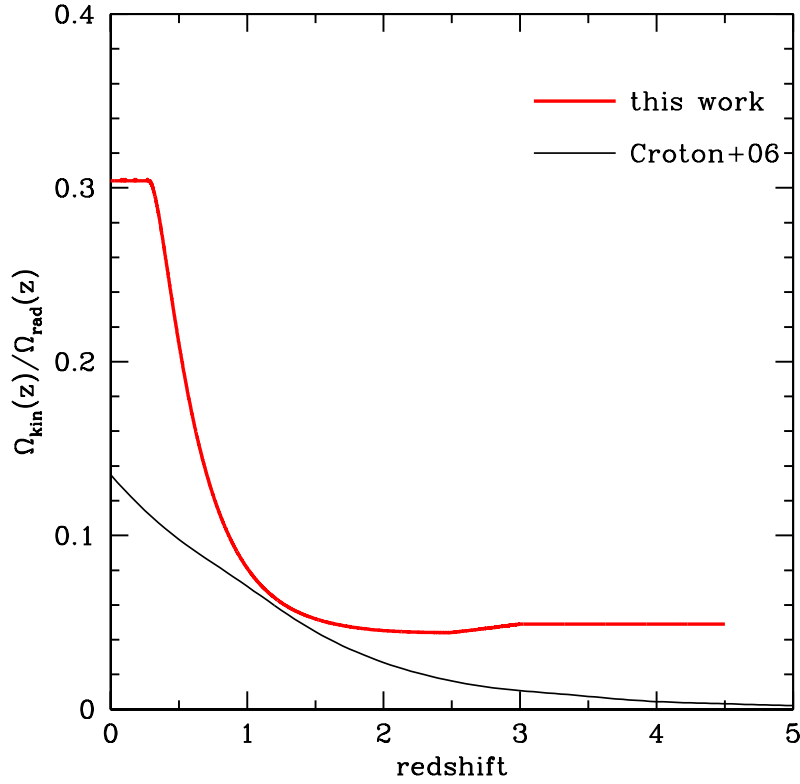
Figure 4.12: Kinetic to radiative power density ratio as a function of redshift (fit #5; red line). Results from Croton et al. (2006) are shown by a black line.

4.6); as a consequence the resulting power density (the integrated kinetic LF) depends mainly on which conversion of the radio luminosity into kinetic power is used at low luminosities.

4.4   Discussion and conclusions

The probability distribution function of R_X, $P(R_X|L_X, z)$ estimated in Section 4.2 depends on both luminosity and redshift: the average R_X increases

with decreasing luminosity and (possibly) increasing redshift (see best fit #5 in Table 4.1 and Figure 4.4). The observed increase of the average R_X value with decreasing luminosity is similar to previous results and models where (in analogy with X-ray binaries) low luminosity AGN are expected to be more likely radio loud (see e.g. Merloni & Heinz 2008; Körding, Jester & Fender 2008). These trends, however, do not include the most luminous (radio loud; mostly FRII) sources. As far as the more radio loud population is concerned, it has been observed that the fraction of more radio loud AGN increases with increasing optical (or X-ray) luminosity and decreasing redshift (Miller, Peacock & Mead 1990; Visnovsky et al. 1992; Padovani 1993; La Franca et al. 1994; Goldschmidt et al. 1999; Ivezić et al. 2002; Cirasuolo et al. 2003; Jiang et al. 2007).

The knowledge of the R_X distribution, once convolved with the X-ray LF and the relations between the kinetic and radio luminosity, allows to estimate the kinetic LF and its evolution. At luminosities higher than the break of the bolometric LF ($L_K \sim 10^{39}$ W) the kinetic LF results to be more than two orders of magnitude smaller than the bolometric LF (see Figure 4.9), while at lower luminosities the relevance of the kinetic LF increases, reaching values comparable to the bolometric one at $L_K \sim 10^{36}$ W, which roughly corresponds to the minimum luminosity experimentally probed by the X-ray LF ($\log L_X \sim 42$ erg s^{-1}; see e.g. La Franca et al. 2005). The kinetic LF shows a maximum in the range $L_X = 10^{35} - 10^{37}$ W, where most ($\sim 90\%$) of the kinetic power density (shown in Figure 4.10) is produced.

In Figure 4.11 we show the kinetic and radiative power density as a function of the redshift. We also show the kinetic power density corresponding to the more radio emitting AGN having R_X larger than -4, and then corresponding to the population which is typically represented by the radio LF (see in Figure 4.6 the comparison of the reproduced radio LF with $R_X > -4$ with the radio LF of FRI sources as measured by Smolčić et al. 2009). It is then possible to

see that the kinetic power density could be underestimated by up to a factor of about two, if the radio LF alone is used, without taking into account the low radio luminosity AGN population.

Our estimates are in qualitative agreement with the trends of the radiative and kinetic power density with redshift used by Croton et al. (2006) at $z > 0.5$ (see Figure 4.11). However, at lower redshifts we find a sharp (a factor of five) decrease of both radiative and kinetic power densities from $z \sim 0.5$ (i.e. about 5 billion years ago) to $z = 0$. This result is quite robust, and comes from the strong negative evolution of the AGN LF from $z \sim 2$ down to $z = 0$, which has been observed since the first studies of the QSO evolution in the optical (see e.g. Marshall et al. 1983; Croom et al. 2009, for recent results), and measured by many other authors in the hard X-rays (e.g. Ueda et al. 2003; La Franca et al. 2005; Hasinger 2008). Conversely, Croton et al. (2006) assume an almost continuous increase of both the kinetic and radiative powers, due to the assumption that both phenomena are related to an almost constant accretion onto the SMBH. Under this assumption Croton et al. (2006) overestimate both the AGN radiative and kinetic power densities at low ($z \lesssim 0.5$) redshift, allowing only for a much shallower decrease of the kinetic feedback (a factor of 30%) and of the AGN radiative power.

In Figure 4.12 we show the $\Omega_K/\Omega_{\mathrm{rad}}$ ratio as function of redshift. According to our best fit #5, at $z > 0.5$ the kinetic power density is $\sim 5\%$ of the radiative density, and increases up to about 30% at decreasing redshifts. This increase at low redshifts of the ratio of the kinetic power to the radiative power density could help in modeling the quenching of the star formation at low redshift. In Croton et al. (2006) a milder increase is assumed, which should be attributed to the (above discussed) overestimate of the low redshift AGN radiative density.

Many previous results on the AGN kinetic LF are based on the convolution of some relations between the kinetic and radio power with direct measures of

the AGN radio LF (e.g. Shankar et al. 2008; Merloni & Heinz 2008; Körding, Jester & Fender 2008; Cattaneo & Best 2009; Smolčić et al. 2009). As already discussed in the introduction, the measure of the R_X distribution is useful in order to allow a detailed implementation of the AGN feedback within the galaxy formation and evolution models because it gives the opportunity to predict the radio luminosity (and thus feedback) of each AGN as a function of its luminosity (accretion rate) and redshift.

According to our best fit #5, in the redshift range $z = 0.5 - 3$ the integrated kinetic power density is $\sim 1 - 2 \times 10^{33}$ W Mpc^{-3} (see Figure 4.11). This is in rough agreement with the previous estimates by Merloni & Heinz (2008), Körding, Jester & Fender (2008) and Smolčić et al. (2009). At lower redshift ($z <$0.5) we observe a drop by a factor of five, similar to what observed by Körding, Jester & Fender (2008), and in agreement, within the uncertainties, with Merloni & Heinz (2008). On the contrary our results are, at any redshift, $2 - 8$ times greater than that reported by Cattaneo & Best (2009). Merloni & Heinz (2008) found that their kinetic LF roughly corresponds to a constant overall efficiency in converting the accreted mass energy into kinetic power $\epsilon_{\mathrm{kin}} \simeq 3 - 5 \times 10^{-3}$ (where $L_K = \epsilon_{\mathrm{kin}} \dot{m} c^2$). Their results are similar to ours where, according to Equations 4.11 and 4.12, on average, we have $\epsilon_{\mathrm{kin}} \simeq (\Omega_K/\Omega_{\mathrm{rad}})\epsilon_R \simeq 5 \times 10^{-3}$, as we measure $\Omega_K/\Omega_{\mathrm{rad}} \simeq 0.05$ (see the $\Omega_K/\Omega_{\mathrm{rad}}$ ratio as a function of redshift in Figure 4.12), and assuming a radiative efficiency $\epsilon_R = 0.1$ (Marconi et al. 2004). However, we observe an increase of the $\Omega_K/\Omega_{\mathrm{rad}}$ ratio (i.e. of the kinetic efficiency) up to a value 0.3 at decreasing redshifts, which Merloni & Heinz (2008) observe in the most massive objects only ($> 10^8 - 10^9 \ M_\odot$; see e.g. their Figure 13). It should also be noted that, although the integrated kinetic power density of Merloni & Heinz (2008) is in agreement with our estimate, their kinetic LF is similar to our measure only at $L_K \sim 10^{36}$ W (see Figure 4.10), while it is definitely larger (by about an order of magnitude) at higher kinetic luminosities. Once integrated in
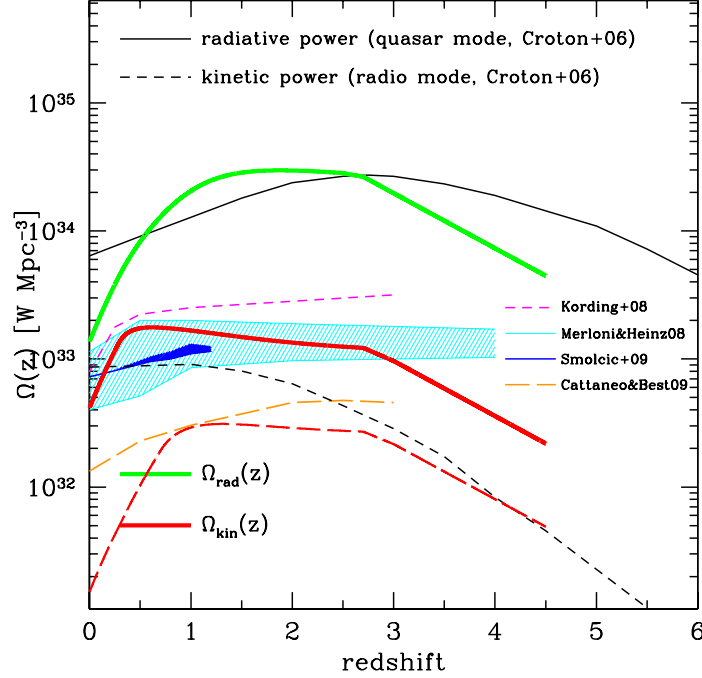
Figure 4.13: Same as Figure 4.11. The dashed red line shows the resulting kinetic power density when using the same low luminosity integration limit as in Merloni & Heinz (2008). See Section 4.4 for details.

luminosity, the computed power densities are similar (at $z \lesssim 3$) because our low luminosity limit ($L_K = 10^{34}$ W) is significantly lower than that used by Merloni & Heinz (2008, $L_K = 10^{36}$ W). If we use the same low luminosity limit used in Merloni & Heinz (2008), the resulting kinetic power density would be up to a factor of 10 lower with respect to Merloni & Heinz (2008), as shown in Figure 4.13. The origin of this difference is clear from Figure 4.10, where our results and the kinetic luminosity function from Merloni & Heinz (2008) above $L_K = 10^{36}$ W are very different. The contribution from radio quiet sources is therefore required in our estimate to correctly reproduce the galaxy formation models expectations; in Merloni & Heinz

(2008) this contribution is not needed, and could instead lead to an estimate of the kinetic power density well above the model requirements.

Shankar et al. (2008) found that the ratio of the kinetic to bolometric luminosity, defined as $g_k = L_K/L_{\mathrm{bol}}$, is constant and equal to $g_k = 0.10$ with a scatter of $\sigma = 0.38$. According to Equations 4.11 and 4.12, g_k corresponds roughly to the ratio $\Omega_K/\Omega_{\mathrm{rad}}$ (plotted as function of redshift in Figure 4.12), which, as discussed above, levels at ~ 0.05 at $z > 1$ while increases up to 0.3 at $z = 0$.

Chapter 5

The obscured Black Holes growth phase

5.1 Introduction

In the last years, the X-ray universe has been probed down to extremely deep fluxes, thanks to the ESA *XMM-Newton* and NASA *Chandra* missions. The latest data catalog from the Chandra Deep Field South (CDFS) has reached a flux limit of about $F(2-8 \text{ keV}) \simeq 5 \times 10^{-17}$ erg s^{-1} cm^{-2}, revealing a sky density above $10\,000$ AGN per square degree. Optical surveys, however, are limited to shallower magnitude levels (e.g. $B = 22$, Wolf et al. 2003) and reveal only a density of hundreds of AGN/deg^2. Therefore, X-ray surveys are the most powerful tools available to detect AGN.

However, even the most deep X-ray surveys may not be able to detect the whole AGN population. The most heavily obscured sources suffer from attenuation in their spectrum, due to Compton scattering, at energies below 10 keV; only a small number of these Compton-thick AGN have been detected. Nevertheless, the number density of these sources is expected to be much higher (as stated in Section 2.6): the SMBH mass function obtained by

integrating the X-ray luminosity function is a factor of $\sim 1.5 - 2$ smaller (depending on the assumed efficiency in the conversion of gravitational energy to radiation) than the same mass function derived using the $M_{BH} - \sigma_V$ scaling relations and the local bulge's luminosity function (Marconi et al. 2004; Merloni & Heinz 2008). Moreover, AGN synthesis models for the cosmic X-ray background require a significative number of Compton-thick sources, at moderate redshifts, to account for the peak at $20 - 30$ keV (Gilli, Comastri & Hasinger 2007).

In the last few years, the mid infrared part of the spectrum has gathered much attention for providing an alternative and promising way to detect highly obscured AGN. The radiation coming from the inner region is absorbed by the circumnuclear dust and re-emitted at infrared wavelengths, thus making highly obscured AGN bright infrared emitters. In this kind of sources, the $2 - 10$ keV X-ray emission may be diminished by up to two orders of magnitude, while the mid infrared emission remains unattenuated: in this range of wavelengths, the dust extinction is less strong than in nearby parts of the spectrum (like the near infrared and the optical/UV part). All these features explain why surveys in the mid infrared band have more capabilities to reveal obscured AGN. We will briefly review the most recent developments in the search of Compton-thick AGN in the following Section.

5.2 Recent results

Several authors have pointed out that the sources with strong mid infrared ($24\,\mu$m) fluxes but faint optical and near infrared emission are probably hosting heavily obscured Compton-thick nuclei. Martinez-Sansigre et al. (2005) first detected a population of distant objects via this selection and argued that these are mostly highly obscured type 2 QSO (as confirmed by spectroscopic observations) and their number is at least comparable in size to

the unobscured AGN. Houck et al. (2005) selected a population of distant galaxies with extreme mid infrared-to-optical ratios ($F_{24}/F_R > 1000$) around $z \sim 2$; these kind of sources are called Dust Obscured Galaxies (DOGs; Dey et al. 2008).

DOGs are young, massive, star-forming galaxies. It has been shown that this kind of sources have higher stellar mass and star formation rates with respect to the normal galaxies: the majority of DOGs have stellar masses above 10^{11} $M_\odot$ and SFR > 40 $M_\odot$/yr (some extreme objects may form hundreds or even thousands of solar masses per year).

Stacking analysis is a powerful tool to study X-ray emission of DOGs. In deep X-ray surveys it is possible to detect these sources by stacking together the X-ray images at the infrared position of the sources. Using this technique, it has been suggested (Daddi et al. 2007; Fiore et al. 2008; Georgantopoulos et al. 2008; Fiore et al. 2009) that the majority of DOGs have redshifts in the range $z = 1 - 3$ and host a Compton-thick AGN.

Fiore et al. (2009)

Fiore et al. (2009) selected a sample of DOGs in the COSMOS field and analyzed its X-ray properties. About $\sim 25 - 30\%$ of the sample is detected in the X-rays, and a fraction of 75% of these sources have luminosities compatible with AGN emission. The remaining part of the sample is not detected in the X-ray band; the authors computed the stacked count for these sources and used the estimated hardness ratios to constrain the fraction of Compton-thick sources in the candidate sample, making also use of detailed Monte Carlo simulations; these simulations were performed assuming that the sources without X-ray detection are either highly obscured AGN or star forming galaxies, and probing which combination better reproduces the observed values of hardness ratio. They demonstrated that the samples of sources with highest F_{24}/F_R ratios, as well as extreme $R - K$ colors
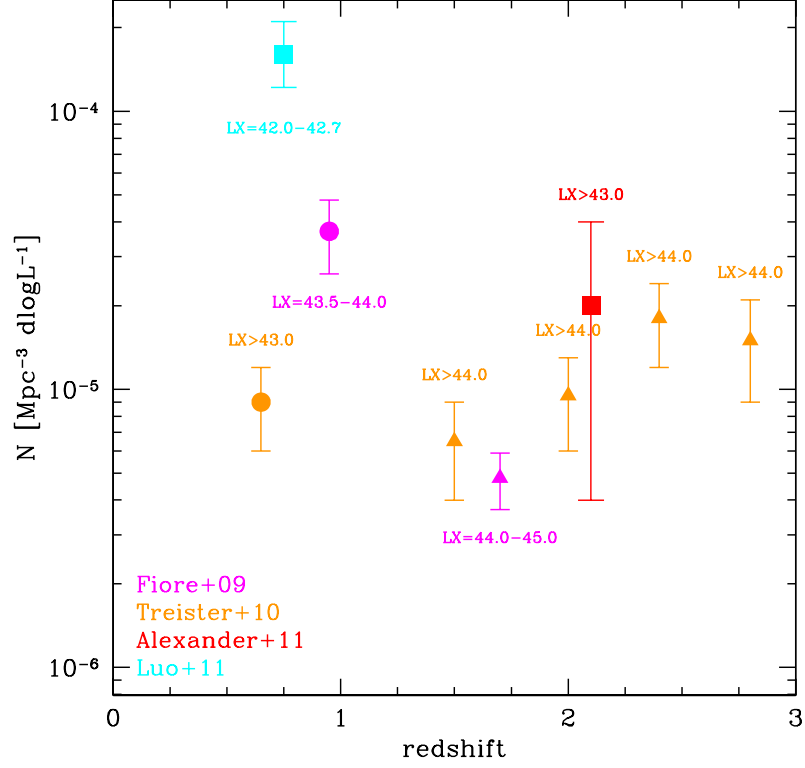
Figure 5.1: Space density of Compton-thick AGN as a function of redshift, as reported by Fiore et al. (2009, magenta), Treister et al. (2010, orange), Alexander et al. (2011, red) and Luo et al. (2011, cyan). The intrinsic $2 - 10$ keV luminosity range of each sample is reported near the data.

$(R - K > 4.5)$, are almost made up of Compton-thick AGN. The authors also gave an estimation of the volume density of Compton-thick AGN in two redshift-luminosity bin, founding $\Phi_{CT} = (4.8 \pm 1.1) \times 10^{-6}$ Mpc^{-3} for $z = 1.2 - 2.2$ and $\log L_X = 44 - 45$ erg s^{-1}, and $\Phi_{CT} = (3.7 \pm 1.1) \times 10^{-5}$ Mpc^{-3} for $z = 0.7 - 1.2$ and $\log L_X = 43.477 - 44$ erg s^{-1} (see Figure 5.1); these results mean that the highly obscured AGN densities in these two bins are $\sim 44\%$ and $\sim 67\%$ respectively of the densities of unobscured and moder-

ately obscured AGN as expected from the La Franca et al. (2005) luminosity function.

Treister et al. (2010)

Using the same selection criteria from Fiore et al. (2009), Treister et al. (2010) selected a sample of infrared excess sources in the Extended *Chandra* Deep Field-South. While a small fraction ($\sim$ 9%) of these sources are X-ray detected and still compatible with moderate values of absorption ($N_H = 10^{22} - 10^{23}$ cm^{-2}), the majority of the sample is again undetected in the X-rays. Using a stacking analysis of the undetected sample, the authors found significant detection in both soft and hard bands, and the average X-ray spectral properties can be interpreted by assuming that $\sim$ 90% of the population is made up of Compton-thick sources. They also studied the space density of sources implied by this sample, and, while at low redshifts and luminosities their results are in good agreement with existing models or extrapolations of X-ray luminosity functions to higher obscurations, from $z = 1.5$ to 2.5 they observed a strong positive evolution in the number of sources with $L_X > 10^{44}$ erg s^{-1}, as shown in Figure 5.1.

Georgantopoulos et al. (2011)

Georgantopoulos et al. (2011) performed a spectral analysis of a sample of 22 X-ray detected DOGs from the Chandra Deep Fields, and address the Compton-thick content of this sample mainly using the information obtained from X-ray spectroscopy. They found that 7 out of 22 DOGs are associated with relatively unobscured sources, having a power-law spectrum with $\Gamma > 1.4$ (the value of $\Gamma = 1.4$ corresponds to the stacked spectrum of all sources in the CDFS; see Tozzi et al. 2001). A number of intrinsically flat-spectrum ($\Gamma < 1$) sources have also been found: when limiting the analysis to the

subsample with good photon statistic, they found that 4 out of 12 (30%) sources have a flat spectrum. Georgantopoulos et al. (2011) conclude that this fraction could be as high as 50% if all sources are taken into account, lower than reported in the previously reported studies of stacking analysis of X-ray undetected DOGs.

Alexander et al. (2011)

Alexander et al. (2011) put a constraint on the obscured AGN density in the $z \sim 2$ *BzK* galaxy population, using the new CDFS 4 Ms observations. The authors approach consisted in characterizing the X-ray spectral and variability properties of the X-ray detected part of the sample, and performing a stacking analysis of the X-ray undetected sources. The most obscured (i.e., with a flat spectral slope) AGN resulted to be better characterized by a pure reflection model than an absorbed power-law, suggesting an extreme Compton-thick absorption, and moreover their composite spectrum show a prominent emission line at ~ 6.4 keV; however, the authors do not clearly reveal further AGN sources in the undetected part of the sample, suggesting that their contribution is not dominant. This led to an estimation of a space density of $\Phi_{CT} \simeq f \times 4 \times 10^{-5}$ Mpc^{-3} for Compton-thick sources with $2 - 10$ keV luminosity $L_X \gtrsim 10^{43}$ erg s^{-1} in the redshift range $z \sim 1.4 - 2.6$, where f lies between 0.1 and 0.5 (Figure 5.1).

Luo et al. (2011)

In their work, Luo et al. (2011) analyzed 242 sources identified via the ISX selection method (Daddi et al. 2007) in the CDFS at redshift $z = 0.5 - 1$; an X-ray stacking analysis of 23 of the objects in the central region resulted in a very hard X-ray signal with an effective photon index of $\Gamma = 0.6^{+0.3}_{-0.4}$, indicating a significant contribution from obscured AGN. Using

Monte Carlo simulations, the authors inferred that in the ISX sample the fraction of obscured AGN is as high as $74\% \pm 25\%$, within which $\simeq 80\%$ are Compton-thick AGN; these sources have moderate intrinsic X-ray luminosities ($\sim 1 - 5 \times 10^{42}$ erg s^{-1}). Luo et al. (2011) estimated that the space density of Compton-thick AGN in these redshift and X-ray luminosity ranges is $(1.6 \pm 0.5) \times 10^{-4}$ Mpc^{-3} (Figure 5.1).

This work

In this work we have used the 24 μm selected sample described in Section 3.2, which consist in 16 409 sources with a redshift measurement available, either spectroscopic or photometric, and accurate 5.8 μm luminosity estimation. All these sources are shown in Figure 5.2 on the redshift-5.8 μm luminosity plane.

We divided our data-set in 12 $L_{5.8} - z$ bins as shown in Figure 5.2; the redshift and luminosity ranges of each bin were chosen to avoid any potential incompleteness due to the flux limits of the two sources. These ranges, the survey used (either COSMOS or GOODS) and the 24 μm sources included in each bin, are reported in Table 5.1.

5.3   X-ray detected CT AGN

In some cases the *Chandra* observations may be deep enough to directly detect Compton-thick AGN. Therefore, before looking for hidden obscured AGN within our sample of 24 μm sources, we first searched in the literature for published lists of Compton-thick AGN in COSMOS and GOODS that are suitable to be included in our sample.

5.3.1 CT AGN in COSMOS

In the C-COSMOS catalog we did not found any Compton-thick AGN among those sources with enough X-ray counts (70) to carry out detailed spectral fit analyses (see Lanzuisi et al. in preparation).

We then verified if Compton-thick AGN exist among detected sources with less X-ray counts (for which a detailed spectral fit analysis was not possible). Therefore, we selected all those sources in the C-COSMOS catalog with less than 70 counts in the $0.5 - 7$ keV band and estimated the N_H value from the hardness ratio. According to this analysis we found 55 objects with $\log N_H > 23.8$, which were further studied in more detail. The sources have been divided in four redshift bins having the same ranges reported in Table 5.1 (due to the small numbers, we were not able to further divide these strips in luminosity bins). In each redshift bin, the average $0.5 - 7.0$ keV spectrum was extracted and fitted with two different models: a power-law with a single

Table 5.1: Sources in the $L_{5.8} - z$ grid (see Figure 5.2.

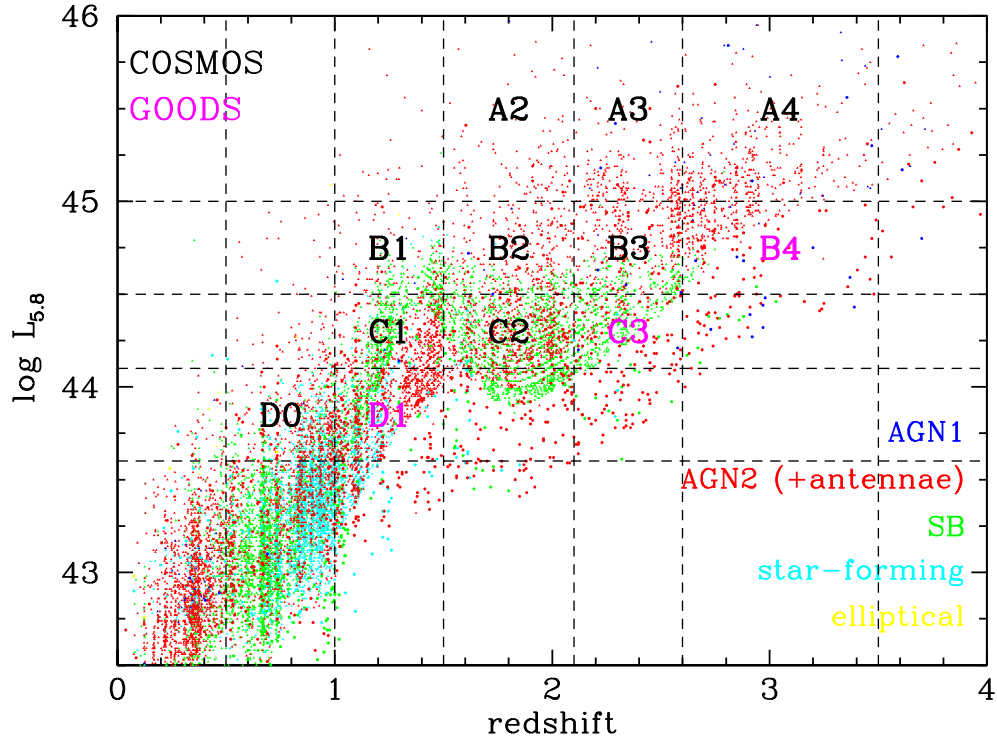| bin	z	$\log L_{5.8~\mu m}$ erg s^{-1}	number of sources	survey used
A2	1.5-2.1	45.0-46.0	94	COSMOS
A3	2.1-2.6	45.0-46.0	202	COSMOS
A4	2.6-3.5	45.0-46.0	339	COSMOS
B1	1.0-1.5	44.5-45.0	255	COSMOS
B2	1.5-2.1	44.5-45.0	383	COSMOS
B3	2.1-2.6	44.5-45.0	426	COSMOS
B4	2.6-3.5	44.5-45.0	44	GOODS
C1	1.0-1.5	44.1-44.5	865	COSMOS
C2	1.5-2.1	44.1-44.5	1311	COSMOS
C3	2.1-2.6	44.1-44.5	80	GOODS
D0	0.5-1.0	43.6-44.1	709	COSMOS
D1	1.0-1.5	43.6-44.1	118	GOODS

Figure 5.2: 5.8 μm luminosity-redshift distribution for sources in the mid infrared sample.

absorption component and two power-laws with two absorption components, with one fixed to $N_H = 3 \times 10^{24}$ cm^{-2}; the second model gave the best results, suggesting that Compton-thin and Compton-thick AGN are both present in these samples, in an almost equal fraction. On average, these results predict that the contribution of these sources to the CT population is less than a few sources in each of the $L_{5.8} - z$ bins used in our analysis (see Table 5.1).

5.3.2 CT AGN in GOODS

In the GOODS field, Brightman & Ueda (2012) performed a spectral analysis of the sources contained in the CDFS 2 Ms catalog from Luo et al. (2008),

using the full CDFS 4 Ms data set already available, and found a total of 41 Compton-thick AGN (with $10^{24} < N_H < 10^{26}$ cm^{-2}). The authors presented a list of 20 secure (confidence limit $> 90\%$) Compton-thick sources, with the details of the spectral fit parameters. Two Compton-thick sources from Brightman & Ueda (2012) are included in our $L_{5.8} - z$ grid, and then have been taken into account in the following analysis.

Recently, Iwasawa et al. (2012) presented a list of 7 obscured AGN selected using their X-ray excess in the $9 - 20$ keV band, relative to lower energy emission, including two possible Compton-thick sources. However, these two Compton-thick candidates (PID 114 and PID 252) lie outside the $L_{5.8} - z$ grid defined in section 3.2.3, and so we did not include them in the following analysis.

The breakdown of the number of X-ray detected Compton-thick sources in each $L_{5.8} - z$ bin is reported in Table 5.2 (column 2).

5.4 Sources without X-ray detection

Several selection criteria have been proposed to efficiently select Compton-thick AGN on the basis of their optical and mid infrared properties, as discussed in Section 5.1. It has been shown that most of the sources with high mid infrared to optical color ratio (MIR/O> 1000) are highly obscured AGN. However, Compton-thick sources are also found at lower MIR/O values, although in a smaller fraction (see Fiore et al. 2009).

In this work, we adopted a different approach, based on the study of the X-ray count rates of 24 μm sources; this study can give useful information on whether an highly obscured AGN is hosted by an infrared source or not. We expect unobscured or moderately obscured AGN to be located in the high end of the X-ray count rate distribution, while sources not powered by accretion, like passive galaxies, should lie at the lower end of the same distribution.
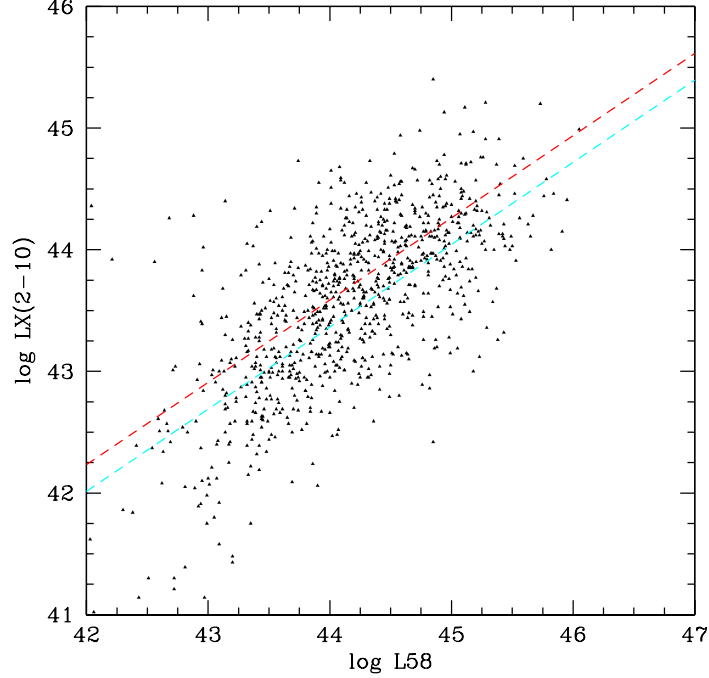
Figure 5.3: 2-10 kev luminosity as a function of 5.8 μm infrared luminosity for detected AGN sources in C-COSMOS catalog. The red and cyan dashed lines indicate respectively the best-fit relations for $N_H > 10^{23}$ and $N_H < 10^{23}$ cm^{-2} AGN populations (see Section 5.4.1).

We expect to find Compton-thick AGN in an intermediate region of this distribution. Therefore we studied the X-ray count rate distribution for all 24 μm sources included in our data-set (COSMOS and GOODS) and included in the $L_{5.8} - z$ bins defined in Table 5.1.

5.4.1 Simulations to assess count-rate distributions

To define quantitatively the X-ray count rates ranges in which Compton-thick are expected to be found, we developed a simulation code that generates the
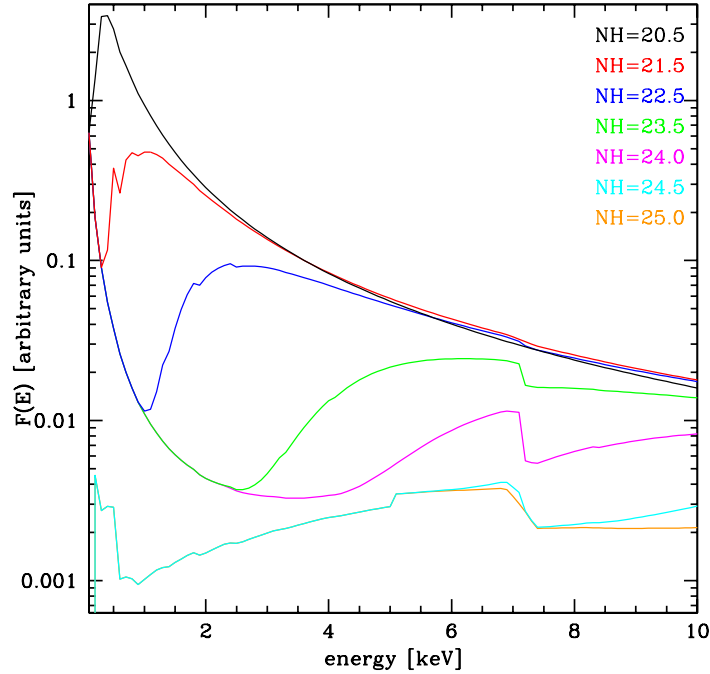
Figure 5.4: X-ray spectrum assumed in our simulations for seven different N_H absorption values (see section 5.4.1).

expected X-ray count rate distributions of AGN in three different classes of absorption, starting from the expected intrinsic X-ray luminosity for each source and assuming an N_H distribution.

N_H distribution

We first computed the expected number of AGN per unit volume in 30 N_H bins (between $20 < \log N_H < 25$) and in a dense $L_X - z$ grid using the X-ray luminosity function from La Franca et al. (2005); the results have been rebinned in three different bins of N_H: unabsorbed ($10^{20} < N_H < 10^{22}$ cm^{-2}), Compton-thin ($10^{22} < N_H < 10^{24}$ cm^{-2}) and Compton-thick ($10^{24} < N_H <$

10^{25} cm^{-2}). Following the prescriptions of La Franca et al. (2005) we adopted a flat distribution for N_H values larger than 10^{21} cm^{-2}, where the fraction of absorbed AGN increases with decreasing luminosity and increasing redshift.

5.8 μm-X-ray luminosity correlation

One of the most important ingredients of our simulation is the prediction of the intrinsic X-ray luminosity that an AGN could have according to its $L_{5.8}$ luminosity. The $L_X - L_{5.8}$ correlation has been measured (although with a large scatter) for all COSMOS 24 μm sources with an X-ray counterpart: we estimated the N_H values of all sources on the basis of their hardness ratio and evaluated the $L_X - L_{5.8}$ correlation in two different absorption bins. We found:

$$\log L(2 - 10 \text{ keV}) = 0.676 \log L_{5.8} + 13.622 \qquad (5.1)$$

for $N_H \leq 10^{23}$ cm^{-2}, and

$$\log L(2 - 10 \text{ keV}) = 0.676 \log L_{5.8} + 13.842 \qquad (5.2)$$

for $N_H > 10^{23}$ cm^{-2}, with a scatter of 0.5 dex in both cases (see Figure 5.3). The above Equations 5.1 and 5.2, along with their scatter, were used to infer the densities of AGN in the $L_X - z$ space (as predicted by La Franca et al. 2005) into the $L_{5.8} - z$ space.

X-ray spectrum

We assumed a power-law spectrum with an energy index $\alpha_{\text{AGN}} = 0.8$, plus a Compton-reflection component with the same normalization of the power-law, assuming an inclination of the reflecting material to the line of sight of 60 degrees, and a scattering component with the same spectral index of the power-law component and normalization 1/100 of the power-law component. For $N_H > 3 \times 10^{24}$ cm^{-2}, we assumed that direct emission is completely

blocked by photoelectic absorption and Compton scattering. As an example, Figure 5.4 shows the X-ray spectra corresponding to seven N_H values.

Simulation results

In each $L_{5.8} - z$ bin we computed the expected X-ray count rates in the $0.5 - 7.0$ keV band, based on the X-ray luminosities and the 30 N_H values we used to compute the expected densities of AGN. The $0.5 - 7.0$ keV count rates were computed from $2 - 10$ keV luminosities using the above described spectra and the *Chandra* on axis response.

In Figure 5.5 the expected AGN count rate distribution, computed with the above described method in the B2 bin (see Table 5.1), is compared with the observed background subtracted count rate distribution of the 24 μm sources. It should be noted that the observed distribution is bimodal: a main peak, located in the range between 10^{-5} and 10^{-4} counts/s, and a secondary maximum, at higher count rate values, are visible. As expected, according to the simulations of the count rate distributions, the secondary maximum at high count rate values is fairly well reproduced by the population of unabsorbed AGN (orange dashed line in Figure 5.5), while Compton thin AGN are expected at slightly lower count rates (red dashed line in Figure 5.5).

According to our simulations the Compton-thick AGN are expected to have count rates lower than the Compton-thin population. The green vertical line in Figure 5.5 represents the lower limit of the expected Compton-thick AGN distribution: in our simulations, no Compton-thick AGN generate X-ray count rates with values lower than the green line. This suggests that Compton-thick AGN are rare at lower count rates where instead starburst galaxies are expected.

In Figure 5.5 the magenta line shows the X-ray count rate distribution of the observed 24 μm sources having more than 10 background-subtracted X-ray counts (within $5''$ from the infrared position). As shown before, almost
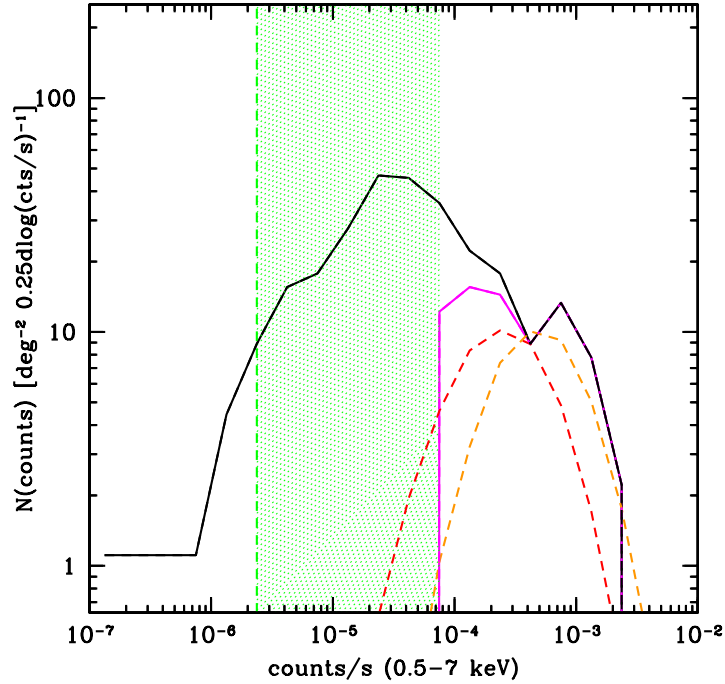
Figure 5.5: X-ray count rate distribution for 24 μm selected sources in the B2 bin (black solid curve; see Table 5.1); the magenta solid curve represents the count rate distribution of sources above 10 background subtracted counts. Expectations from La Franca et al. (2005) luminosity function are shown in dashed curves, for unabsorbed ($\log N_H < 22$, orange) and Compton-thin ($22 < \log N_H < 24$, red) sources. Green dashed line indicates the lower limit used for Compton-thick candidates selection; the green shaded area represents the count rate range where Compton-thick AGN are expected to be found (see Section 5.4.1 for details).

all these sources are either unabsorbed or Compton-thin AGN (see above) and therefore very few Compton-thick AGN are expected in this subsample. Moreover, the magenta curve is very tightly related to the distribution of the X-ray detected sources: if a Compton-thick AGN produces an X-ray count rate value in this range, we should find it among the X-ray detected sources (see Section 5.4.1).
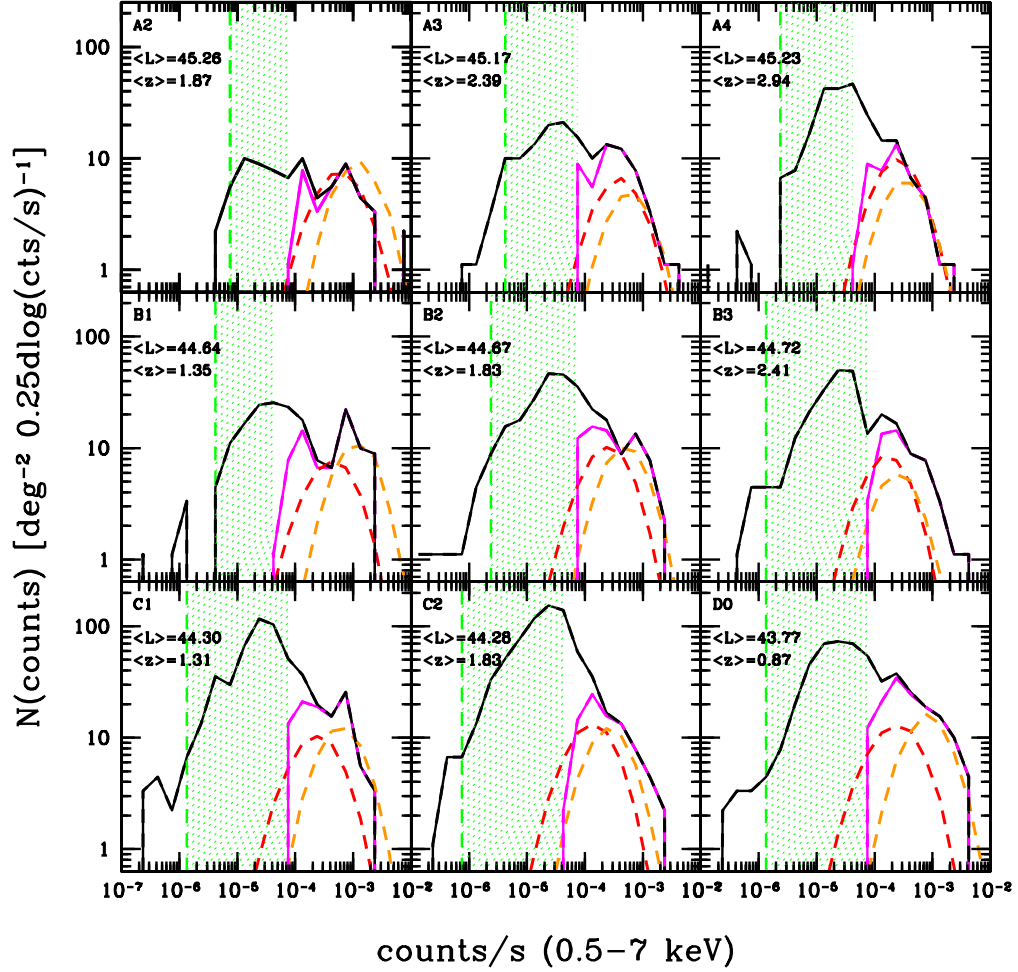
Figure 5.6: Expected and observed X-ray count rate distributions in the 9 COSMOS bins. Average 5.8 μm luminosity and redshift for each bin are reported. The color combinations are the same from Figure 5.5.

We then decided to carry out our analysis on those 24 μm sources having X-ray count rates in the interval between the green (lower limit of the expected Compton-thick distribution) and the magenta (lower limit of the observed sources with more than 10 background-subtracted counts) lines; this interval
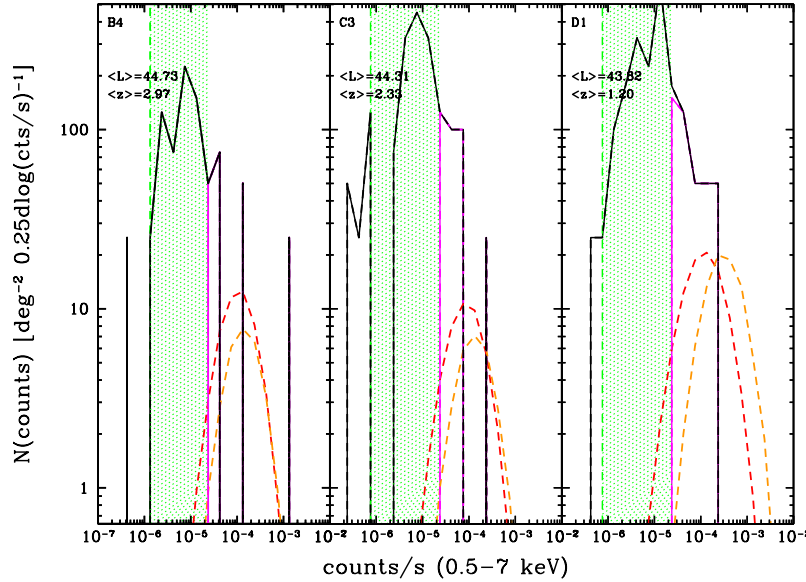
Figure 5.7: Same as Figure 5.6 for the 3 GOODS bins.

is showed with a green shaded area in Figure 5.5.

The same selection has been applied to all the 12 bins of the $L_{5.8} - z$ plane (see Figures 5.6 and 5.7). In Table 5.2 the number of sources that satisfy this selection criterion are reported in column (3).

It should be noted that changing the assumptions on the N_H distribution does not affect the position of the lower limit of the count rate distribution of Compton-thick AGN, but only their number density. However, as a further check, in a small number of bins we have also carried out our study on those sources with X-ray count rates below the lower count rates threshold.

5.4.2 Stacking analysis

Due to the very low count rates of the sources in our samples, it is not possible to study them individually with common spectral analysis techniques.

However, the high positional accuracy of *Chandra* X-ray data allows to superimpose (*stack* together) the X-ray images of several sources in order to increase the signal to noise ratio (SNR). This *stacking analysis* techinque increases the exposure time by tens to hundreds of times, and by a factor about square root of this value the sensitivity and the flux limit of the sample.

Several requirements have to be fulfilled in order to efficiently apply the stacking analysis technique. The positions of the stacked sources must be known with high precision, to avoid dispersion of the signal on a higher area and the inclusion of spurious counterparts. The stacked sources must also belong to the same population (i.e. with similar X-ray properties) in order to obtain a coherent average spectrum from the stacking of several individual sources. It should be avoided to include in the analysis bright sources (i.e. having fluxes much higher than the average flux of the other stacked sources); otherwise, the resulting spectrum would not represent an average property of the whole population, but it would be dominated by the brightest sources. To characterize the average X-ray properties of the above described samples, we performed a detailed stacking analysis of the *Chandra* counts at the infrared positions of each source, in order to obtain an average hardness ratio in each $L_{5.8} - z$ bin. Due to the different depth of the X-ray data available for the two surveys, COSMOS and GOODS sources were treated separately.

The upper X-ray count rate threshold that we have applied in our selection (see Section 5.4.1) allowed us to exclude from the analysis the brightest sources, that, as stated before, could dominate the resulting stacked spectrum. To reduce the background noise, we have further excluded from our analysis the candidates nearby X-ray detected sources, i.e. when a source was found in the X-ray catalog within a radius of 15 arcsec from the infrared position of the candidate. When dealing with COSMOS data, this led to the exclusion of less than 10% of the selected candidates, while in GOODS this fraction may reach, in some of the $L_{5.8} - z$ bins, $\sim 40 - 50\%$ of the sample.

This stacking analysis was performed in two energy bands, in order to evaluate in each bin the mean hardness ratio for the selected candidates. Following Fiore et al. (2009), we chose the $0.3 - 1.5$ keV and $1.5 - 6$ keV bands as soft and hard bands, as these energy bands give the best results in terms of SNR. The resulting stacked images are shown in Figures 5.8 to 5.19.

We performed several trials in order to chose the source extraction region in order that maximizes the SNR. A box with a 5 arcsec side (100 ACIS-I square pixels area) resulted to be the best possible choice; we obtained a slightly lower SNR using a box with a side of 4 arcsec.

We used the derived soft and hard X-ray stacked counts to compute, in each $L_{5.8} - z$ bin, the average hardness ratio for our Compton-thick candidate samples. We defined the hardness ratio and its error as

$$HR = \frac{H - S}{H + S},$$
(5.3)

$$\Delta HR = \sqrt{\frac{(H\Delta S)^2 + (S\Delta H)^2}{(H + S)^4}}.$$
(5.4)

The resulting hardness ratios, as well as the number of sources that entered the stacking analysis, are shown in Table 5.2.

5.4.3 CT AGN fraction in 24 μm samples

We used the hardness ratios derived for each $L_{5.8} - z$ bin from the stacked images to constrain the fraction of Compton-thick AGN to the total 24 μm sources in the selected X-ray count rates ranges. For this purpose, we developed a Monte Carlo code that simulates the X-ray count rates produced by a given population of sources (star-forming galaxies, Compton-thin & Compton thick AGN) as a function of the redshift, infrared luminosity and exposure time of each object.
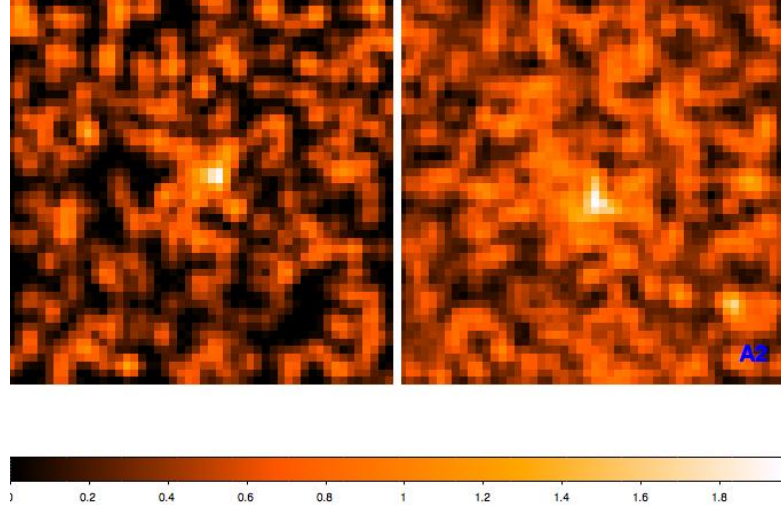
Figure 5.8: Stacked *Chandra* images in the soft $0.3 - 1.5$ keV (left) and in the hard $1.5 - 6$ keV (right) bands, in the A2 bin. Images have sides of $\sim 25''$ and have been smoothed with a Gaussian with $\sigma = 1''$.
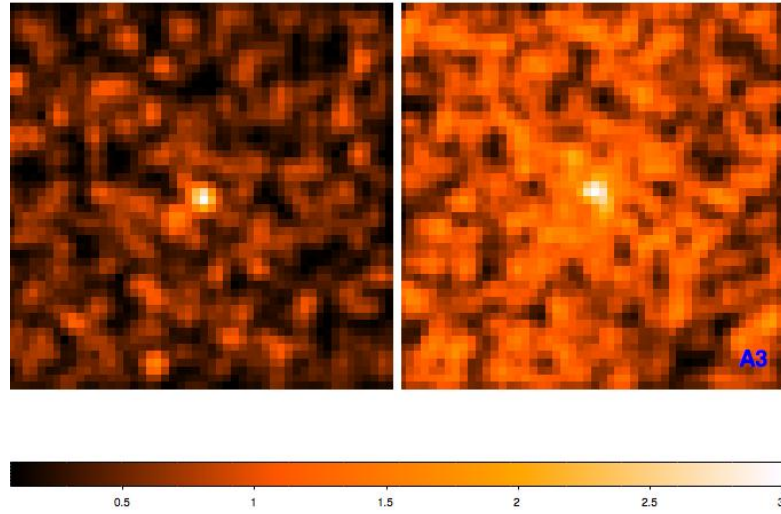

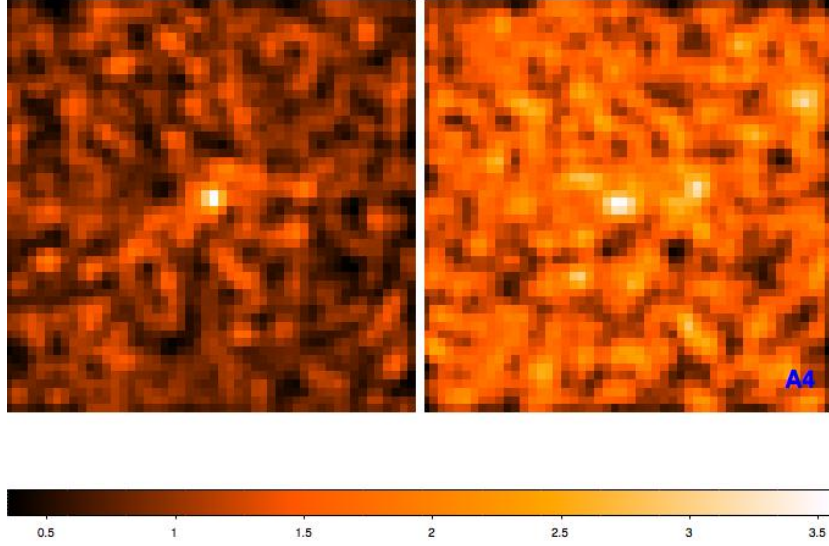Figure 5.9: Same as Figure 5.8, for bin A3.
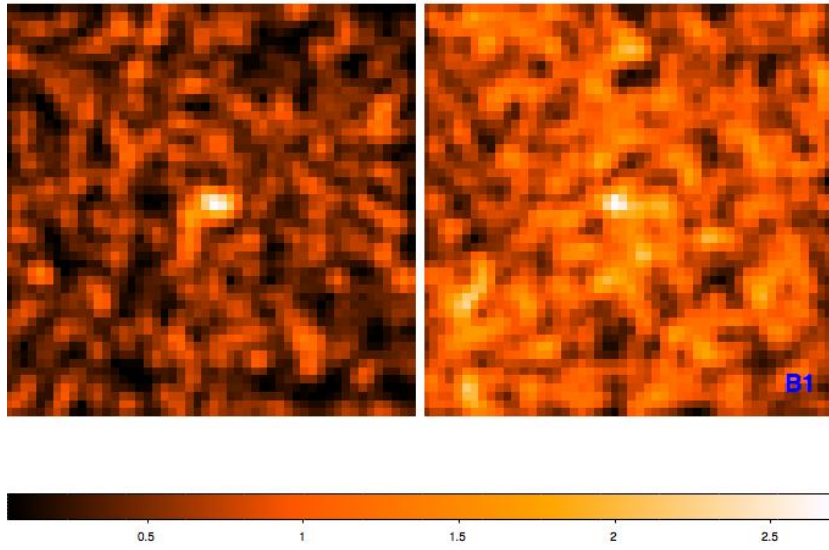
Figure 5.10: Same as Figure 5.8, for bin A4.

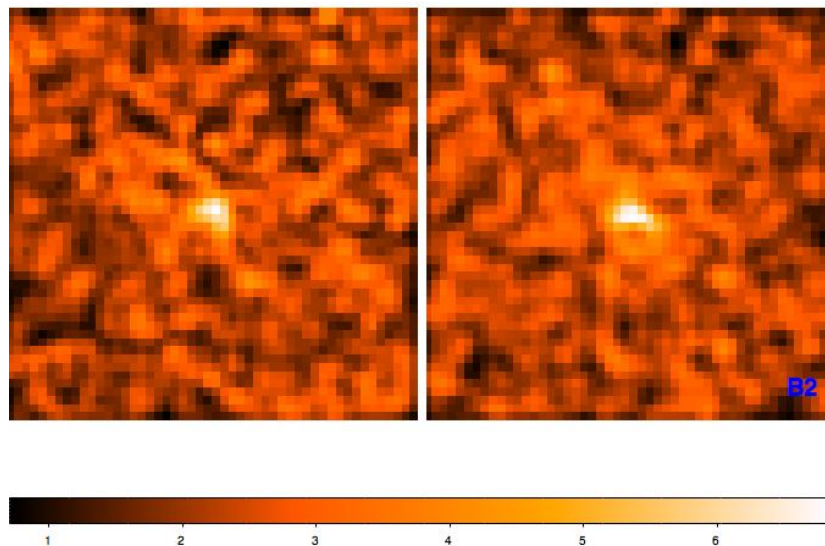Figure 5.11: Same as Figure 5.8, for bin B1.

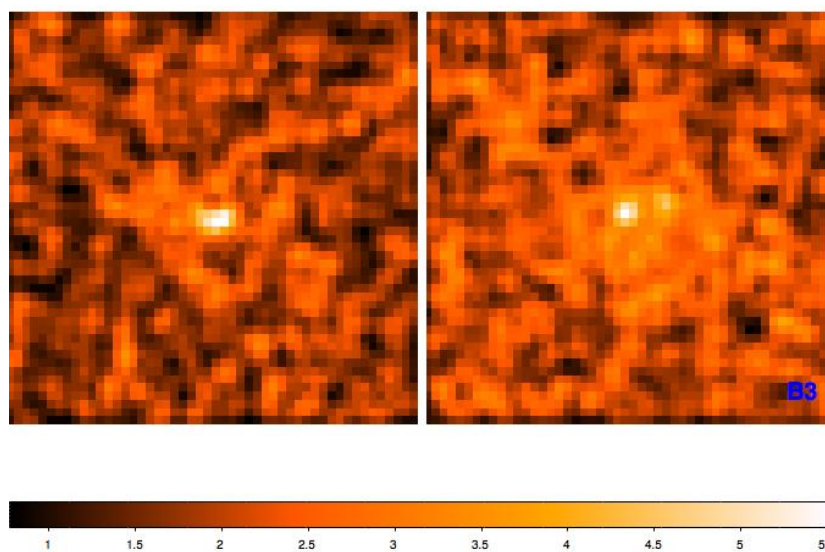Figure 5.12: Same as Figure 5.8, for bin B2.

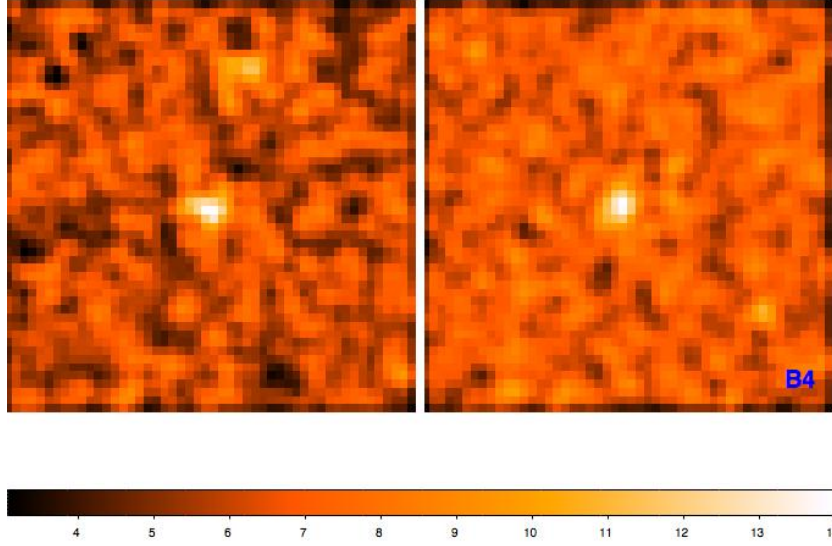Figure 5.13: Same as Figure 5.8, for bin B3.
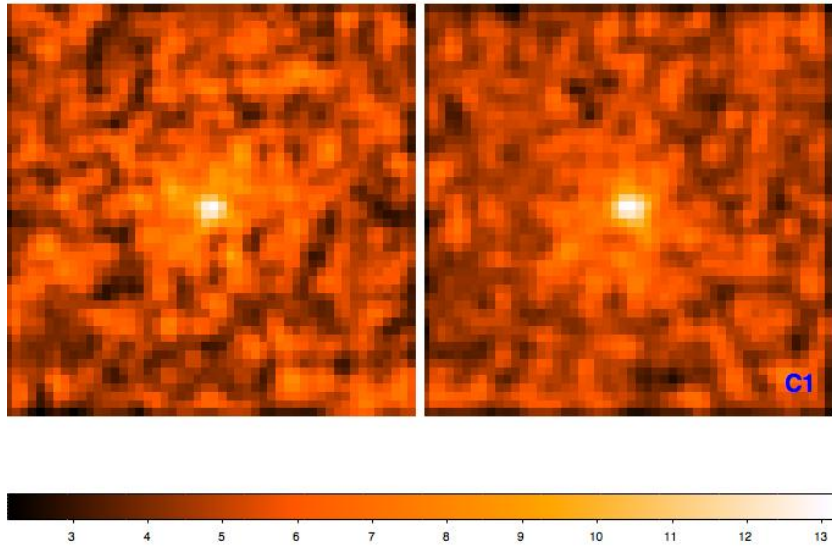
Figure 5.14: Same as Figure 5.8, for bin B4.

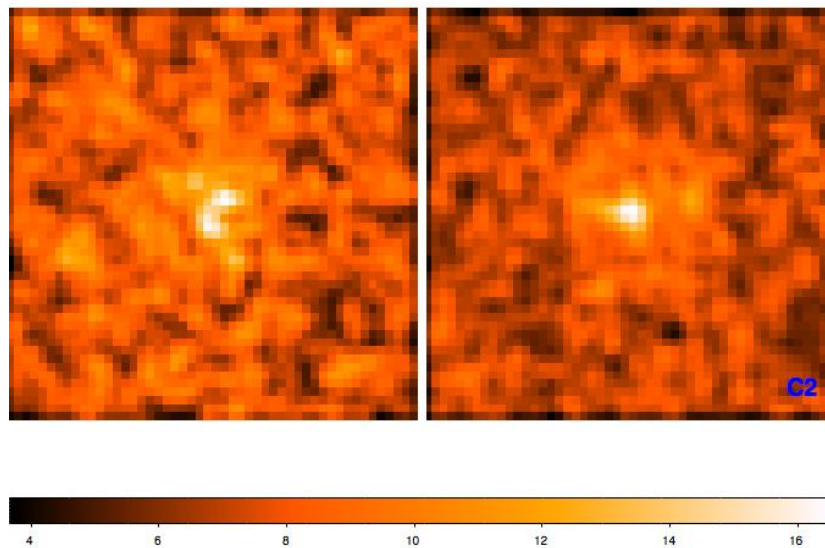Figure 5.15: Same as Figure 5.8, for bin C1.
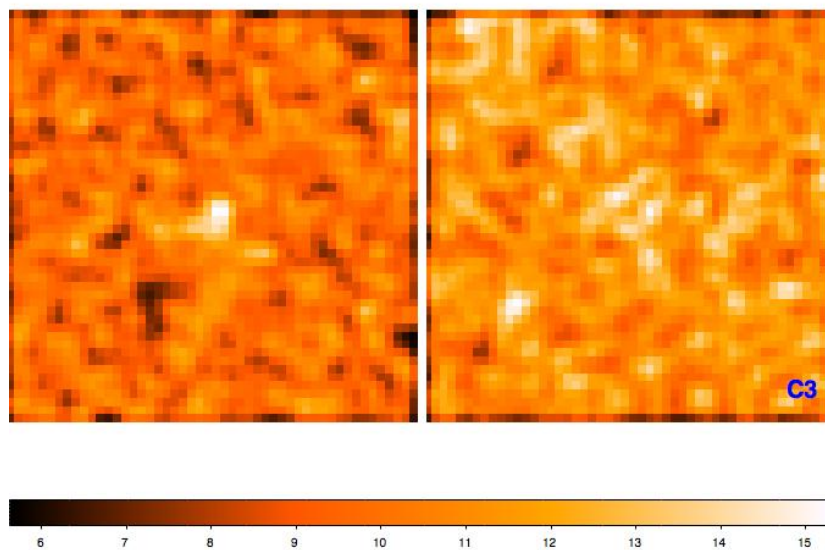
Figure 5.16: Same as Figure 5.8, for bin C2.

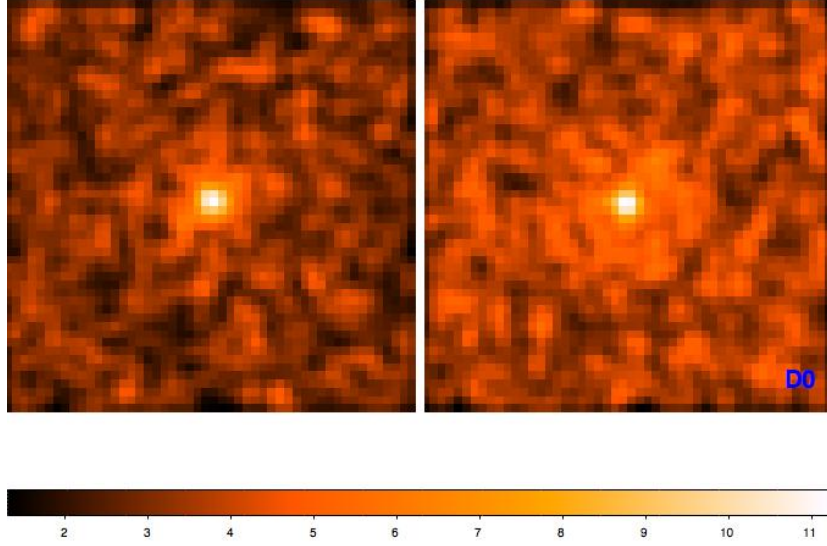Figure 5.17: Same as Figure 5.8, for bin C3.
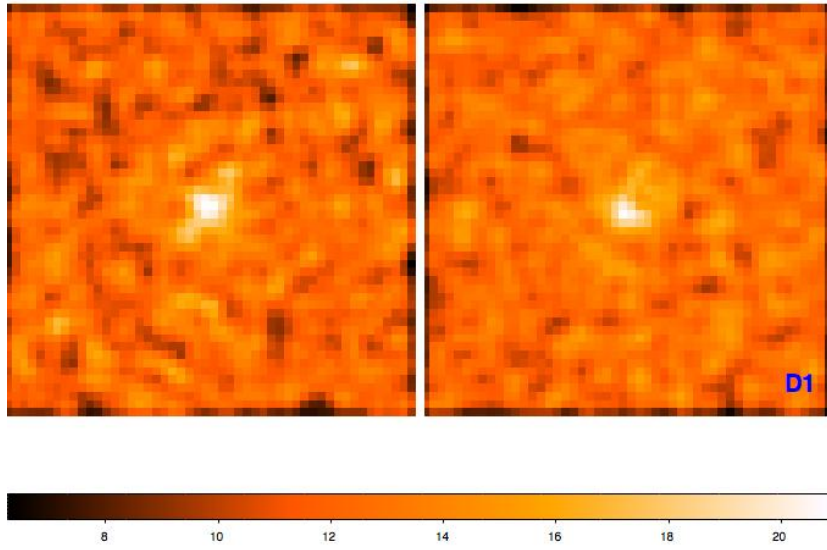
Figure 5.18: Same as Figure 5.8, for bin D0.

Figure 5.19: Same as Figure 5.8, for bin D1.

Table 5.2: Results of the stacking analysis of X-ray undetected sources.

bin	# of det sources	# of undet sources	hardness ratio $(H-S)/(H+S)$	CT/MIR fraction	CT density $\mathrm{Mpc}^{-3}\,\mathrm{d}\log L^{-1}$
A2	0	30	0.329 ± 0.181	$0.66^{+0.15}_{-0.15}$	$2.16^{+0.49}_{-0.49} \times 10^{-6}$
A3	0	52	0.317 ± 0.170	$0.62^{+0.14}_{-0.16}$	$4.65^{+1.05}_{-1.20} \times 10^{-6}$
A4	0	111	-0.094 ± 0.261	$0.24^{+0.25}_{-0.23}$	$1.69^{+1.78}_{-1.62} \times 10^{-6}$
B1	0	53	0.009 ± 0.331	$0.45^{+0.24}_{-0.44}$	$8.43^{+4.49}_{-8.24} \times 10^{-6}$
B2	0	131	0.447 ± 0.131	$0.73^{+0.10}_{-0.14}$	$2.58^{+0.35}_{-0.49} \times 10^{-5}$
B3	0	136	0.441 ± 0.166	$0.67^{+0.15}_{-0.15}$	$3.02^{+0.68}_{-0.68} \times 10^{-5}$
B4	2	17	0.287 ± 0.198	$0.47^{+0.22}_{-0.21}$	$4.78^{+1.68}_{-1.60} \times 10^{-5}$
C1	0	293	0.360 ± 0.087	$0.66^{+0.10}_{-0.09}$	$1.16^{+0.18}_{-0.16} \times 10^{-4}$
C2	0	412	0.354 ± 0.100	$0.61^{+0.10}_{-0.10}$	$2.99^{+0.49}_{-0.49} \times 10^{-4}$
C3	0	27	0.152 ± 0.258	$0.32^{+0.30}_{-0.26}$	$9.89^{+9.27}_{-8.03} \times 10^{-5}$
D0	0	236	0.173 ± 0.101	$0.46^{+0.10}_{-0.12}$	$6.34^{+1.38}_{-1.65} \times 10^{-5}$
D1	0	30	0.205 ± 0.139	$0.48^{+0.12}_{-0.18}$	$2.38^{+0.59}_{-0.89} \times 10^{-4}$

Using these simulations we computed the average hardness ratio, in each bin, as a function of the fraction of highly-obscured AGN, assuming that the sources are either Compton-thick AGN or star-forming galaxies. Actually, a small number of these sources may be indeed mildly obscured AGN; to account for this contamination we included in each simulation a fixed number of Compton-thin AGN, as expected from the La Franca et al. (2005) luminosity function. However, this contamination resulted to be negligible. Following Ranalli, Comastri & Setti (2003), for the star-forming objects we assumed a $\log(\lambda L_\lambda(5.8\mu\mathrm{m})/L(2-10\ \mathrm{keV}))$ luminosity ratio of 2.38, with a gaussian dispersion of 0.5 dex, and a power-law spectrum with an energy index $\alpha_{\mathrm{stb}} = 0.9$, with a gaussian dispersion of 0.1 dex; we also assumed that the star-forming galaxies are not affected by absorption.

For the AGN component, as already described in Section 5.4.1, we:
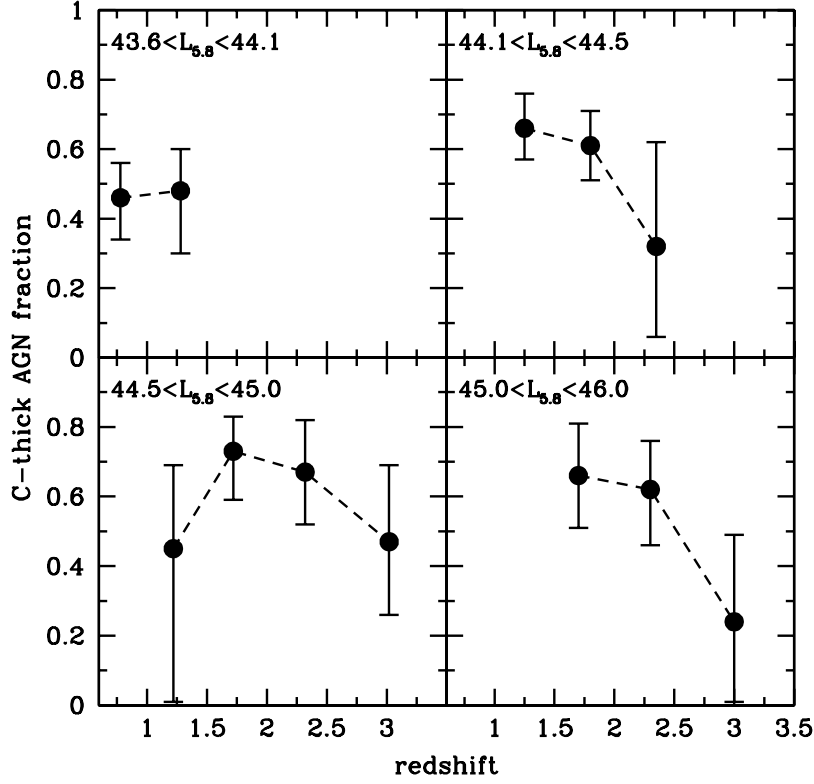
Figure 5.20: Fraction of Compton-thick AGN to the selected sources (with count rates in the range where Compton-thick AGN are expected; see Section 5.4.1) as a function of redshift.

1. converted the 5.8 μm luminosities into X-ray luminosities assuming Equations 5.1 and 5.2 for the Compton-thin and Compton-thick AGN, respectively;

2. assumed the X-ray spectra shown in Figure 5.4;

3. used the N_H distribution following La Franca et al. (2005).

For each assumed fraction of highly-obscured AGN a total of 50 series of simulations have been carried out. To produce a Compton-thick AGN, we

randomly pick a redshift/luminosity/exposure set of values from our selected sample of candidates and a N_H value from the column density distribution; the sets of values used to generate the star-forming galaxies and Compton-thin AGN were instead taken from the whole population sample in the $L_{5.8}-z$ bin. All simulated sources, whose count rates resulted to be outside the range of the parent sample (see Section 5.4.1), were excluded from the analysis and a new object was generated. We conservatively requested that the Compton-thin AGN were so bright to have count rates very close (within 0.1 dex) to the upper limit value of the parent sample.

We used the output of these simulations to convert the hardness ratios obtained from the stacking analysis into the fractions of Compton-thick AGN to the 24 μm sources having X-ray count rates included in the selected ranges (see Section 5.4.1); these fractions are reported in Table 5.2. The same fractions are also shown in Figure 5.20 as a function of redshift.

As stated in Section 5.4.1, in order to check how much effective our count rate selection criterion was, we also stacked together the X-ray counts of the 24 μm sources having count rates lower than those in the ranges defined in Section 5.4.1. In this case it resulted that the average hardness ratio was, as expected, definitely smaller and compatible with a population of star forming galaxies only.

5.5　Density of Compton-thick AGN

We studied the X-ray count rate distribution of our 24 μm selected sample in order to define the range of values in which is most likely to find the emission from Compton-thick AGN, and then studied, in several $L_{5.8} - z$ bins, the spectral X-ray properties to constrain the fraction of highly obscured AGN. These measures allowed us to derive, from the volume densities of the 24 μm sources, the Compton-thick AGN volume densities.
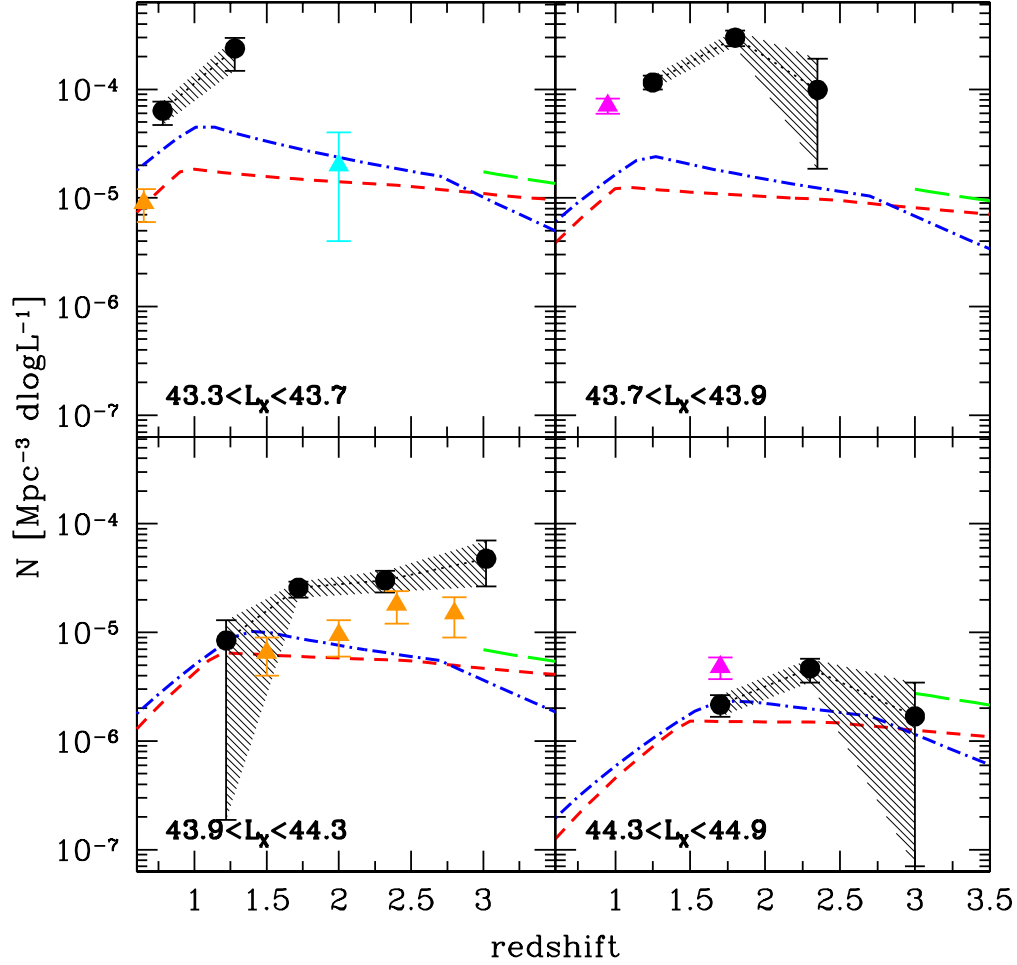
Figure 5.21: Volume density of 24 μm selected Compton-thick AGN as a function of redshift. Black filled circles show the measurements described in this work. Filled triangles represent the results from previous works (see Section 5.1): Fiore et al. (2009, magenta), Treister et al. (2010, orange), Alexander et al. (2011, cyan). The dashed lines show the expectations from La Franca et al. (2005, red), Gilli, Comastri & Hasinger (2007, blue) and Fiore et al. (2012, green) luminosity functions.
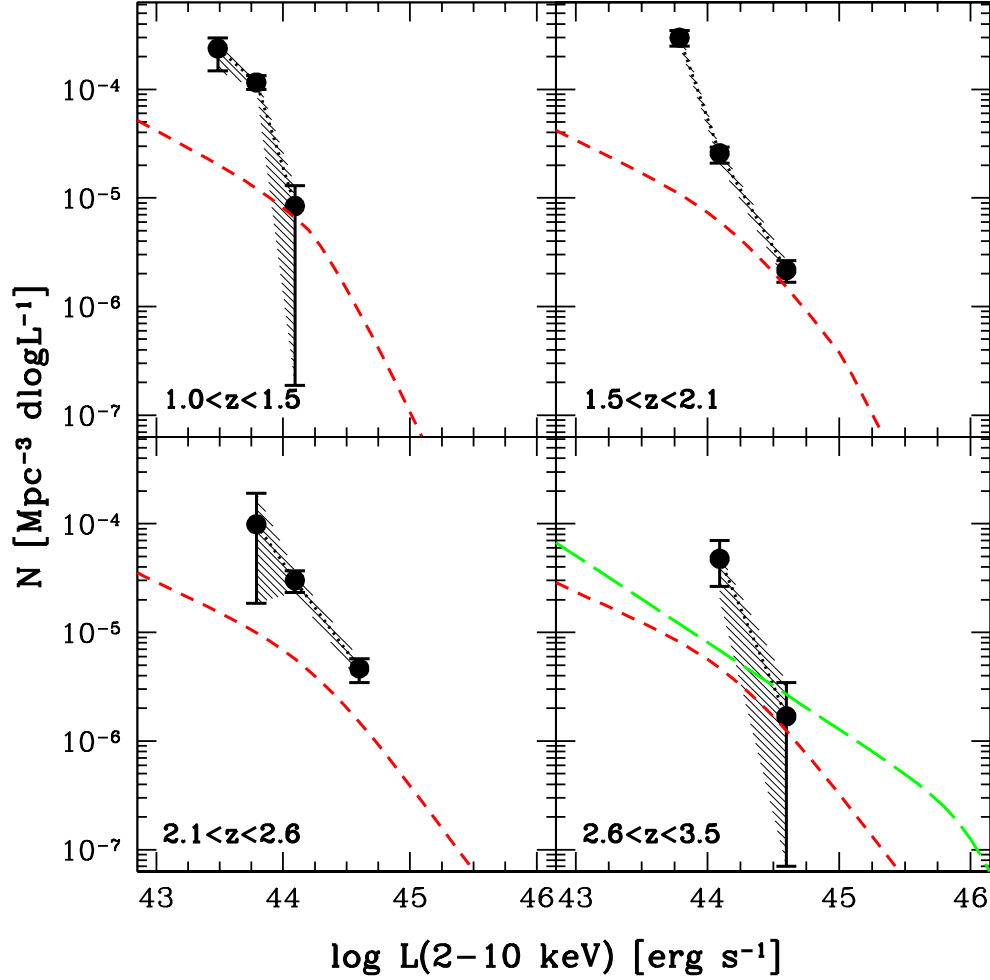
Figure 5.22: Volume density of 24 μm selected Compton-thick AGN as a function of $2-10$ keV X-ray luminosity. Black filled circles show the measurements described in this work. The dashed lines show the expectations from La Franca et al. (2005, red) and Fiore et al. (2012, $z > 3$, green) luminosity functions.

In each $L_{5.8} - z$ bin, we evaluated the space density of the 24 μm sources having X-ray count rates included in the selection ranges discussed in Section 5.4.1 by applying the $1/V_{\mathrm{max}}$ method from Schmidt (1968, see Section 3.3)

and corrected this value for the corresponding fraction of Compton-thick AGN constrained in Section 5.4.3. To obtain the total Compton-thick AGN densities, the contribution due to the X-ray detected Compton-thick AGN from Brightman & Ueda (2012), as discussed in Section 5.3, was added to the GOODS data.

In COSMOS we did not include any contribution from X-ray detected sources. As stated in Section 5.3, we found only a few sources per bin that are compatible with Compton-thick AGN emission. This contribution is negligible if compared to the contribution due to the undetected sources (see Table 5.2); therefore, we decided to ignore it. Our results are reported in Table 5.2 (column 8 and 9).

In Figure 5.21 the densities of Compton-thick AGN as a function of redshift are shown and compared with previous results from Fiore et al. (2009) and Treister et al. (2010), as well as with the model expectations from La Franca et al. (2005), Gilli, Comastri & Hasinger (2007), Fiore et al. (2012); the same measures as a function of the X-ray luminosity are presented in Figure 5.22. While at high luminosities our results are in fairly good agreement with previous luminosity function measures, for $L_X < 10^{44}$ erg s^{-1} the Compton-thick densities result to be considerably higher, up to a factor of ~ 10 at $L_X \simeq 10^{43}$ erg s^{-1}, than earlier reported.

5.6 AGN fraction in 24 μm samples

The measure of the Compton-thick AGN fraction that we carried out in Section 5.4.3 allowed us to evaluate the fraction of AGN to the 24 μm selected galaxy sample.

The fractions of highly obscured AGN, f_{stack} (measured in Section 5.4.3), were limited to the X-ray count rate ranges defined in Section 5.4.1. Therefore, we computed the fraction of highly obscured AGN to the total 24 μm sample
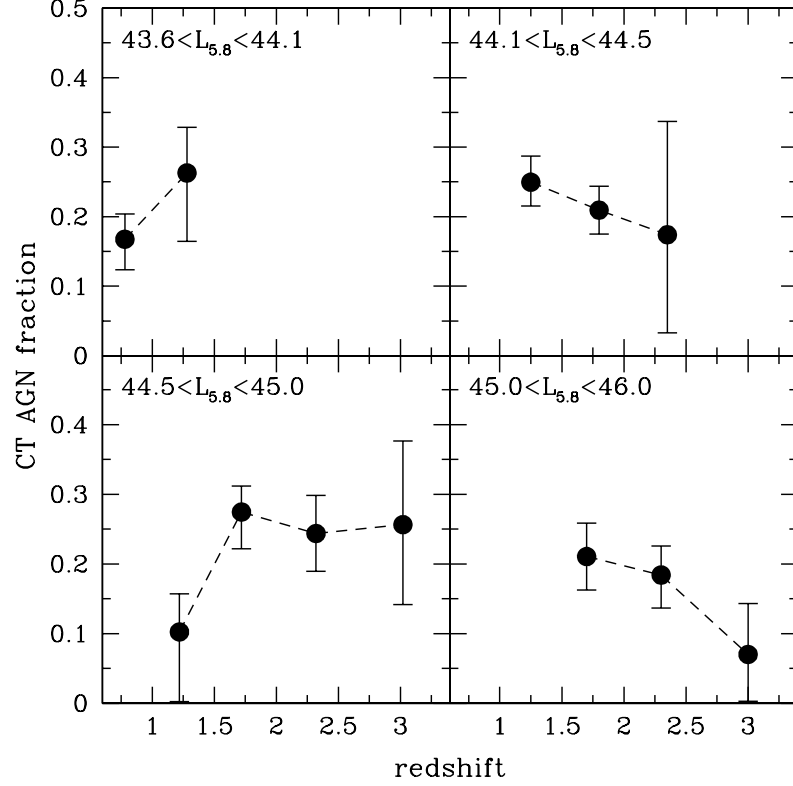
Figure 5.23: Fraction of Compton-thick AGN to the total 24 μm sources in each $L_{5.8} - z$ bin. See Section 5.6 for details.

using the following formula:

$$f_{CT} = \frac{f_{\text{stack}} N_{\text{stack}}}{N_{24}}, \qquad (5.5)$$

where N_{stack} and N_{24} represent the number of stacked and total 24 μm sources, respectively. The result of this computation is shown in Figure 5.23 as a function of redshift.

The luminosity function from La Franca et al. (2005) has then been assumed to compute, in each $L_{5.8} - z$ bin, the expected number N_{LF} of unobscured and mildly obscured AGN. This contribution has been used, in each bin, to
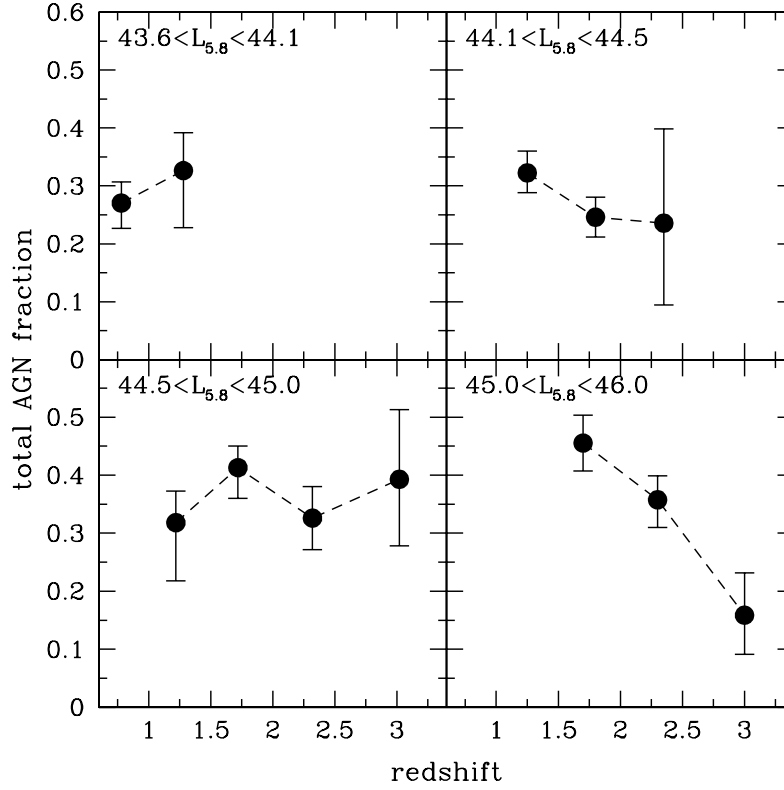
Figure 5.24: Fraction of AGN (unobscured, Compton-thin and Compton-thick) to the total 24 μm sources in each $L_{5.8} - z$ bin. See Section 5.6 for details.

derive the fraction of AGN to the total 24 μm sample:

$$f_{\mathrm{AGN}} = \frac{f_{\mathrm{stack}} N_{\mathrm{stack}} + N_{\mathrm{LF}}}{N_{24}}. \tag{5.6}$$

The final result is presented in Figure 5.24.

5.7 AGN duty cycle

The knowledge the fraction of Compton-thick AGN to the whole 24 μm source population, along with previous estimation of the luminosity function

Figure 5.25: AGN duty cycle as a function of redshift. Shaded areas represent the expectations from Fiore et al. (2012) for $\log M_* = 11.75\ M_\odot$ (green) and $11.25\ M_\odot$ (red). Filled squares and triangles respectively show the results from Brusa et al. (2009b), for X-ray selected AGN only, having the same stellar masses and $L_X > 10^{43}$ erg s^{-1}.

of unabsorbed and Compton-thin AGN, can be used to evaluate the AGN
duty cycle, that represents the fraction of galaxies undergoing nuclear activity
to the total number of galaxies having the same mass.

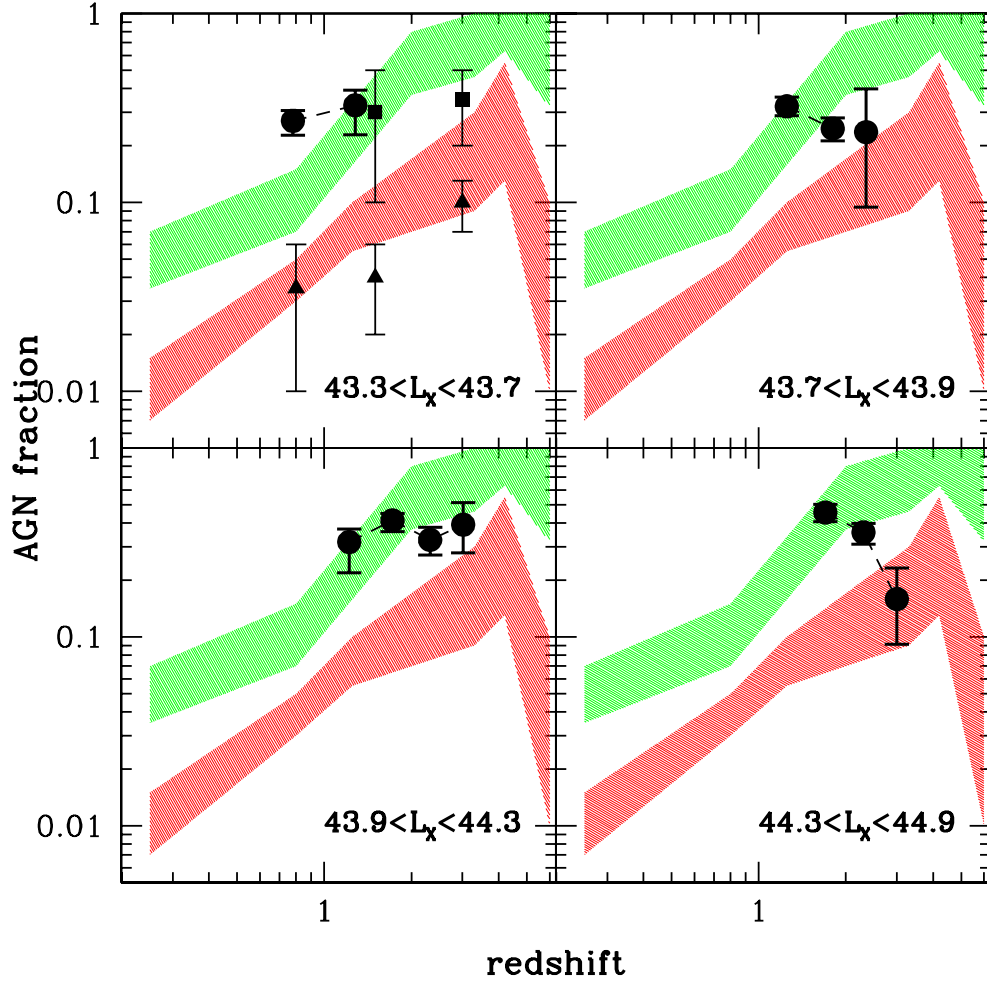We adopted for the AGN duty cycle the same definition from Fiore et al.
(2012), which defined the duty cycle as the fraction of AGN with $2 - 10$ keV
luminosity $L_X > 10^{43}$ erg s^{-1} to the total number of galaxies having the
same stellar mass. It should be noted that, according to this definition, the
AGN duty cycle and the AGN timescale can be different, since the latter is
related to the intrinsic lifetime of the AGN and so may include phases of
lower luminosity.

To evaluate the AGN duty cycle, we computed in each $L_{5.8} - z$ bin the
contributions from Compton-thick AGN and from unobscured and mildly
obscured AGN. The contribution from Compton-thick AGN has been ob-
tained by correcting the number of 24 μm sources in each bin for the fraction
of Compton-thick AGN derived in Section 5.6; it should be noted that, if
we assume Equation 5.2 to convert 5.8 μm luminosities into X-ray luminosi-
ties, all the 24 μm sources in our sample have X-ray luminosity greater than
10^{43} erg s^{-1}. In order to compute the contribution from unobscured and
Compton-thin AGN, we have integrated in each $L_{5.8} - z$ bin the X-ray LF
from La Franca et al. (2005) for $L_X > 10^{43}$ erg s^{-1}, according to our definition
of the AGN duty cycle:

$$N_{\text{unobsc+C-thin}} = \int \frac{\mathrm{d}\Phi(L_X, z)}{\mathrm{d}\log L_X} \mathrm{d}V(z) \mathrm{d}\log L_X. \tag{5.7}$$

Figure 5.25 shows our results, and the comparison with the estimates from
Fiore et al. (2012) for two specific stellar mass bins for AGN. These esti-
mates are derived from the X-ray luminosity function, by: a) converting
them into "active" SMBH mass function, using Monte Carlo simulations and
assuming a bolometric correction factor (e.g. Marconi et al. 2004) and a dis-
tribution of Eddington ratios; b) transforming these SMBH mass functions

into galaxy mass functions of active galaxies, assuming a conversion factor between SMBH mass and host galaxy mass (see e.g. Häring & Rix 2004); c) dividing the active galaxy mass functions by the galaxy stellar mass functions.

We found, for the AGN duty cycle, an almost constant value (around $\sim 30\%$) in the redshift range $z = 1 - 3$. A similar result has been found by Brusa et al. (2009b), which observed that the AGN fraction increases with increasing stellar mass from values smaller than 1% for $M_* \simeq 10^{10} \ M_\odot$ up to $\sim 30\%$ for $M_* > 3 \times 10^{11} \ M_\odot$.

The measure of the AGN duty cycle as a function of redshift is a useful tool to discriminate among different AGN triggering mechanisms. Two main scenarios have been proposed so far: galaxy mergers (see e.g. Barnes & Hernquist 1996; Menci et al. 2008) and recycled gas from normal stellar evolution in the inner regions (Ciotti & Ostriker 2007; Ciotti, Ostriker & Proga 2010). Different predictions on the AGN duty cycle arise from these models: in the galaxy encounters scenario, a strong increase of the duty cycle with redshift is expected, since these events are more frequent in the past, when, at the same time, more gas is available for nuclear accretion. On the other side, in the recycled star gas scenario the AGN timescale is much longer, and a slower variation of the duty cycle with redshift is thus expected.

5.8 Accretion history in the universe

The measure of the volume density of Compton-thick AGN that we discussed in Section 5.5 directly constrains the contribution of highly obscured AGN to the cosmological history of accretion of supermassive black holes in the galactic centers. Again, by adding the contribution of unobscured and moderately obscured sources, it is possible to estimate the total mass accreted by the whole AGN population up to present day.

In Section 2.7 we have discussed how the local (relic) density of SMBH should be accounted for by integrating the overall density released by AGN. To perform this computation we must assume a radiative efficiency ϵ and a bolometric correction factor to convert the $2-10$ keV luminosities into bolometric luminosities:

$$L_{\text{bol}} = K_{\text{bol}}(L_{\text{X}})L_{\text{X}}. \tag{5.8}$$

We assumed a typical value of $\epsilon = 0.1$ (see Marconi et al. 2004; Vasudevan & Fabian 2009) for the radiative efficiency, and adopted the luminosity-dependent bolometric correction from Marconi et al. (2004):

$$K_{\text{bol}}(L_{44}) = 33.698 + 23.948L_{44} + 10.542L_{44}^2 + 3.567L_{44}^3 + 0.918L_{44}^4 + 0.110L_{44}^5, \tag{5.9}$$

where

$$L_{44} = \log \frac{L_X}{10^{44} \text{ erg s}^{-1}}. \tag{5.10}$$

Under these assumption, we can integrate Equation 2.21, assuming that the initial mass of seed black hole at redshift z_{s} is negligible, and compute the total accreted black hole mass due to Compton-thick AGN in our 24 μm selected sample. This quantity corresponds to a black hole mass density in the local universe of $\rho_{\text{BH, CT}} = 1.28 \times 10^5 \ M_\odot \ \text{Mpc}^{-3}$. This density is related only to Compton-thick AGN having 5.8 μm luminosities and redshifts included in the $L_{5.8} - z$ grid that has been used in our analysis. To compute the total accreted local black hole mass density, the contribution from unobscured and mildly obscured AGN, as well as the contribution from Compton-thick AGN that lie outside the grid, must be accounted for. For all these populations, number densities from La Franca et al. (2005) LF have been used. Once these contributions have been included, we obtain a total accreted black hole mass density of

$$\rho_{\text{BH}} = 3.55 \times 10^5 \ M_\odot \ \text{Mpc}^{-3}. \tag{5.11}$$

The BH density in Equation 5.11 is consistent with previous estimations obtained from $M_{BH}-$bulge relations, that lie in the range $\rho_{BH} = (4.2-5.1) \times 10^5 \ M_\odot \ \mathrm{Mpc}^{-3}$, and with the prediction of recent evolutionary models (see Merritt & Ferrarese 2001; Fukugita & Peebles 2004; Marconi et al. 2004; Graham 2007).

5.9 Discussion and conclusions

We have measured the space density of Compton-thick AGN in several $L_{5.8}-z$ bins by correcting the density of 24 μm selected sources in each bin with the corresponding fraction of Compton-thick AGN to the total 24 μm population. As shown in Figure 5.22, we found a strong increase with decreasing X-ray luminosity in the space density of highly obscured sources. This trend has been observed by several authors (Ueda et al. 2003; La Franca et al. 2005) in the evolution of the moderately obscured AGN population. While at $2 - 10$ keV luminosities higher than 10^{44} erg s^{-1} our measures are in fair agreement with luminosity function models expectations (La Franca et al. 2005), around $\simeq 10^{43}$ erg s^{-1} we have the first observational evidence that the number density of Compton-thick AGN is considerably higher than previous luminosity function expectations.

This result does not depend on the particular choice of the N_H distribution: choosing a different N_H distribution could modify the expected number of Compton-thick AGN at a given X-ray count rate value, but the lower limit of the count rate range where the Compton-thick sources are expected to be found (as discussed in Section 5.4.1) remains the same. Moreover, we have verified that below these lower limits the sources in our sample are mostly star forming galaxies, as discussed in Section 5.4.3.

Several observational evidences and theoretical model predictions suggest the existence of such a population of obscured sources. A significant fraction

of Compton-thick sources above $z > 1.5$ is required to fit the peak of the CXRB around ~ 30 keV (Gilli, Comastri & Hasinger 2007). In the galaxy formation model by Menci et al. (2008), at $z > 2$, the predicted density of low-luminosity ($L_X \lesssim 10^{43}$ erg s^{-1}) AGN is a factor of 2 above the observation, thus suggesting the existence of a relevant fraction of Compton-thick sources in these redshift and luminosity intervals.

Several recent works have been focusing on the search of highly obscured AGN in deep X-ray surveys (like the CDFS and C-COSMOS). In most cases, the authors selected samples of Compton-thick candidates using mid infrared to optical colors. Fiore et al. (2009) estimated that the space density of Compton-thick AGN is 4.8×10^{-6} Mpc^{-3} for $z = 1.2 - 2.2$ and $\log L_X = 44 - 45$, and 3.7×10^{-5} Mpc^{-3} for $z = 0.7 - 1.2$ and $\log L_X = 43.5 - 44.3$. Their analysis was performed with a brighter 24 μm sample selection (a factor of 7 higher than this work). They found slightly higher densities in the high luminosity bin, while for the low luminosity bin their measure cannot be directly compared with ours, due to the different redshift ranges. Treister et al. (2010) found a significant number of Compton-thick sources with X-ray luminosities above 10^{44} erg s^{-1} at $z > 2.5$, followed by a decline of a factor of 3 up to $z \sim 1.5$. In the $\log L_X = 43.9 - 44.3$ bin, which can be used for a comparison, we found a higher density of highly obscured sources than Treister et al. (2010), and a less strong decline (a factor of ~ 2) at lower redshifts.

Alexander et al. (2011) estimated the space density of $L_X > 10^{43}$ erg s^{-1}, $z = 1.4 - 2.6$ highly obscured sources in the CDFS, selected using the BzK technique. We cannot directly compare our measures with their estimations, because in the same redshift bin we can only select brighter sources. However, we note that the Alexander et al. (2011) estimate is in good agreement with the luminosity function model predictions from La Franca et al. (2005) and Gilli, Comastri & Hasinger (2007), while our results are significantly higher
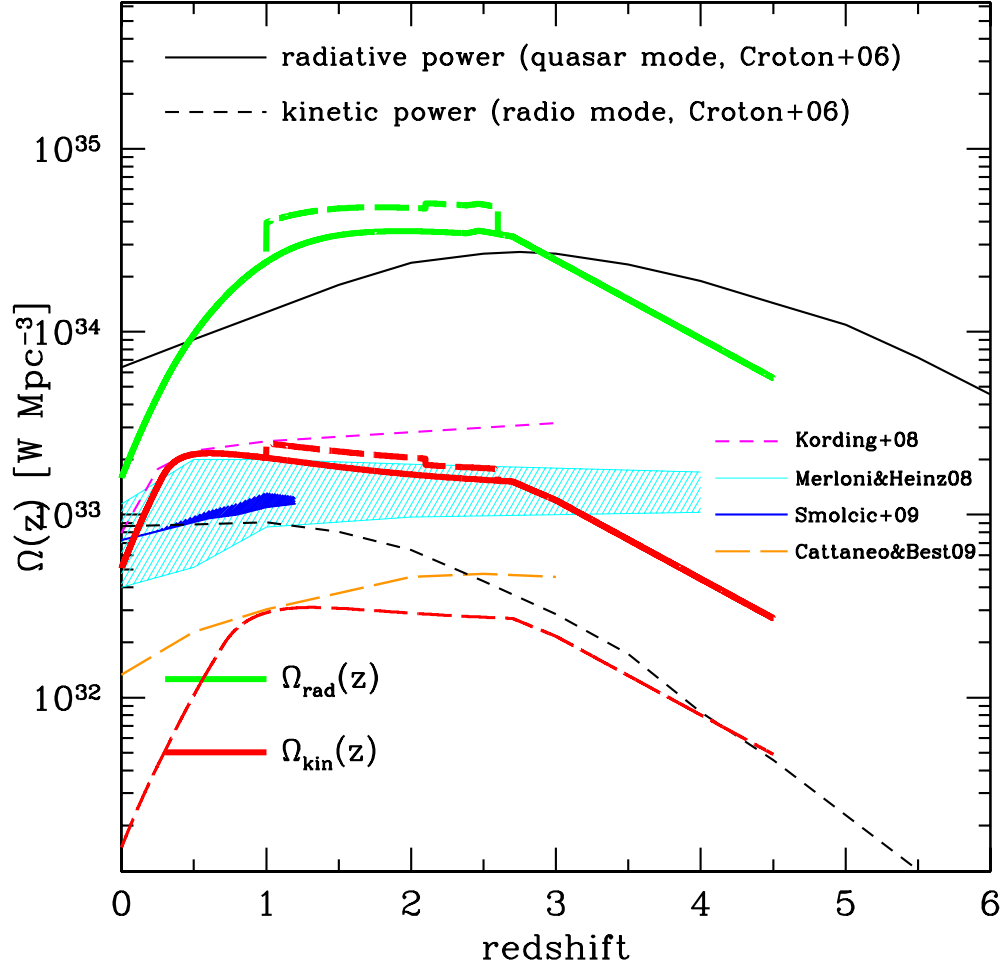
Figure 5.26: Radiative (green) and kinetic (red) power density of AGN as a function of redshift (see Figure 4.11). The dashed lines show the resulting power when the densities of Compton-thick AGN are corrected to reproduce the estimations discussed in Section 5.5.

below $z = 1$; the authors pointed out that their estimation should be regarded only as a lower limit of the true Compton-thick density, since their sample do not include distant sources not selected using the BzK technique.

In Chapter 4 we have computed the 1.4 GHz luminosity function of AGN by convolving the $2 - 10$ keV luminosity function with the previously derived probability distribution function of the ratio between 1.4 GHz and X-ray luminosities. This 1.4 GHz luminosity function has then been convolved with a relation between kinetic and radio luminosities in order to derive the kinetic power density output of AGN.

We can now correct our previous estimation (see Section 4.3 and Figure 4.11) by including in Equations 4.11 and 4.12 the contribution from Compton-thick undetected sources as measured in Section 5.5. We have first corrected, in each bin, the expected density of Compton-thick AGN in order to match the results of our measures. We have increased the luminosity function expectations by a factor of 10 in the range between $\log L_X = 43.3 - 43.7$ and $z = 1.0 - 2.1$ and between $\log L_X = 43.7.43.9$ and $z = 2.1 - 2.6$ and by a factor of 5 in the range between $\log L_X = 43.7 - 43.9$ and $z = 1.0 - 2.1$ and between $\log L_X = 43.9 - 44.3$ and $z = 2.1 - 2.6$. The resulting radiative and kinetic power densities are shown in Figure 5.26. After applying this correction, we found that the radiative power density increases by a factor of 1.5, while the kinetic power density is only $\sim 20\%$ higher in the redshift range $z = 1 - 3$.

We have then derived an upper limit on both $\Omega_{\mathrm{kin}}(z)$ and $\Omega_{\mathrm{rad}}(z)$ by increasing the luminosity function expectation for Compton-thick AGN ($N_H = 10^{24} - 10^{26}$ cm^{-2}) with intrinsic X-ray luminosities below 10^{44} erg s^{-1} and in the redshift range $z = 1 - 3$ by a factor of 10. In this scenario, the resulting power densities could be (at most) a factor of ~ 3 higher.

In summary, our new measures of an higher density of Compton-thick AGN do not change significantly the conclusions derived by our previous work on the radio/kinetic power density and feedback from AGN.

Chapter 6

Concluding remarks

Feedback from black holes is believed to play a key role in the context of the galaxy formation and evolution. Therefore, completing the census of accreting black holes during cosmic time represents a major challenge for modern astrophysics. While X-ray surveys are able to detect sources not affected by strong absorption, Compton-thick AGN are usually missed, although these sources are believed to represent a significant fraction of the whole AGN population.

In Chapter 5 we have measured the space density of Compton-thick AGN in 24 μm selected samples from COSMOS and GOODS, where deep *Chandra* observations exist, using the latest data releases available. We have used a new selection criterion, taking advantage of luminosity function model predictions, in order to select a population of Compton-thick candidates, which have been confirmed through X-ray spectral analysis of stacked data. Our measures show that:

- at high luminosities ($L_X > 10^{44}$ erg s^{-1}) the Compton-thick AGN densities are compatible with previous luminosity functions estimations;

- at low luminosities ($L_X \sim 10^{43}$ erg s^{-1}) are significantly higher than

the luminosity function estimations, as required by several galaxy formation models and CXRB synthesis models;

- we found that the Compton-thick AGN density increases with decreasing luminosity, in a similar way to the moderately obscured AGN;

- our predicted local density of relic BH, due to obscured and unobscured accretion, is consistent with the estimations derived from the local scaling relations and with the model predictions.

Some models predict that the same cold gas that fuels black hole accretion and star formation is responsible of AGN obscuration. In this scenario, the more powerful AGN clean their line of sight more quickly than low luminosity AGN; therefore, the fraction of obscured AGN should increase for decreasing luminosity, as observed in Compton-thin sources, in agreement with our findings.

In addition of obtaining a complete census of accreting black holes, the quantification of the AGN feedback on their host galaxies is another fundamental ingredient in order to fully understand the cosmological evolution of galaxies. In this context, the measure of the probability distribution of the ratio R_X between radio and X-ray luminosities is required for a correct estimation of the radio feedback of AGN.

As discussed in Chapter 4, we used a sample of more than 1600 X-ray selected AGN observed at 1.4 GHz to measure the probability distribution function $P(R_X|L_X, z)$ as a function of the X-ray luminosity and redshift. The knowledge of the $P(R_X|L_X, z)$ distribution is necessary to estimate the AGN kinetic (radio) feedback into the hosting galaxies by allowing to couple it with the luminous, accreting, phases of the AGN activity. The average value of R_X increases with decreasing X-ray luminosities and (possibly) increasing redshift. At variance, we did not find a statistical significant difference between the radio properties of the X-ray absorbed ($N_H > 10^{22}$ cm^{-2}) and

unabsorbed AGN.

We were able to better measure the densities of the more radio quiet ($R_X < -4$) AGN which resulted to be responsible of about half of the derived kinetic power density.

According to our analysis the value of the kinetic energy density is in qualitative agreement with the last generation galaxy evolution scenarios, where radio mode AGN feedback is invoked to quench the star formation in galaxies and slow down the cooling flows in galaxy clusters. However at redshifts below 0.5, similarly to what observed by Körding, Jester & Fender (2008), we found a sharp (about a factor of five) decrease of the kinetic energy density, which is strictly related the AGN density evolution, but which is not included in many of the galaxy/AGN formation and evolution models where, instead, the radio mode feedback is assumed to continuously increase (or only smoothly decrease) at low redshift.

We have also verified that our findings on a higher density of low luminosity Compton-thick AGN with respect to luminosity function expectations do not change significantly the conclusions derived by this work.

The topics discussed in this Ph.D. thesis have been the subject of the following papers:

- La Franca, F., Melini, G., & Fiore, F., "*Tools for computing the AGN feedback: radio-loudness distribution and the kinetic luminosity function*" 2010, AJ, 718, 368;

- Bonchi, A., La Franca, F., Melini, G., Bongiorno, A., & Fiore, F., "*On the AGN radio luminosity distribution and the black hole fundamental plane*" 2013, MNRAS, in press (arXiv:1211.2688);

- Melini, G., Fiore, F., La Franca, F., et al. 2013, close to submission to A&A.

The same topics have been presented, either as invited talks, contributed talks or posters, in several workshops and conferences.

Appendices

Appendix A

The BH Fundamental Plane

The radio data set presented in Section 3.4 has been used to extend the results presented in Chapter 4 to a determination of the BH fundamental plane (see Merloni, Heinz & Di Matteo 2003). This work has been performed by Andrea Bonchi during his Master Degree Thesis; my contribution on it was mainly on the data set issues. In this Appendix the paper concerning the topics discussed in this work is presented.

On the radio luminosity distribution of active galactic nuclei and the black hole fundamental plane

A. Bonchi,[1] F. La Franca,[1]⋆ G. Melini,[1] A. Bongiorno[2] and F. Fiore[2]

[1]*Dipartimento di Fisica, Università Roma Tre, Via della Vasca Navale 84, I-00146 Roma, Italy*
[2]*INAF Osservatorio Astronomico di Roma, Via Frascati 33, I-00044 Monte Porzio Catone, Italy*

ABSTRACT

We have studied the dependence of the nuclear radio (1.4 GHz) luminosity of active galactic nuclei (AGN) on both 2–10 keV X-ray and host-galaxy K-band luminosities. A complete sample of 1268 X-ray-selected AGN (both type 1 and type 2) has been used, which is the largest catalogue of AGN belonging to statistically well-defined samples where radio, X-ray and K-band information exists. At variance with previous studies, radio upper limits have been taken into account statistically using a Bayesian maximum-likelihood fitting method. A good fit is obtained assuming a plane in 3D L_R–L_X–L_K space, namely $\log L_R = \xi_X \log L_X + \xi_K \log L_K + \xi_0$, with a $\sim$1 dex wide (1σ) spread in radio luminosity. As already shown by La Franca, Melini & Fiore, no evidence of bimodality in the radio luminosity distribution was found and therefore any definition of radio-loudness in AGN is arbitrary. Using scaling relations between the black hole (BH) mass and the host galaxy K-band luminosity, we have also derived a new estimate of the BH fundamental plane (in $L_{5\,\mathrm{GHz}}$–L_X–M_{BH} space). Our analysis shows that previous measures of the BH fundamental plane are biased by $\sim$0.8 dex in favour of the most luminous radio sources. Therefore, many AGN studies, where the BH fundamental plane is used to investigate how AGN regulate their radiative and mechanical luminosity as a function of the accretion rate, and many AGN/galaxy co-evolution models, where radio feedback is computed using the AGN fundamental plane, should revise their conclusions.

Key words: methods: statistical – galaxies: active – radio continuum: galaxies – X-rays: galaxies.

1 INTRODUCTION

In recent years, in many galaxy formation models active galactic nuclei (AGN) are considered to be related to mechanisms capable of switching off star formation in the most massive galaxies, thus reproducing both the observed shape of the galaxy luminosity function and the red, early-type, passive evolving nature of local massive galaxies. It is expected that AGN and galaxy evolution are closely connected to each other (AGN/galaxy co-evolution) through feedback processes coupling both star formation and black hole (BH) accretion-rate histories. Some of these models assume that the AGN feedback into the host galaxy is due to the kinetic energy released by the radio jets and is, therefore, dependent on the AGN radio luminosity (Cattaneo et al. 2006; Croton et al. 2006; Marulli et al. 2008). Indeed, it has already been demonstrated that conversion of the AGN radio luminosity function into a kinetic luminosity function provides an adequate amount of energy (Best et al. 2006;

Körding, Jester & Fender 2008; Merloni & Heinz 2008; Shankar et al. 2008; Cattaneo & Best 2009; Smolčić et al. 2009; La Franca et al. 2010).

In this context, in order to build up more realistic AGN/galaxy co-evolutionary models, it is very useful to measure the dependence of the AGN core radio luminosity on other physical quantities related to AGN/galaxy evolutionary status, such as the BH and galaxy star masses and their time derivatives: accretion and star formation rates. These quantities can be measured either directly or indirectly.

A good estimate of galaxy star masses can be obtained by spectral energy distribution (SED) analyses in the optical and near-infrared (NIR) domains (see e.g. Merloni et al. 2010; Pozzi et al. 2012) or, still satisfactorily, from NIR (e.g. K-band) luminosity measures, as the mass-to-light ratio in the K band has a 1σ scatter of 0.1 dex (Madau, Pozzetti & Dickinson 1998; Bell et al. 2003).

BH masses can be estimated using reverberation mapping techniques or measuring the width of broad emission lines observed in optical and NIR spectra (the single-epoch method: see e.g. Vestergaard 2002). Less direct estimates are obtained using the scaling relations observed between the BH mass and the bulge or

⋆ E-mail: lafranca@fis.uniroma3.it

spheroid mass or between the BH mass and the bulge luminosity of the host galaxies (e.g. Dressler 1989; Kormendy & McClure 1993; Kormendy & Richstone 1995; Magorrian et al. 1998). In this framework even the total host galaxy K-band luminosity, if converted into the bulge luminosity, can be used as a good proxy of the BH mass (see e.g. Fiore et al. 2012).

The accretion rate, $\dot{m}$, is related to the AGN hard (>2 keV) X-ray luminosity, L_X, via knowledge of the X-ray bolometric correction, K_X, and the efficiency, ϵ, of conversion of mass accretion into radiation:

$$L_X = \frac{L_{bol}}{K_X} = \frac{\epsilon \dot{m} c^2}{(1-\epsilon) K_X}, \tag{1}$$

where L_{bol} is the bolometric luminosity and typical values for ϵ are about 0.1 (Marconi et al. 2004; Vasudevan & Fabian 2009).

The AGN radio luminosity distribution and its relationship to either the optical or X-ray luminosity have been studied by many authors. Some of these studies discussed the AGN radio luminosity in terms of a bimodal distribution where two separate populations of radio-loud and radio-quiet objects exist (e.g. Kellermann et al. 1989; Miller, Peacock & Mead 1990). Many other studies have alternatively measured a relationship between the radio and X-ray luminosities (e.g. Brinkmann et al. 2000; Terashima & Wilson 2003; Panessa et al. 2007; Bianchi et al. 2009; Singal et al. 2011). However, almost all these studies are based on incomplete samples due to the lack of deep radio observations. AGN samples selected in other bands (typically optical or X-ray) are therefore not fully detected in the radio band.

However, in order to study the AGN radio luminosity properties and their relation to X-ray and optical luminosities properly, it is necessary to use fully (or almost) radio-detected and complete AGN samples and, when needed, to take the radio upper limits properly into account. More recently, using deep radio observations, it has been shown that both AGN radio/optical and radio/X-ray luminosity ratios span more than five decades continuously (Best et al. 2005; La Franca et al. 2010; Singal et al. 2011; Baloković et al. 2012), without evidence of bimodal distributions, and it is therefore inaccurate to deal with the AGN radio properties in terms of two separate populations of radio-loud and radio-quiet objects. La Franca et al. (2010) used a sample of about 1600 hard X-ray (mostly 2–10 keV) selected AGN to measure (also taking into account the presence of censored radio data) the probability distribution function (PDF) of the ratio between the nuclear radio (1.4 GHz) and X-ray luminosity $R_X = \log[\nu L_\nu (1.4\,\text{GHz})/L_X(2\text{–}10\,\text{keV})]$ (see Terashima & Wilson 2003, for a discussion on the difference between the radio-to-optical and radio-to-X-ray ratio distributions in AGN). The probability distribution function of R_X was functionally fitted as dependent on the X-ray luminosity and redshift, $P(R_X|L_X, z)$. Measurement of the probability distribution function of R_X eventually allowed us to compute the AGN kinetic luminosity function and the kinetic energy density.

In this paper, using the same sample and a similar method to that used by La Franca et al. (2010), we describe the measure of dependence of the AGN radio core luminosity distribution, L_R, on both the X-ray (2–10 keV) luminosity L_X and the host galaxy (AGN-subtracted) K-band luminosity L_K. This measurement, in the context of the AGN/galaxy co-evolution scenario (see the discussion above), is vey useful in order to relate the kinetic (radio) feedback to the accretion rate (L_X) and the galaxy assembled star mass (L_K). In order to take the presence of censored data in the radio band accurately into account, an ad hoc Bayesian maximum likelihood

(ML) method and a three-dimensional Kolmogorov–Smirnov (KS) test have been developed.

Many authors have observed the existence of an analogous relationship between the radio luminosity, X-ray luminosity and black hole mass (M), the BH fundamental plane: namely, $\log L_R = \xi_{RX} \log L_X + \xi_{RM} \log M + \text{constant}$ (see Merloni, Heinz & di Matteo 2003; Falcke, Körding & Markoff 2004; Gültekin et al. 2009a). The measurement of such a relation is very useful in order to discriminate between several theoretical models of jet production in AGN, as it suggests that BH regulate their radiative and mechanical luminosity in the same way at any given accretion rate scaled to the Eddington one (Falcke & Biermann 1995; Heinz & Sunyaev 2003; Churazov et al. 2005; Laor & Behar 2008).

As relations have been observed between the BH mass and the K-band bulge luminosity (see discussion above), in Section 6 we convert our measure of the relation in $\log L_R$–$\log L_X$–$\log L_K$ space into a relation in $\log L_R$–$\log L_X$–$\log M$ space and discuss how important it is to take the presence of radio upper limits properly into account in order to measure the BH fundamental plane.

Unless otherwise stated, all quoted errors are at the 68 per cent confidence level. We assume $H_0 = 70$ km s^{-1} Mpc^{-1}, $\Omega_m = 0.3$ and $\Omega_\Lambda = 0.7$.

2   THE DATA

In our analysis we used the same data set used by La Franca et al. (2010), where radio (1.4-GHz) observations (either detections or upper limits) were collected for 1641 AGN (both type 1 (AGN1) and type 2 (AGN2), i.e. showing or not showing the broad-line region in their optical spectra) belonging to complete (i.e. with almost all redshift and N_H measures available) hard X-ray (>2 keV; mostly 2–10 keV) selected AGN samples,[1] with unabsorbed 2–10 keV luminosities larger than 10^{42} erg s^{-1}.

As the goal was to use the radio luminosity in order to estimate the kinetic luminosity, La Franca et al. (2010) measured radio emission that was, as much as possible, causally linked (contemporary) to the observed X-ray activity (accretion). Radio fluxes were measured in a region as close as possible to the AGN, therefore minimizing the contribution of objects like the radio lobes in Fanaroff–Riley type II (FR II) sources (Fanaroff & Riley 1974). For this reason they built up a large data set of X-ray-selected AGN (where redshift and N_H column densities estimates were available) observed at 1.4 GHz with $\sim$1 arcsec typical spatial resolution (1 arcsec corresponds, at maximum, to about 8 kpc at $z \sim 2$). The cross-correlation of the X-ray and radio catalogues was carried out inside a region with 5 arcsec radius (approximately less than or equal to the size of the central part of a galaxy like ours), following a maximum-likelihood algorithm as described by Sutherland & Saunders (1992) and Ciliegi et al. (2003). The offsets between the X-ray and radio positions of the whole sample resulted in a root-mean-square (rms) of 1.4 arcsec (similar to the typical values obtained in X-ray to optical cross-correlations, e.g. Cocchia et al. 2007).

In order to measure the K-band galaxy luminosity, the 1641 AGN from La Franca et al. (2010) have been cross-correlated with already existing K-band photometric catalogues, as explained below.

---

[1] Throughout this work we assumed that all the X-ray sources with 2–10 keV unabsorbed luminosities larger than 10^{42} erg s^{-1} are AGN. See e.g. Ranalli, Comastri & Setti (2003) for a study of the typical X-ray luminosities of star-forming galaxies.

2.1 The local sample: SWIFT and Grossan

At the lowest redshift we have used a sample of 33 AGN belonging to the 22-month SWIFT catalogue (Tueller et al. 2008). These AGN have been detected at high galactic latitude ($|b| > 15°$) in the 14–195 keV band with fluxes brighter than 10^{-11} erg s^{-1} cm^{-2}; all objects have N_H column density and optical spectroscopic classification available. The radio luminosity at 1.4 GHz has been derived using the Faint Image of the Radio Sky at Twenty Centimetres (FIRST) Very Large Array (VLA) survey (Becker, White & Helfand 1995). In the case of no radio detection, a 5σ upper limit of 0.75 mJy was adopted. The correlation between catalogues was made through the likelihood-ratio technique (Sutherland & Saunders 1992; Ciliegi et al. 2003). K_S magnitudes have been associated with the sources using the Two-Micron All-Sky Survey (2MASS) catalogue, which has a $\sim$14.3 mag completeness limiting magnitude (Skrutskie et al. 2006). Cross-correlation with the K-band data has been carried out by comparing the positions of the the 2MASS sources on the K-band image of the AGN counterpart.

To enlarge the local sample, La Franca et al. (2010) used the hard X-ray selected AGN catalogue detected by the *High-Energy Astronomy Observatory 1* (*HEAO-1*) mission (2–10 keV fluxes brighter than 2×10^{-11} erg s^{-1} cm^{-2}) described by Grossan (1992) and revised by Brusadin (2003). As for the SWIFT sample, these sources have been cross-correlated with the FIRST and 2MASS radio and K-band catalogues, respectively.

In summary, the local sample contains 43 X-ray sources, all with K_S band detection.

2.2 Hard Bright Sensitivity Survey

We have used the 32 AGN selected by the Hard Bright Sensitivity Survey (HBSS) of the *XMM–Newton* satellite, carried out at 4.5–7.5 keV fluxes brighter than 7×10^{-14} erg s^{-1} cm^{-2} (Della Ceca et al. 2008). K_S detections and upper limits were obtained for 19 and 13 sources, respectively, from the 2MASS catalogue. The cross-correlation was carried out using the same technique used for the local sample. Those sources missing a K_S detection were eventually excluded from the analysis.

2.3 The *ASCA* surveys: AMSS and ALSS

Two samples come from observations of the *Advanced Satellite for Cosmology and Astrophysics* (*ASCA*) satellite: the *ASCA* Medium Sensitivity Survey (AMSS: Akiyama et al. 2003), which is composed of 43 AGN, and the *ASCA* Large-Sky Survey (LASS: Ueda et al. 1999), which is composed of 30 AGN. For both of these catalogues we used the K_S photometric measures by Watanabe et al. (2004). Only one source (belonging to the AMSS) is missing a K_S detection.

2.4 COSMOS

The largest sample used in this work comes from X-ray observations of the field of the Cosmic Evolution Survey (COSMOS). The catalogue by Cappelluti et al. (2009) of *XMM–Newton* sources with 2–10 keV fluxes brighter than $\sim$3 $\times 10^{-15}$ erg s^{-1} cm^{-2} was used. K-band magnitudes for 648 out of 677 sources were taken from Brusa et al. (2010, and private communication).

2.5 *Chandra* Lockman Area North Survey

K-band photometry for 125 out of 139 AGN belonging to the *Chandra* Lockman Area North Survey (CLANS) were obtained from Trouille et al. (2008). The radio data come from Owen & Morrison (2008).

2.6 European Large Area *ISO* Survey

In the field S1 of the European Large Area *ISO* Survey (ELAIS-S1) we used the catalogue of X-ray sources detected using *XMM–Newton* by Puccetti et al. (2006), which reaches a 2–10 keV flux limit of 2×10^{-15} erg s^{-1} cm^{-2}. Radio data were taken from Middelberg et al. (2008), while spectroscopic and photometric identifications were taken from La Franca et al. (2004), Berta et al. (2006), Feruglio et al. (2008) and Sacchi et al. (2009). In Feruglio et al. (2008), K_S detections for 363 objects out of the 421 sources used by La Franca et al. (2010) are available.

2.7 Deep samples: *Chandra* Deep Field South and North

The deepest X-ray catalogues used in this work are those available in the *Chandra* Deep Field South (CDFS) and North (CDFN). These are subsamples of the Great Observatories Origins Deep Survey (GOODS) GOOD-S and GOOD-N multi-wavelength surveys with 2–10 keV flux limits of 2.6×10^{-16} erg s^{-1} cm^{-2} and 1.4×10^{-16} erg s^{-1} cm^{-2}, respectively.

In the CDFS we used 94 sources from the catalogue of Alexander et al. (2003) and identified by Brusa et al. (2010). These sources were correlated with radio data taken from Miller et al. (2008). K_S-band photometry was obtained using the deepest multi-wavelength catalogue (FIREWORKS) provided by Wuyts et al. (2008), which reaches $K_S \simeq 22.5$ mag. The K_S-band catalogue was cross-correlated with the optical catalogue using the likelihood-ratio technique. K_S-band counterparts for 86 out of 94 sources were found.

In the CDFN we used the X-ray catalogue from Alexander et al. (2003) with the identifications from Trouille et al. (2008). The sample consists of 162 extragalactic sources for which radio information was obtained from Biggs & Ivison (2006). Trouille et al. (2008) provided K_S-band detections for all but one of the sources.

In Table 1 the breakdown of all samples used is reported. Column 1 lists the original number N of sources contained in the samples used by La Franca et al. (2010), while column 2 lists the number of sources N_K having a K-band detection.

Table 1. Sample breakdown.

Sample	N (1) La Franca et al. (2010)	N_K (2) K detected	N_{K-GL} (3) K glx lum	N_R (4) Radio det
SWIFT	33	33	21	19
Grossan	10	10	0	0
HBSS	32	19	17	4
ALSS	30	30	19	4
AMSS	43	42	19	4
COSMOS	677	648	575	121
CLANS	139	125	91	52
ELAIS	421	363	283	37
CDF-S	94	86	85	12
CDF-N	162	161	158	40
Total	1641	1517	1268	293

3 *K*-BAND AGN AND GALAXY LUMINOSITIES

The *K*-band absolute magnitudes, M_K, have been computed by applying an empirical *K*-correction. We used the formula

$$M_K = m_K + 5 - 5 \log d_l(z) + 2.5(1 + \alpha) \log(1 + z), \qquad (2)$$

where $d_l(z)$ is the luminosity distance and the *K*-correction is represented by the α parameter. We used $\alpha = -0.86$ after comparison of our data with the COSMOS catalogue, where absolute *K*-band magnitudes have been accurately computed through SED fitting techniques (Bongiorno et al. 2012, and references therein).

In order to estimate the host galaxy *K*-band luminosities (i.e. the stellar component), we subtracted the AGN contribution from the measured total luminosities. For this purpose we used the nuclear (AGN-only) infrared SEDs, normalized to the hard X-ray (2–10 keV) intrinsic luminosity and averaged within bins of absorbing N_H as published by Silva, Maiolino & Granato (2004). These AGN SEDs were obtained through interpolation, using updated models from Granato & Danese (1994), of the nuclear infrared data of AGN taken from the Maiolino & Rieke (1995) sample. The accuracy of our method has been tested by comparing our estimates with those obtained by Merloni et al. (2010) and Bongiorno et al. (2012) for the COSMOS catalogue using SED decomposition fitting techniques. As shown in Fig. 1, our estimates, although less accurate, are in good agreement with those obtained by Merloni et al. (2010) and Bongiorno et al. (2012). The average difference that results is $\log L_K (\text{COSMOS}) - \log L_K (\text{us}) = -0.07(0.05)$ dex, with a 1σ spread of 0.30 (0.18) dex for AGN1 (AGN2).

In some cases we obtained that the expected AGN *K*-band luminosity was very close to (or even larger than) the total measured (AGN + host galaxy) luminosity. With the SED decomposition fitting techniques used by Merloni et al. (2010) and Bongiorno et al. (2012), no object could have an AGN luminosity larger than the total one (see also Pozzi et al. 2007, 2012). Bongiorno et al. (2012) conservatively decided that if the galaxy component were smaller than
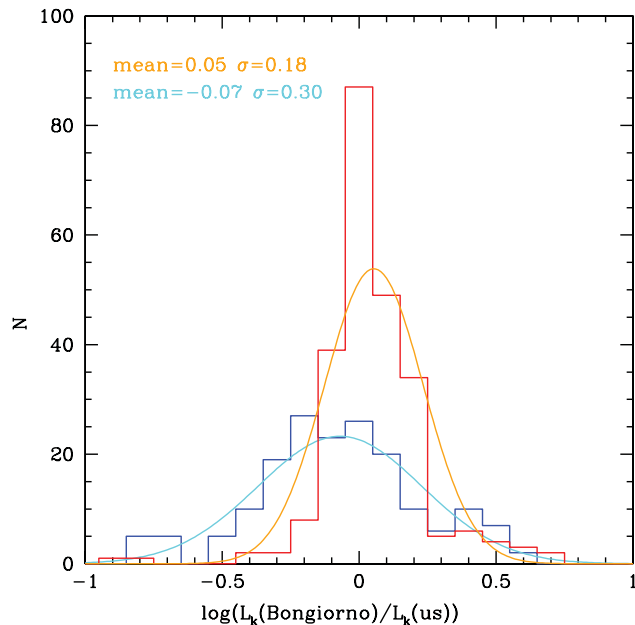

Figure 1. Histogram of the logarithmic differences between our estimates of the *K*-band luminosities of host galaxies (after AGN component subtraction; see text) in the COSMOS sample and the SED fitting measures from Bongiorno et al. (2012). AGN1 and AGN2 are shown by blue and red lines in the online article, respectively.
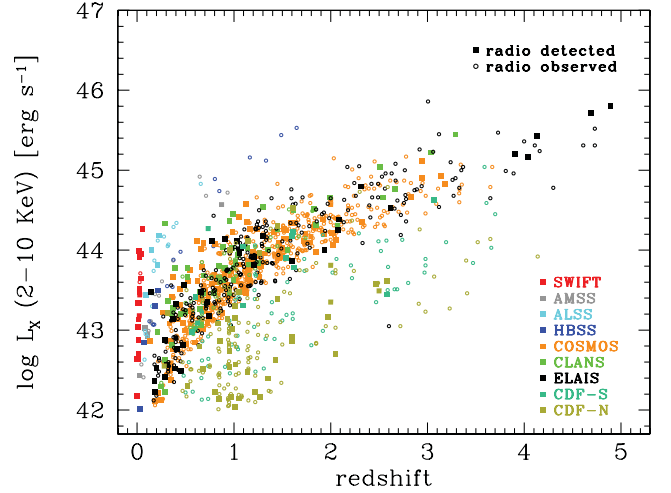

Figure 2. 2–10 keV de-absorbed luminosity, L_X, of the total sample as a function of redshift.

10 per cent of the total one then only an upper limit, corresponding to 10 per cent of the total luminosity, could be assigned. Following this approach, we decided to adopt a more conservative assumption and excluded from our analysis those 249 sources where the galaxy component that resulted was smaller than 20 per cent of the total one.[2]

In Table 1 we report in column 3 the number $N_{K-\text{GL}}$ of sources where it was possible to estimate the galaxy *K*-band luminosity.

4 THE WHOLE SAMPLE

In summary, our data set is composed of nine X-ray-selected AGN samples that contain a total of 1268 sources for which we were able to estimate the *K*-band stellar component luminosities of the host galaxy, L_K. For all these AGN, column densities and de-absorbed 2–10 keV luminosities, L_X, are available. The radio data allowed us to measure the 'nuclear' 1.4-GHz luminosity, L_R, for 293 sources while for the remaining sources 5σ radio upper limits (Table 1, column 4) are available. In total, this is the largest catalogue of AGN (both of type 1 and 2) belonging to statistically well-defined samples where radio, X and *K*-band information exists. The distribution of the whole AGN sample in the L_X–z plane is shown in Fig. 2, while in Figs 3 and 4 we show the 3D L_K–L_X–L_R distribution, projected on to the three 2D L_K–L_X, L_K–L_R and L_X–L_R planes, where L_K is shown before (L_K^{tot}) and after (L_K) the subtraction of the AGN component in the *K* band, respectively.

5 THE PLANE FITTING

5.1 Maximum-likelihood fitting method

We have used a maximum-likelihood fitting technique with a Bayesian approach in order to derive the probability distribution function of the AGN radio luminosity, L_R, as a function of L_X and the *K*-band stellar component luminosity, L_K, $P(L_R|L_X, L_K)$. The

[2] As described in Section 5, our 3D ML fitting method is able to deal with upper limits on one physical quantity only (the radio luminosity in our case). Therefore all sources where an upper limit on the *K*-band luminosity was available were excluded from our analysis (this happened to all the 10 sources of the Grossan sample).
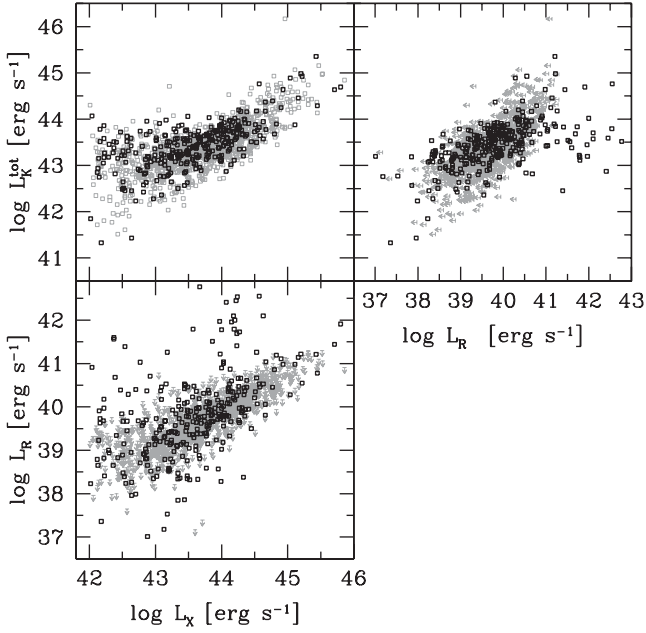
Figure 3. Distribution of the sample in the 2D L_K–L_X, L_K^{tot}–L_R and L_X–L_R planes, where L_K^{tot} is the total (galaxy + AGN) K-band luminosity. Squares represent the radio-detected sources while sources with a radio upper limit are shown by either grey arrows or grey squares (upper left panel).
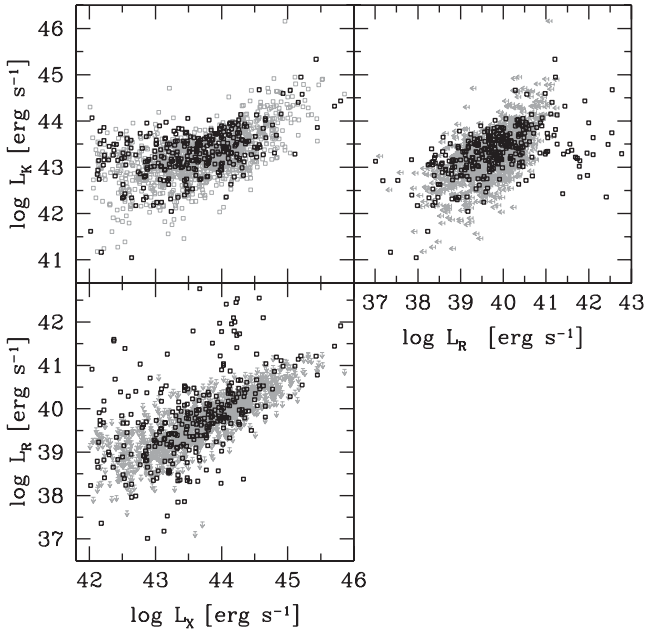

Figure 4. As in Fig. 3, with L_K representing the AGN-subtracted K-band galaxy luminosity.

maximum-likelihood fitting method does not need to use binning (e.g. as happens when using the χ^2 fitting method) and therefore the results do not depend on the arrangement of the binning pattern. In the usual maximum-likelihood fitting of luminosity function distributions $\rho(z, L)$ of extragalactic sources (e.g. Marshall et al. 1983), the best-fitting solution is obtained by minimizing the quantity $S = -2 \ln \mathcal{L}$ (where $\mathcal{L}$ is the likelihood and the S function follows the χ^2 statistic and therefore allows us to estimate the confidence interval of the best-fitting parameters: Lampton, Margon &

Bowyer 1976). The natural logarithm of the likelihood function is computed as follows:

$$\ln \mathcal{L} = \sum_i \ln[\rho(z_i, L_i)] - \int \rho(z, L)\Omega(z, L)\frac{dV}{dz} \, dL \, dz, \qquad (3)$$

where the sum is made over all i observed sources and $\Omega(z, L)$ is the sky coverage as a function of the luminosity L and redshift z. The first term is proportional to the combined probability (of independent events) of observing all i sources, each having redshift z_i and luminosity L_i, while the second term corresponds to the total number of expected sources in the sample and is, therefore, also used to constrain the normalization of the luminosity function.

In our case we have devised a new S function to be minimized which, following the same statistical principles as the maximum-likelihood method, is able to measure the conditional probability distribution function $P(L_R|L_X, L_K)$ (where $\int P(L_R|L_X, L_K) \, dL_R = 1$) of observing a radio luminosity L_R in an object having L_X and L_K luminosities. Our method has the advantage (in comparison with other three-dimensional fitting techniques) of also being able to take into account the occurrence of upper limits in one of the three dimensions. Indeed, as already discussed, in all samples the radio observations are not deep enough do detect all the sources (see Table 1) and therefore upper limits need to be considered in order to derive the true AGN radio luminosity distribution (see Plotkin et al. 2012, for an analogous Bayesian approach to this topic). For these reasons the natural logarithm of the likelihood function has been computed as follows:

$$\ln \mathcal{L} = \sum_i \ln P(L_{R_i}|L_{X_i}, L_{K_i})$$
$$- \sum_j \int_{L_R > L_{\lim_j}}^{\infty} P(L_R|L_{X_j}, L_{K_j}) \, dL_R. \qquad (4)$$

The first sum is computed for all i radio-detected sources and, as in equation (3), is proportional to the combined probability of observing the radio luminosities L_{R_i} of all i detected sources, while the second term is the sum of the probability of radio-detecting each j observed (either radio-detected or not) AGN, with a radio luminosity larger than its radio-detection limit $L_{\lim_j}$. In this case, analogously to the classical maximum-likelihood method (equation 3), this second term corresponds to the expected total number of radio-detected sources.

5.2 The 3D Kolmogorov–Smirnov test

Although the maximum-likelihood technique is very powerful in finding the parameters of the best-fitting solution and their uncertainties, it does not allow us to quantify how good the solution is. We have therefore devised a three-dimensional Kolmogorv–Smirnov (3D–KS) test able to measure the probability of observing the 3D distribution (in L_R–L_X–L_K space) of our sample of radio-detected sources under the null hypothesis that the data are drawn from the best-fitting model distribution.

The KS test is a standard statistical test for deciding whether a set of data is consistent with a given probability distribution. In one dimension the KS statistic is the maximum difference D between the cumulative distribution functions of the data and the model (or another sample). What makes the KS statistic useful is that its distribution (in the case of the null hypothesis that the data are drawn from the same distribution) can be calculated, giving the significance of any non-zero value of D.

Table 2. Best-fitting solutions.

Model	Function	ξ_X	ξ_K	ξ_0	Offset	σ_l[1]	σ_u	a	k	S	P_{KS}
1	Gaussian	0.313	0.683	38.684	0.00	0.974	...	...	...	1583	2 per cent
2	Double Gaussian	0.373	0.582	38.513	0.41	0.497	1.02	...	...	1571	3 per cent
3	Lorentz	0.379	0.705	39.374	−0.43	1.141	0.30	...	...	1515	26 per cent
4	Gaussian + exp	0.387	0.632	38.937	0.09	0.582	...	0.117	1.66	1504	35 per cent
4	68 per cent conf. errors	$^{+0.031}_{-0.059}$	$^{+0.066}_{-0.053}$	$^{+0.050}_{-0.032}$		$^{+0.028}_{-0.038}$		$^{+0.087}_{-0.021}$	$^{+0.24}_{-0.07}$		

[1]Corresponding to σ in those models with a single spread parameter.

In order to make a 3D–KS test, we have followed the examples of generalization of the KS test to two-dimensional distributions by Peacock (1983) and Fasano & Franceschini (1987). The maximum difference D statistic has been computed by measuring the difference between the fraction of observed and expected (by the model) sources in each of the eight octants defined at the 3D positions of each radio-detected source. In order to compute the number of expected sources, 2000 Monte Carlo simulations have been used. Although the 3D–KS test is carried out on the radio-detected sample only, it properly takes into account the effects of the radio upper limits. Indeed, the simulations have been carried by extracting a radio luminosity (or not) for each observed source by taking into account its radio-detection limits and the model conditional probability distribution function $P(L_R|L_X, L_K)$. The same 2000 simulations have been used to compute the probability (significance) of observing the measured maximum D statistic in the case of the null hypothesis that the data are drawn from the same distribution.

5.3 The fits

We have tried to fit the data assuming that the AGN radio luminosity, L_R, depends on average (i.e. with a spread in the radio luminosity axis) linearly on both the logarithmic X-ray and K-band (host galaxy) luminosities, drawing a plane in 3D $\log L_R$–$\log L_X$–$\log L_K$ space. As already discussed in the Introduction, this assumption is suggested by the observations made by many authors of the existence of a BH fundamental plane: a similar relationship between the radio luminosity, X-ray luminosity, and black hole mass (M), namely $\log L_R = \xi_{RX} \log L_X + \xi_{RM} \log M + \text{constant}$ (see Merloni et al. 2003; Gültekin et al. 2009a). The AGN radio luminosity dependence on $\log L_X$ and $\log L_K$ was modelled by the following relationship:

$$\log \bar{L}_R = \xi_X \log L_{X,44} + \xi_K \log L_{K,43} + \xi_0, \qquad (5)$$

where $\bar{L}_r$ is the luminosity of the peak (*mode*) of the probability distribution function of the spread, in erg s^{-1} units, and the luminosities have been normalized to $L_X = 10^{44}$ erg s^{-1} $L_{X, 44}$ and $L_K = 10^{43}$ erg s^{-1} $L_{K, 43}$.

This spread was first modelled by a Gaussian function, $G(X|0, \sigma)$, where $X = \log(L_R/\bar{L}_R)$, centred on $X = 0$ with standard deviation σ. The best-fitting parameters are shown in Table 2 (model 1). However, the 3D–KS statistic tells that there is only a 2 per cent probability that the observed distribution is drawn from the model. The probability distribution function of X is shown in Fig. 5. The data have been plotted comparing in each bin of X the number of observed (N_{obs}) and expected (N_{exp}; by the model) sources. This method (N_{obs} versus N_{exp} method) reproduces the observations and consequently takes properly into account both radio detections and upper limits (see e.g. La Franca et al. 1994; La Franca & Cristiani 1997; Matute et al. 2006, for similar applications). It is worth noting that this fit, although not satisfactory, gives an indication that the
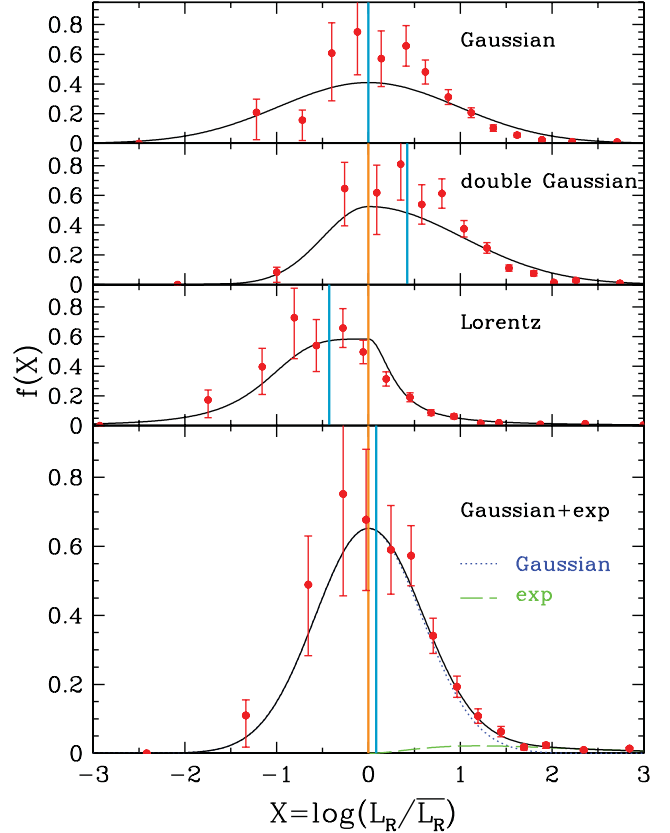

Figure 5. Probability distribution functions of $X = \log(L_R/\bar{L}_R)$, where $\bar{L}_r$ is the luminosity of the peak (*mode*) with the position shown by a vertical continuous line (orange in the online article). The four distributions correspond to the four best fits reported in Table 2. Other vertical lines (blue in the online article) show the values of the means of the distributions, the offsets from peak luminosity of which are reported in Table 2, and which are used in the next figures to represent the best-fitting solutions.

PDF of L_R is quite large: $\sigma \simeq 1$ dex, i.e. 68 per cent of cases are included in a 2-dex wide distribution. Similar results have been found by Merloni et al. (2003) and Gültekin et al. (2009a).

As shown in Fig. 5 (and already observed by La Franca et al. 2010), the data show an excess of high-radio-luminosity sources if compared with a symmetrical distribution. In order to take this excess better into account we have assumed an asymmetrical double Gaussian distribution with two σ values: σ_l and σ_u for radio luminosities values below (lower) and above (upper) the value of the radio luminosity, $\bar{L}_r$, of the peak of the probability distribution[3] (i.e. for X values above or below zero) respectively. Indeed, the fit

[3] Defined by equation (5).

gives a larger spread, $\sigma_u = 1.0$, at $X > 0$ than measured at $X < 0$, where $\sigma_1 = 0.5$. However, even with this model the 3D–KS test does not gives good enough probability (3 per cent). As the PDF is asymmetrical, we show in Fig. 5 the loci of both the peak and the mean of the PDF. A better representation of the model (e.g. in figures comparing the fit with the data) should, indeed, be carried out using the position of the mean of the distributions. The offsets between the mean and the mode (offset = mean - mode) of the PDF are also listed in column 4 of Table 2.

Better results are obtained if the spread is modelled as proposed by La Franca et al. (2010), assuming a double Lorentzian function described by the parameters σ_1 and σ_u:

$$P(X) = \begin{cases} \dfrac{N}{A\pi\sigma_l\left[1+\left(\frac{X}{\sigma_l}\right)^4\right]} & (X < 0), \\[4mm] \dfrac{A\,N}{\pi\sigma_u\left[1+\left(\frac{X}{\sigma_u}\right)^2\right]} & (X \geq 0), \end{cases} \qquad (6)$$

where, in order to obtain a continuous function at $X = 0$, $A = \sqrt{\sigma_u/\sigma_l}$ and the parameter N is constrained by the probability normalization requirement: $\int P(X)\,dX = 1$. In this case (see Fig. 5 and model 3 in Table 2) a 26 per cent 3D–KS probability is obtained.

An even better solution is obtained if, for $X > 0$, we add to a Gaussian distribution $G(X|0, \sigma)$ (as in model 1) an exponential function able to reproduce the high-radio-luminosity tail,

$$P(X) = \begin{cases} bG(X|0,\sigma) & (X < 0), \\ aX^2 e^{-kX} + bG(X|0,\sigma) & (X \geq 0), \end{cases} \qquad (7)$$

where the a and b parameters are not independent, as they are constrained by the probability normalization requirement:

$$b = 1 - \int_0^\infty aX^2 e^{-kX}\,dX. \qquad (8)$$

The best-fitting solution (model 4 in Table 2; also see Fig. 5) gives $b = 0.9499$, which implies that the added exponential tail at high radio luminosities represents about 5 per cent (1–0.9499) of the population (10 per cent for $X \geq 0$ where it is defined). In this case a 35 per cent 3D–KS probability is obtained. As already shown by La Franca et al. (2010), the radio luminosity distribution of the AGN does not show any evidence of a bimodal distribution and therefore any definition of radio loudness is arbitrary. None the less, it should be observed that (as demonstrated by these fits) the radio luminosity PDF is not symmetrical but skewed with a long tail at high radio luminosities. The introduction of this tail at $X > 0$ allows us to obtain a narrower ($\sigma \sim 0.6$ dex) complementary symmetrical Gaussian distribution. The position of the peak of the radio distribution of our best-fitting solution (number 4) is represented by the following equation:

$$\log \bar{L}_R = 0.39^{+.03}_{-.06} \log L_{X,44} + 0.63^{+.07}_{-.05} \log L_{K,43} + 39.94^{+.05}_{-.03}. \qquad (9)$$

Confidence regions for each parameter were obtained by minimizing the S function at a number of values around the best-fitting solution, while leaving the other parameters free to float (see Lampton et al. 1976). The 68 per cent confidence regions quoted correspond to $\Delta S (=\Delta\chi^2) = 1$. The best-fitting solution is also shown in Fig. 6, where the 3D distribution of the data is shown, and Fig. 7, where the 2D edge-on view of the plane is shown. This last figure helps us to understand how important it is to take into account the effects of using censored data. The fitting solution seems, indeed, not to be a good representation of the distribution of radio detections. This is because most of the X-ray samples have no radio
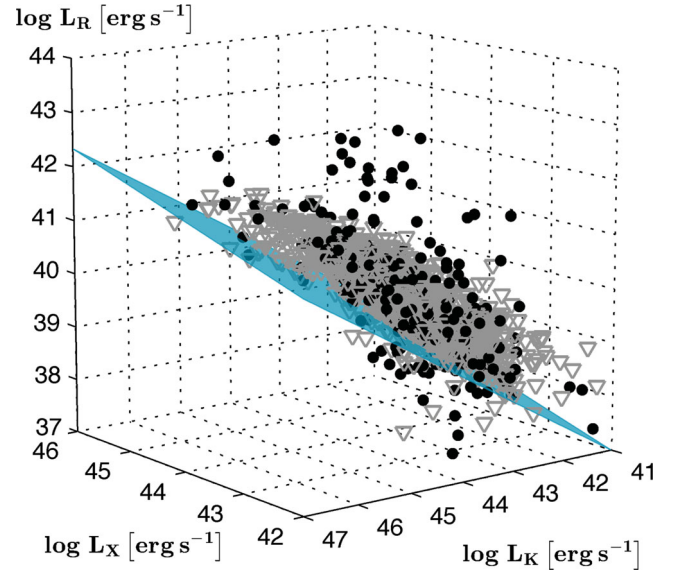

Figure 6. 3D distribution in L_R–L_X–L_K space. Filled circles represent radio detections and faint open triangles represent radio upper limits. The plane of the distribution of mean L_R as a function of L_X and L_K, according to the best-fitting solution (4) (Table 2), is shown.
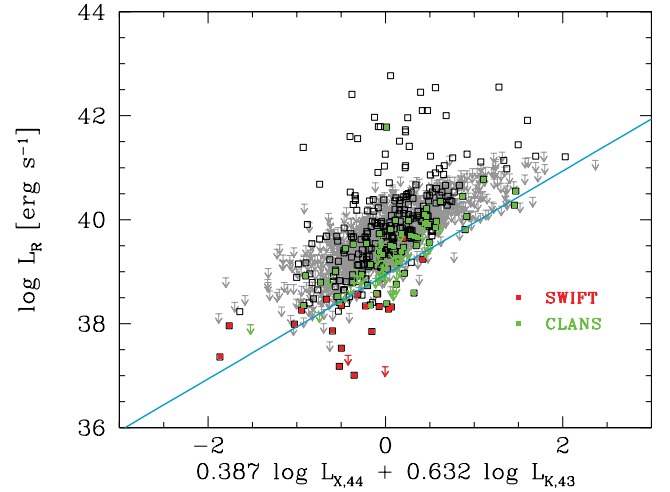

Figure 7. Edge-on view of the 3D plane. The more complete samples, SWIFT and CLANS, are represented by squares (red and green respectively in the online article). The continuous line shows the locus of the mean radio luminosity probability distribution function of our best-fitting solution (4) (Table 2). Radio upper limits are represented by arrows.

observations able to detect all sources and then the radio detections are biased in favour of the most luminous radio sources. Indeed, the mean radio luminosity of each of our samples decreases as a function of the radio identification completeness fraction: the average radio luminosity of the samples with about 10 per cent radio identifications is about $\log L_R = 40.0$ erg s^{-1}, while for the 90 per cent complete samples the average luminosity is about 2 dex lower ($\log L_R = 38.2$ erg s^{-1}; see Fig. 8). This bias is taken properly into account with our ML fitting method, which takes into account upper limits. The fitting solution, indeed, reproduces fairly well the distribution of the most radio-complete samples, such as SWIFT and CLANS (see Figs 7 and 9).
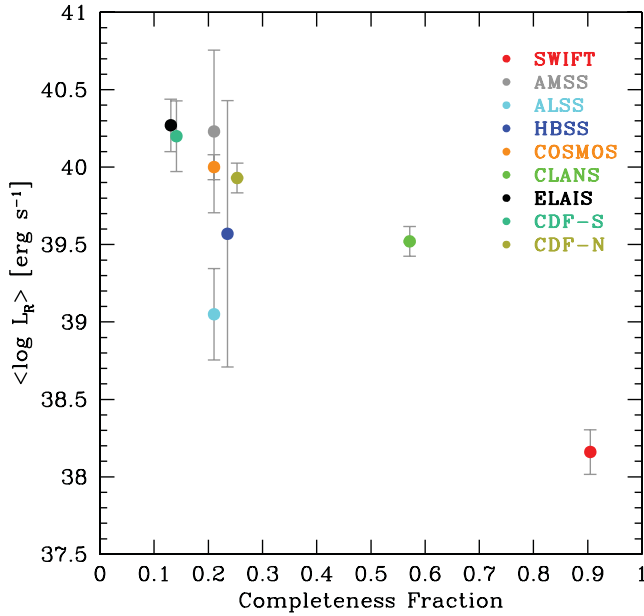
Figure 8. Mean radio luminosity of the radio-detected sources of each sample as a function of the radio-detection completeness.
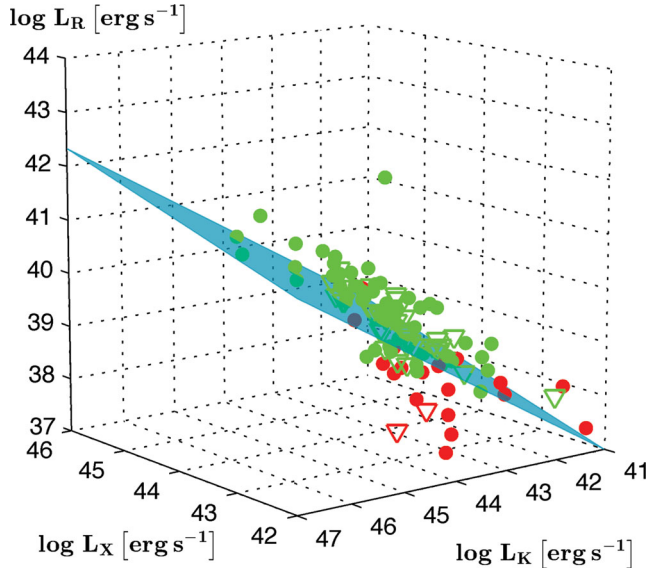

Figure 9. Same as Fig. 6 but using only the more radio-complete SWIFT (red circles in the online article) and CLANS (green circles in the online article) samples. Radio upper limits are represented by open triangles. The plane of distribution of the mean L_R as a function of L_X and L_K, according to the best-fitting solution (4), is shown.

6 THE AGN FUNDAMENTAL PLANE

Many authors have observed the existence of a BH fundamental plane relationship between the radio luminosity, X-ray luminosity and BH mass (see the discussion in the Introduction). As a relation has been observed between the BH mass and the bulge luminosity, it is interesting to study whether the BH fundamental plane measures are compatible or not with our measured relationship in the $\log L_R$–$\log L_X$–$\log L_K$ plane (we remember that L_K is the galaxy stellar-component luminosity). We have therefore estimated the BH masses

using the calibrated black hole versus K-band bulge luminosity relation from Graham (2007):

$$\log(M_{bh}/M_\odot) = -0.37(M_{K,bulge} + 24) + 8.29. \quad (10)$$

The bulge to total luminosity ratio (B/T) or bulge to disc ratio (B/D, where $B/T = [1 + D/B]^{-1}$) are functions of the galaxy type (see Dong & De Robertis 2006; Graham & Worley 2008). Therefore, in order to derive the bulge luminosities properly from our measures of the total galaxy luminosities it would be necessary to know the morphological type of our galaxies. Unfortunately this information is available only for a few tenths of galaxies belonging to the local sample (SWIFT), while for the higher redshift galaxies no information is available. Moreover, such kinds of relationships have been calibrated only using local samples, while it is well known that the average galaxy mass and morphology change with redshift (e.g. smaller and more clumpy galaxies occur with increasing redshift; Mosleh et al. 2012) and our sample reaches $z \sim 5$. However, our aim is not to measure the BH fundamental plane but only to verify how compatible our measure is with previous measures. According to Graham & Worley (2008), we have therefore assumed an average value of $B/T = 1/4$ in the K bandpass (see e.g. Fiore et al. 2012, for similar assumptions). Under this assumption, equation (10) corresponds to the relation

$$\log(M_{bh}/M_\odot) = 0.925 \log L_K - 31.781, \quad (11)$$

where L_K is the total (bulge plus disc) galaxy luminosity, expressed in erg s^{-1} units. We have compared our BH mass estimates with those reported by Merloni et al. (2010), which have been obtained via virial-based analysis of optical spectra of AGN1. On average, our estimates are larger by 0.14 dex in solar masses with a spread of 0.43 dex in solar mass units. This spread is compatible with the typical spreads ($\sim$0.3–0.4 dex) of the BH mass estimates based on both virial and scaling-relation methods (Gültekin et al. 2009b), the uncertainties in which, in our comparison, should both be taken into account in the propagation of errors.

According to equation (11), our best-fitting solution (4) is transformed in L_R–L_X–M_{BH} space into the relation

$$\log L_R = 0.39 \log L_X + 0.68 \log M_{BH} + 16.61, \quad (12)$$

while Merloni et al. (2003) measure

$$\log L_R = 0.60 \log L_X + 0.78 \log M_{BH} + 7.33, \quad (13)$$

where L_R here is the 5-GHz nuclear luminosity in units of erg s^{-1}, with 1.4-GHz radio luminosities converted into 5-GHz νL_ν luminosities assuming a radio spectral index $\alpha = 0.7$ (where $L_\nu \propto \nu^{-\alpha}$: Condon, Cotton & Broderick 2002), L_X is the 2–10 keV nuclear X-ray luminosity in units of erg s^{-1} and M_{BH} is the black hole mass in units of M$_\odot$ (Merloni et al. 2003).

7 DISCUSSION AND CONCLUSIONS

As expected (see Fig. 10), our estimate of the BH fundamental plane predicts lower radio luminosities if compared with the previous measure by Merloni et al. (2003). The typical difference, computed at 10^8 M$_\odot$ BH mass and 10^{44} erg s^{-1} X-ray luminosity, is $\sim$0.8 dex. As already observed in L_R–L_X–L_K space, this difference is due to the inclusion in our analysis of the contribution of the radio upper limits, and indeed our best-fitting solution reproduces well the distribution of the most radio-complete samples, such as SWIFT and CLANS (Figs 11 and 12).

It should be noted that the fundamental plane of Merloni et al. (2003) was constructed by including a sample of X-ray BH
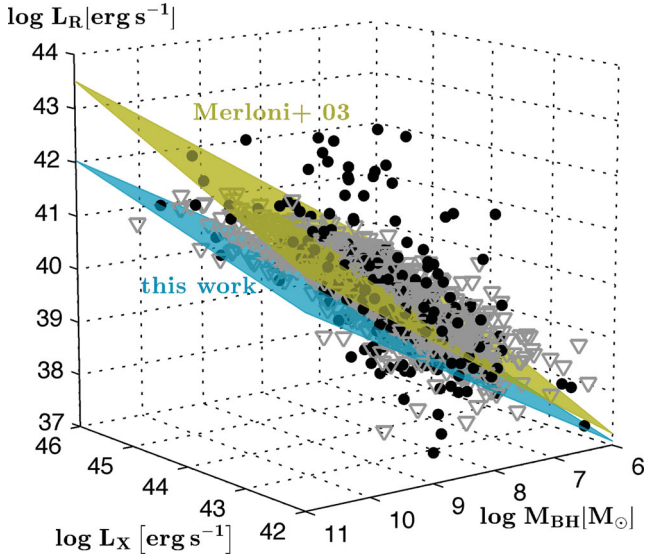
Figure 10. 3D distribution in L_R–L_X–M_{BH} space. The projection from L_R–L_X–L_K space of the plane of the best-fitting solution (4) is shown in cyan in the online article. The fundamental plane from Merloni et al. (2003) is shown in gold in the online article. Radio upper limits are represented by open triangles.
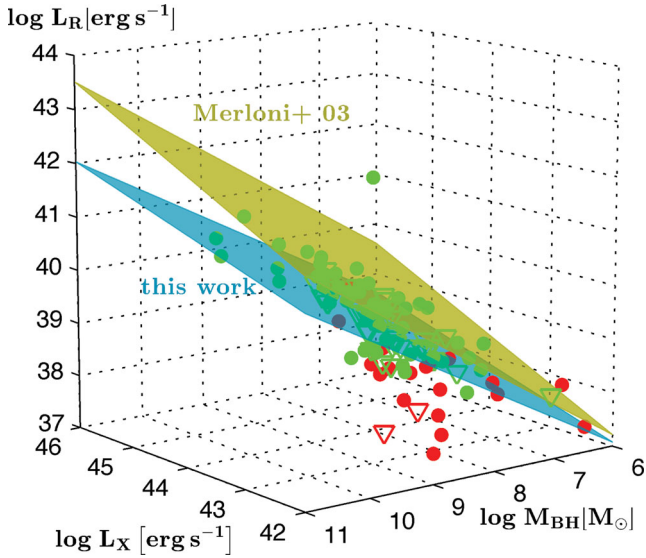

Figure 11. Same as Fig. 10 but using only the more radio-complete SWIFT (red circles in the online article) and CLANS (green circles in the online article) samples. Radio upper limits are represented by open triangles.

Figure 12. Edge on view of the BH fundamental plane as measured by Merloni et al. (2003) (dashed line, gold in the online article). The continuous line (cyan in the online article) shows our solution for a sample of AGN having average $\log M = 8.5$. The more complete samples, SWIFT and CLANS, are represented by squares (red and green respectively in the online article). Radio upper limits are represented by arrows.

study could suggest that in AGN a second, less radio-luminous population should also be taken into account, which could correspond to those objects with low values of the $X = \log(L_R/\bar{L}_R)$ parameter (see Fig. 5).

As already discussed in the Introduction, the measure of the dependence in AGN of L_R on other physical quantities such as L_X and the host galaxy K-band luminosity L_K is very useful in order better to include AGN in galaxy evolution models where AGN/galaxy feedback plays a relevant role.

Our analysis has allowed us to find a good analytical solution represented by a plane in 3D $\log L_R$–$\log L_X$–$\log L_K$ space once a wide ($1\sigma \sim 1$ dex) asymmetrical spread in the radio luminosity axis is included. This result confirms the study of La Franca et al. (2010) who, studying the dependence of PDFs of L_R on L_X and z, were able to model the 1-dex wide (1σ) spread in the AGN radio luminosity distribution. These results show that a proper study of the correlation between different band luminosities in AGN (or other sources) cannot be performed without taking into account censored data.

A clear example, in this framework, is the measure of the BH fundamental plane in 3D $\log L_R$–$\log L_X$–$\log M$ space. After converting our measures of the host galaxy K-band luminosity into BH masses using scaling relations, our best-fitting solution corresponds to a BH fundamental plane that on average predicts 0.8 dex lower values for the AGN radio luminosities.

It should be pointed out that, at variance with many similar statistical studies, our analysis is based on a compilation of complete, hard X-ray selected AGN samples, where both AGN1 and AGN2 are included. Therefore, our results should better represent the behaviour of the whole AGN population. However, it will be interesting to check the 3D correlation between L_R, L_X and L_K in complete, *radio-selected* samples. As the Merloni et al. (2003) sample was a hybrid sample without a clear selection criterion, it is plausible that some of the differences found in the present work could be due to the specific selection criterion. In very general terms, if we do not believe we know any of the three terms (X-ray luminosity,

binaries. While it is interesting to see that the mass scaling is still broadly consistent with that of Merloni et al. (2003) even in our study of an AGN-only sample, the radio–X-ray coefficient is very different: $\sim$0.4 in this study, while low-accretion-rate (and low-luminosity) X-ray BH binaries show a tight radio–X-ray correlation with slope $\sim$0.6. Interestingly enough, recent reanalysis of radio–X-ray correlations in X-ray binaries suggest the presence of a second, less radio-luminous branch (Gallo, Fender & Pooley 2003; Coriat et al. 2011; Gallo, Miller & Fender 2012). In this framework, our
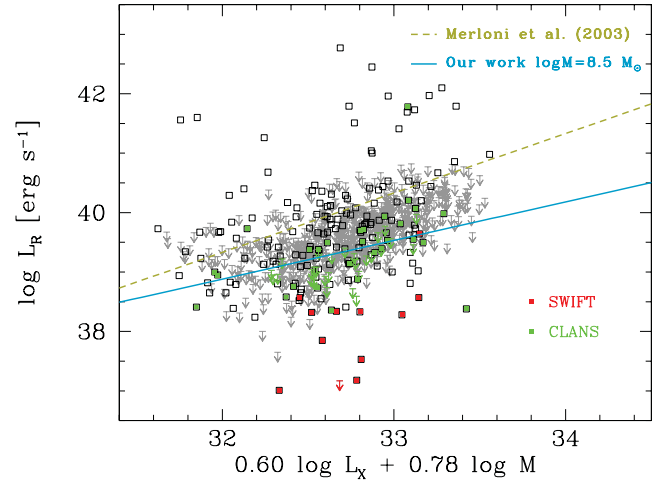
radio luminosity and BH mass) to be the primary physical driver, all should be treated as equal in a correlation study (but this is beyond the purpose of this paper).

In order to improve these analyses, it would be very useful to obtain deeper radio observations of complete samples of AGN combined with detailed optical–NIR–MIR SED observations. These data, when available, will eventually allow us to measure the dependence of the radio luminosity distribution (i.e. the feedback) on star and BH masses, their derivatives (star formation and accretion rates) and redshift. This result could be achieved by complementing multiwavelength surveys with observations carried out with new radio facilities such as the Expanded Very Large Array and the Square Kilometer Array.

ACKNOWLEDGMENTS

NOTE ADDED IN PRESS

It is brought to our attention that, after the submission of this paper, a new relationship between the BH mass and K-band bulge luminosity has been published by Graham & Scott (2012). After a quick analysis, we expect that, using this new relationship, our fundamental plane estimate would be tilted such as that the distance from the plane of Merloni, Heinz & Di Matteo (2003) will remain of about 0.8 dex for $\log M_{BH}$ 8, while it will increase at larger BH masses and decrease at smaller BH masses.

REFERENCES

Akiyama M., Ueda Y., Ohta K., Takahashi T., Yamada T., 2003, ApJS, 148, 275
Alexander D. M. et al., 2003, AJ, 126, 539
Baloković M., Smolčić V., Ivezić Ž., Zamorani G., Schinnerer E., Kelly B. C., 2012, ApJ, 759, 30
Becker R. H., White R. L., Helfand D. J., 1995, ApJ, 450, 559
Bell E. F., McIntosh D. H., Katz N., Weinberg M. D., 2003, ApJS, 149, 289
Berta S. et al., 2006, A&A, 451, 881
Best P. N., Kauffmann G., Heckman T. M., Brinchmann J., Charlot S., Ivezić Ž., White S. D. M., 2005, MNRAS, 362, 25
Best P. N., Kaiser C. R., Heckman T. M., Kauffmann G., 2006, MNRAS, 368, L67
Bianchi S., Bonilla N. F., Guainazzi M., Matt G., Ponti G., 2009, A&A, 501, 915
Biggs A. D., Ivison R. J., 2006, MNRAS, 371, 963
Bongiorno A. et al., 2012, MNRAS, 427, 3103
Brinkmann W., Laurent-Muehleisen S. A., Voges W., Siebert J., Becker R. H., Brotherton M. S., White R. L., Gregg M. D., 2000, A&A, 356, 445
Brusa M. et al., 2010, ApJ, 716, 348
Brusadin V., 2003, PhD Thesis, Univ. Roma Tre

Cappelluti N. et al., 2009, A&A, 497, 635
Cattaneo A., Best P. N., 2009, MNRAS, 395, 518
Cattaneo A., Dekel A., Devriendt J., Guiderdoni B., Blaizot J., 2006, MNRAS, 370, 1651
Churazov E., Sazonov S., Sunyaev R., Forman W., Jones C., Böhringer H., 2005, MNRAS, 363, L91
Ciliegi P., Zamorani G., Hasinger G., Lehmann I., Szokoly G., Wilson G., 2003, A&A, 398, 901
Cocchia F. et al., 2007, A&A, 466, 31
Condon J. J., Cotton W. D., Broderick J. J., 2002, AJ, 124, 675
Coriat M. et al., 2011, MNRAS, 414, 677
Croton D. J. et al., 2006, MNRAS, 365, 11
Della Ceca R. et al., 2008, A&A, 487, 119
Dong X. Y., De Robertis M. M., 2006, AJ, 131, 1236
Dressler A., 1989, in Osterbrock D. E., Miller J. S., eds, IAU Symp. Vol. 134, Active Galactic Nuclei. Kluwer, Dordrecht, p. 217
Falcke H., Biermann P. L., 1995, A&A, 293, 665
Falcke H., Körding E., Markoff S., 2004, A&A, 414, 895
Fanaroff B. L., Riley J. M., 1974, MNRAS, 167, 31P
Fasano G., Franceschini A., 1987, MNRAS, 225, 155
Feruglio C. et al., 2008, A&A, 488, 417
Fiore F. et al., 2012, A&A, 537, A16
Gallo E., Fender R. P., Pooley G. G., 2003, MNRAS, 344, 60
Gallo E., Miller B. P., Fender R., 2012, MNRAS, 423, 590
Graham A. W., 2007, MNRAS, 379, 711
Graham A. W., Worley C. C., 2008, MNRAS, 388, 1708
Graham A. W., Scott N., 2012, ApJ, in press (arXiv:1211.3199)
Granato G. L., Danese L., 1994, MNRAS, 268, 235
Grossan B. A., 1992, PhD thesis, Massachusetts Institute of Technology, Cambridge, MA, USA
Gültekin K., Cackett E. M., Miller J. M., Di Matteo T., Markoff S., Richstone D. O., 2009a, ApJ, 706, 404
Gültekin K. et al., 2009b, ApJ, 698, 198
Heinz S., Sunyaev R. A., 2003, MNRAS, 343, L59
Kellermann K. I., Sramek R., Schmidt M., Shaffer D. B., Green R., 1989, AJ, 98, 1195
Körding E. G., Jester S., Fender R., 2008, MNRAS, 383, 277
Kormendy J., McClure R. D., 1993, AJ, 105, 1793
Kormendy J., Richstone D., 1995, ARA&A, 33, 581
La Franca F., Cristiani S., 1997, AJ, 113, 1517
La Franca F., Gregorini L., Cristiani S., de Ruiter H., Owen F., 1994, AJ, 108, 1548
La Franca F. et al., 2004, AJ, 127, 3075
La Franca F., Melini G., Fiore F., 2010, ApJ, 718, 368
Lampton M., Margon B., Bowyer S., 1976, ApJ, 208, 177
Laor A., Behar E., 2008, MNRAS, 390, 847
Madau P., Pozzetti L., Dickinson M., 1998, ApJ, 498, 106
Magorrian J. et al., 1998, AJ, 115, 2285
Maiolino R., Rieke G. H., 1995, ApJ, 454, 95
Marconi A., Risaliti G., Gilli R., Hunt L. K., Maiolino R., Salvati M., 2004, MNRAS, 351, 169
Marshall H. L., Tananbaum H., Avni Y., Zamorani G., 1983, ApJ, 269, 35
Marulli F., Bonoli S., Branchini E., Moscardini L., Springel V., 2008, MNRAS, 385, 1846
Matute I., La Franca F., Pozzi F., Gruppioni C., Lari C., Zamorani G., 2006, A&A, 451, 443
Merloni A., Heinz S., 2008, MNRAS, 388, 1011
Merloni A., Heinz S., Di Matteo T., 2003, MNRAS, 345, 1057
Merloni A. et al., 2010, ApJ, 708, 137
Middelberg E. et al., 2008, AJ, 135, 1276
Miller L., Peacock J. A., Mead A. R. G., 1990, MNRAS, 244, 207
Miller N. A., Fomalont E. B., Kellermann K. I., Mainieri V., Norman C., Padovani P., Rosati P., Tozzi P., 2008, ApJS, 179, 114
Mosleh M. et al., 2012, ApJ, 756, L12
Owen F. N., Morrison G. E., 2008, AJ, 136, 1889
Panessa F., Barcons X., Bassani L., Cappi M., Carrera F. J., Ho L. C., Pellegrini S., 2007, A&A, 467, 519
Peacock J. A., 1983, MNRAS, 202, 615

Plotkin R. M., Markoff S., Kelly B. C., Körding E., Anderson S. F., 2012, MNRAS, 419, 267

Pozzi F. et al., 2007, A&A, 468, 603

Pozzi F. et al., 2012, MNRAS, 423, 1909

Puccetti S. et al., 2006, A&A, 457, 501

Ranalli P., Comastri A., Setti G., 2003, A&A, 399, 39

Sacchi N. et al., 2009, ApJ, 703, 1778

Shankar F., Cavaliere A., Cirasuolo M., Maraschi L., 2008, ApJ, 676, 131

Silva L., Maiolino R., Granato G. L., 2004, MNRAS, 355, 973

Singal J., Petrosian V., Lawrence A., Stawarz Ł., 2011, ApJ, 743, 104

Skrutskie M. F. et al., 2006, AJ, 131, 1163

Smolčić V. et al., 2009, ApJ, 696, 24

Sutherland W., Saunders W., 1992, MNRAS, 259, 413

Terashima Y., Wilson A. S., 2003, ApJ, 583, 145

Trouille L., Barger A. J., Cowie L. L., Yang Y., Mushotzky R. F., 2008, ApJS, 179, 1

Tueller J., Mushotzky R. F., Barthelmy S., Cannizzo J. K., Gehrels N., Markwardt C. B., Skinner G. K., Winter L. M., 2008, ApJ, 681, 113

Ueda Y. et al., 1999, ApJ, 518, 656

Vasudevan R. V., Fabian A. C., 2009, MNRAS, 392, 1124

Vestergaard M., 2002, ApJ, 571, 733

Watanabe C., Ohta K., Akiyama M., Ueda Y., 2004, ApJ, 610, 128

Wuyts S., Labbé I., Schreiber N. M. F., Franx M., Rudnick G., Brammer G. B., van Dokkum P. G., 2008, ApJ, 682, 985

This paper has been typeset from a TEX/LATEX file prepared by the author.

Appendix B

Proposals

In this Appendix the various successful observing proposals in which I have been involved are listed. These topics are not strictly related to the main project on which I worked during my Ph.D. thesis.

Application for LBT observing time   Category: A

1. Title

The evolution of the $M_{BH} - M_{star}$ relation in obscured AGNs at high redshift

2. Abstract

High redshift *unobscured* AGNs are found to have black hole-to-stellar mass ratios (M_{BH}/M_{star}) higher than in local galaxies, implying that black holes form faster than their host galaxies. Cosmological models ascribe this effect to the enhanced galaxy merging rate at early epochs, which boosts black hole accretion much more than star formation. Within this scenario *obscured* AGNs at high redshift should have either the same M_{BH}/M_{star} ratio as unobscured AGNs (strict unified model), or even higher M_{BH}/M_{star}, since such models expect obscured AGNs to be in an earlier evolutionary phase. However, we have recently determined the M_{BH}/M_{star} ratios in three *obscured* AGNs at z∼1–2 and found that they are in agreement with the ratio observed in local galaxies (and lower than observed in unobscured AGNs). If confirmed, our result would imply a major revision of cosmological models of BH-galaxy coevolution. However, our result is still tentative, since based only on three obscured AGNs at high-z. We propose LUCIFER MOS observations of a much larger sample of ∼50 high-z obscured AGNs with the aim of detecting their broad Hα, to estimate their BH masses through the virial methods and, therefore, locate them on the $M_{BH} - M_{star}$ diagram at high-z.

3a. Number of requested hours per telescope and instrument

LBT	
LBC Binocular	**LUCIFER**
	22

4. Temporal Scheduling Constraints

4b. Soft TOO ☐   **4c. Hard TOO** ☐

5a. Past and future of the project

a) Hours already awarded to the project:

b) Hours foreseen to complete the project:
   (not including this request)

6. Principal investigator

Name Roberto Maiolino

Institute INAF - Osservatorio Astronomico di Roma

Address via di Frascati 33, 00040, Monte Porzio Catone

e-mail roberto.maioilno@oa-roma.inaf.it

Phone 06 94286428

7. Co-investigators (name and institution)

E. Sarria - Univ. Roma III
F. La Franca - Univ. Roma III
F. Fiore - OAR
A. Marconi - Univ. Firenze
M. Elvis - CfA
F. Civano - CfA
A. Comastri - OAB
F. Pozzi - OAB
C. Vignali - Univ. Bologna
M. Brusa - MPE
A. Merloni - MPE
M. Salvato - MPE

o q

INAF – TIME ALLOCATION COMMITTEE

Application for observing time   **Category: A**

Period AOT23 (Feb11-Jul11)   **Deadline: October 15th, 2010**   **Submit using: www.tng.iac.es/submit.html**

---

1. Title

Spectroscopic identification of elusive, highly obscured, type 2 QSOs

---

2. Abstract

Recent works have suggested that selection criteria based on mid-IR properties, i.e. extreme colors and bright flux levels, can be used to reveal a population of dust-enshrouded, extremely-luminous quasars at $z \sim$1–2. These objects are believed to belong to a still missing (but predicted) population of highly obscured (and X-ray absorbed) AGN, possibly linked to a key early phase of massive galaxies/quasars co-evolution.

Using data coming from the Spitzer Wide-area Infrared Extragalactic Survey (SWIRE) and XMM and Chandra telescopes, we have selected a sample of candidate highly obscured AGNs having $F_{24\mu m}/F_R$ ratios >2000. Here we request to carry out NICS+Amici spectroscopy in order to measure the redshift and confirm the AGN nature of 9 of these candidates.

The good effectiveness of this method has been recently tested by us at VLT (Sacchi et al. 2009) and SUBARU (Lanzuisi et al. 2009) on few ($\sim$10) objects.

3a. Number of requested hours per telescope and instrument

TNG					REM	
DOLORES	**DOLOR.+MOS**	**SARG**	**NICS**	**Visitor Instr.**	**ROSS**	**REMIR**
			8			

3b. Observing modes   **TNG:**

	Visitor	**X**	Queuing		ToO

REM:

	Rapid Response		Queuing		ToO

4a. Preferred months

   first choice: April   second choice: March

4b. Other scheduling constraints (use also box 14)

5a. Past and future of the project

a) Hours already awarded to the project: 0

b) Hours foreseen to complete the project: 0
   (not including this request)

5b. Long Term ☐   **5c. Very Large Program** ☐

---

6. Principal investigator

Name   Fabio La Franca

Institute   Università degli Studi Roma Tre

Address   Via della Vasca Navale 84, 00146, Roma

e-mail   lafranca@fis.uniroma3.it

Phone   +39 06 5733 7038

7. Co-investigators (name and institution)

F. Fiore – INAF/OAR
R. Maiolino – INAF/OAR
G. Lanzuisi – INAF/OAR
E. Piconcelli – INAF/OAR
G. Melini – Univ. Roma Tre
C. Vignali – Univ. Bologna
C. Gruppioni – INAF/OABo

EUROPEAN SOUTHERN OBSERVATORY

Organisation Européenne pour des Recherches Astronomiques dans l'Hémisphère Austral
Europäische Organisation für astronomische Forschung in der südlichen Hemisphäre

APPLICATION FOR OBSERVING TIME	PERIOD: **88A**

Important Notice:

By submitting this proposal, the PI takes full responsibility for the content of the proposal, in particular with regard to the names of CoIs and the agreement to act according to the ESO policy and regulations, should observing time be granted

---

1. Title   Category: **A–1**

The First Direct Measure of the Complete (AGN1+AGN2) Local Black Hole Mass Function of the AGN

---

2. Abstract / Total Time Requested

Total Amount of Time: 0 nights VM, 25 hours SM

While the AGN (hard X-ray) luminosity function is fairly well known up to $z \sim 4$, we have no reliable measures of the AGN (AGN1 & AGN2) Super Massive BH Mass Function (SMBHMF). Previous studies have derived the SMBHMF by using, in the optical band, virial based techniques on samples of broad line AGNs (AGN1). But these measures are all biased against AGN2 where the BLR is not visible in the optical. There is growing observational evidence that AGN1 and AGN2 have on average different luminosities and hosting galaxies, and then probably different masses. We propose to measure the BH masses of all 35 AGN2 from the (very complete) 22-month AGN SWIFT/BAT sample with $0<\alpha<12$ and $\delta<10$. We will use the new virial based methods available in the NIR, by detecting the broad components in the Paβ and Paα hydrogen lines. Our deep proposed observations should have a success rate higher than 50% in detecting these broad components.

3.

Run	Period	Instrument	Time	Month	Moon	Seeing	Sky	Mode	Type
A	88	ISAAC	25h	dec	n	1.0	CLR	s	
A/alt	88	SINFONI	20h	dec	n	1.0	CLR	s	

---

4. Number of nights/hours   Telescope(s)   Amount of time

a) already awarded to this project:

b) still required to complete this project: UT3   25h

---

5. Special remarks:

---

6. Principal Investigator: Fabio La Franca, lafranca@fis.uniroma3.it, I, Universita Roma Tre,Dipartimento di Fisica

---

6a. Co-investigators:

F.	Fiore	INAF - Osservatorio Astronomico di Roma,I
R.	Maiolino	INAF - Osservatorio Astronomico di Roma,I
A.	Marconi	Universita di Firenze,Dipartimento di Astronomia e Scienza dello Spazio,I
C.	Vignali	Universita di Bologna, Dipartimento di Astronomia,I

Following CoIs moved to the end of the document ...

---

7. Is this proposal linked to a PhD thesis preparation? State role of PhD student in this project

Yes   /   G. Melini. Data important for PhD thesis   /   mid-course

Application for observing time   **Category: A**

1. Title

The First Direct Measure of the Complete (AGN1+AGN2) Local Black Hole Mass Function of the AGN

2. Abstract

While the AGN (hard X-ray) luminosity function is fairly well known up to $z \sim 4$, we have no reliable measures of the AGN (AGN1 & AGN2) Super Massive BH Mass Function (SMBHMF). Previous studies have derived the SMBHMF by using, in the optical band, virial based techniques on samples of broad line AGNs (AGN1). But these measures are all biased against AGN2 where the BLR is not visible in the optical. There is growing observational evidence that AGN1 and AGN2 have on average different luminosities and hosting galaxies, and then probably different masses. We propose to measure the BH masses of all 37 AGN2 from the (very complete) 22-month AGN SWIFT/BAT sample with $22 < \alpha < 10$ and $\delta > -10$. We will use the new virial based methods available in the NIR, by detecting the broad components in the Paβ and Paα hydrogen lines. Our deep proposed observations should have a success rate higher than 50% in detecting these broad components.

3a. Number of requested hours per telescope and instrument

TNG					REM	
DOLORES	**DOLOR.+MOS**	**SARG**	**NICS**	**Visitor Instr.**	**ROSS**	**REMIR**
			25			

3b. Observing modes

TNG:	**Visitor**	**X**	**Queuing**		**ToO**	
REM:	**Rapid Response**		**Queuing**		**ToO**	

4a. Preferred months

first choice: oct   second choice: nov

4b. Other scheduling constraints (use also box 14)

5a. Past and future of the project

a) Hours already awarded to the project: 0

b) Hours foreseen to complete the project: 25
(not including this request)

5b. Long Term ☐   **5c. Very Large Program** ☐

6. Principal investigator

Name Fabio LA FRANCA

Institute Dip.di Fisica, Univ. Roma Tre

Address Via della Vasca Navale 84

e-mail lafranca@fis.uniroma3.it

Phone 06 5733 7038

7. Co-investigators (name and institution)

F. Fiore — INAF/OAR
R. Maiolino — INAF/OAR
A. Marconi — Univ. Firenze
C. Vignali — Univ. Bologna
M. Brusa — MPE/Munich
A. Bongiorno — INAF/OAR
A. Antonelli — INAF/OAR
S. Bianchi — Univ. Roma Tre
G. Melini — Univ. Roma Tre

Application for LBT observing time **Category: B**

Period Sep 2012-Jun 2013   Deadline: May 18th, 2012, 2pm CEST   Submit using: www.tng.iac.es/lbt/submit.html

---

1. Title **Strategic Program** ☐

The First Direct Measure of the Complete (AGN1+AGN2) Local Black Hole Mass Function of AGN

---

2. Abstract

While the AGN (hard X-ray) luminosity function is fairly well known up to $z \sim 4$, we have no reliable measures of the AGN (AGN1 & AGN2) Super Massive BH Mass Function (SMBHMF). Previous studies have derived the SMBHMF by using, in the optical band, virial based techniques on samples of broad line AGNs (AGN1). But these measures are all biased against AGN2 where the Broad Line Region (BLR) is not visible in the optical. There is growing observational evidence that AGN1 and AGN2 have on average different luminosities and hosting galaxies, and then probably different masses. We propose to measure the BH masses of a subsample of 12 AGN2 randomly selected from the (very complete) 22-month AGN SWIFT/BAT sample. We will use the new virial based methods available in the NIR, by detecting the hidden broad components in the Paα1.875 and Paβ1.282 and HeI1.083 lines. According to the very preliminary analysis of our ISAAC/VLT P88 observations of 23 AGN2, we should have a success rate higher than $\sim 40\%$ in detecting the BLR component. The full (LBT+VLT) sample will allow us to reach the statistical significance needed to verify wether the AGN2 SMBHMF is different than that of AGN1.

---

3. Number of requested hours per instrument

LBC	LUCI1	MODS1
	13.6	

---

4. Principal investigator

Name Fabio LA FRANCA

Institute Dip.di Fisica, Univ. Roma Tre

Address Via della Vasca Navale 84

e-mail lafranca@fis.uniroma3.it

Phone 06 5733 7038

5. Co-investigators (name and institution)

F. Fiore — INAF/OAR
R. Maiolino — Univ. Cambridge
A. Marconi — Univ. Firenze
C. Vignali — Univ. Bologna
M. Brusa — MPE/Munich
A. Bongiorno — INAF/OAR
A. Antonelli — INAF/OAR
S. Bianchi — Univ. Roma Tre
G. Melini — Univ. Roma Tre
F. Onori — Univ. Roma Tre.

Appendix C

Cosmology

In the following Sections some hints on the cosmographic parameters and distance measures in cosmology are given. This treatment has been adopted from Hogg (1999).

C.1   Cosmographic parameters

The *Hubble constant* H_0 is the constant of proportionality between the recession speed v and the distance d in the expanding universe:

$$v = H_0 d, \qquad\qquad (\text{C.1})$$

where the subscripted "0" is referred to the present epoch, as the Hubble constant H varies with time. Although H_0 has the dimensions of an inverse time, it is usually written as:

$$H_0 = 100h \text{ km s}^{-1} \text{ Mpc}^{-3}, \qquad\qquad (\text{C.2})$$

where h is in the range $0.6 - 0.9$. The inverse of the Hubble constant is the *Hubble time* t_H:

$$t_H = \frac{1}{H_0} = 9.78 \times 10^9 h^{-1} \text{ yr} = 3.09 \times 10^{17} h^{-1} \text{ s}, \qquad (\text{C.3})$$

and the speed of light c times the Hubble time is defined as the *Hubble distance D_{H}*:

$$D_{\mathrm{H}} = \frac{c}{H_0} = 3000 h^{-1} \text{ Mpc} = 9.26 \times 10^{25} h^{-1} \text{ m}. \tag{C.4}$$

These three quantities set the scale of the Universe. The mass density ρ and the value of the cosmological constant Λ are instead dynamical properties of the Universe, affecting the time evolution of the metric, but in this Section we will treat them as purely kinematic parameters. They can be made into dimensionless parameters: the *matter density Ω_{M}*:

$$\Omega_{\mathrm{M}} = \frac{8\pi G \rho_0}{3 H_0^2}, \tag{C.5}$$

and Ω_Λ:

$$\Omega_\Lambda = \frac{\Lambda c^2}{3 H_0^2}, \tag{C.6}$$

where the subscripted "0" indicates again that the quantities are to be evaluated at the present epoch. A third density parameters Ω_k measures the curvature of space, and can be defined by:

$$\Omega_{\mathrm{M}} + \Omega_\Lambda + \Omega_k = 1. \tag{C.7}$$

These parameters completely determine the geometry of the Universe if it is homogeneous, isotropic and matter-dominated.

Several different models have been proposed throughout the years, each pushing the observational limits in different directions. The currently accepted paradigm is the $\Lambda-$CDM model, in which, as assumed in this work, $\Omega_{\mathrm{M}} \simeq 0.3$, $\Omega_\Lambda \simeq 0.7$ and $\Omega_k = 0$.

C.2 Comoving distance

The *comoving distance δD_C* between two nearby objects in the Universe is the distance between them which remains constant with epoch if the two

objects are moving with the *Hubble flow* (i.e. with the expanding Universe). In other words, it is the distance between them which would be measured with rulers at the time they are being observed (the *proper distance*) divided by the ratio of the scale factor of the Universe then to now; it is the proper distance multiplied by $(1 + z)$.

The total comoving distance D_C along the line of sight from the observer to a distant object is computed by integrating the infinitesimal distance contributions δD_C between nearby events from $z = 0$ to the redshift z of the source.

Let us define the function

$$E(z) = \sqrt{\Omega_M(1+z)^3 + \Omega_k(1+z)^2}, \tag{C.8}$$

which is proportional to the time derivative of the logarithm of the scale factor, $\dot{a}(t)/a(t)$. Since $dz = da$, $dz/E(z)$ is proportional to the time of flight of a photon traveling across the redshift interval dz, divided by the scale factor at that time. Since $c = \text{cost}$, this is a proper distance divided by the scale factor, which is the definition of the comoving distance. The total lie of sight comoving distance is therefore given by integrating

$$D_C = D_H \int_0^z \frac{dz'}{E(z')}. \tag{C.9}$$

The line of sight comoving distance is the fundamental distance measure in cosmography, since all other distance measures are quite simply derived in terms of it.

C.3 Angular diameter distance

The *angular diameter distance* D_A is defined as the ratio of the physical size of an object to its angular size in radians. It is commonly used to convert angular separations in telescope images into proper separations at the source.

The angular diameter distance is related, in a flat universe ($\Omega_k = 0$), to the line of sight comoving distance by

$$D_{\mathrm{A}} = \frac{D_M}{1+z}. \tag{C.10}$$

C.4 Comoving volume

The *comoving volume* V_{C} is the volume measure in which number densities of non evolving objects locked into the Hubble flow are constant with redshift. Since the derivative of the comoving distance with z is $1/E(z)$, the angular diameter distance converts a solid angle $\mathrm{d}\Omega$ into a proper area, and two factors $(1+z)$ convert a proper area into a comoving area, the comoving volume element in a solid angle $\mathrm{d}\Omega$ and redshift interval $\mathrm{d}z$ is:

$$\mathrm{d}V_{\mathrm{C}} = D_{\mathrm{H}} \frac{(1+z)^2 D_{\mathrm{A}}^2}{E(z)} \mathrm{d}\Omega \mathrm{d}z, \tag{C.11}$$

where, in a flat universe, the angular diameter distance is expressed as in Equation C.10.

Bibliography

Akiyama, M., Ohta, K., Yamada, T., et al. 2000, ApJ, 532, 700

Alexander, D. M., Bauer, F. E., Brandt, W. N., et al. 2003, AJ, 126, 539

Alexander, D. M., Bauer, F. E., Brandt, W. N., et al. 2011, ApJ, 738, 44

Alexander, D. M., & Hickox, R. C. 2012, New Astron. Rev., 56, 93

Antonucci, R. 1993, ARA&A, 31, 473

Arnouts, S., Cristiani, S., Moscardini, L., Matarrese, S., Lucchin, F., Fontana, A.,
    & Giallongo, E. 1999, MNRAS, 310, 540

Ballantyne, D. R. 2009, ApJ, 698, 1033

Barcons, X., Carrera, F. J., Ceballos, M. T., et al. 2007, A&A, 476, 1191

Barnes, J. E., & Hernquist, L. 1996, ApJ, 471, 115

Becker, R. H., White, R. L., & Helfand, D. J. 1995, ApJ, 450, 559

Beckmann, V., Soldi, S., Shrader, C. R., Gehrels, N., & Produit, N. ApJ, 652, 126

Best, P. N., Kaiser, C. R., Heckman, T. M., & Kauffmann, G. 2006, MNRAS, 368,
    L67

Bianchi, S., Maiolino, R., & Risaliti, G. 2012, AdAst, 17

Biggs, A. D., & Ivison, R. J. 2006, MNRAS, 371, 963

Bîrzan, L., Rafferty, D. A., McNamara, B. R., Wise, M. W., & Nulsen, P. E. J. 2004, ApJ, 607, 800

Bîrzan, L., McNamara, B. R., Nulsen, P. E. J., Carilli, C. L., & Wise, M. W. 2008, ApJ, 686, 859

Bonchi, A., La Franca, F., Melini, G., Bongiorno, A., & Fiore, F. 2013, MNRAS, in press (arXiv:1211.2688)

Bondi, M., Ciliegi, P., Schinnerer, E., Smolčić, V., Jahnke, K., Carilli, C., & Zamorani, G. 2008, ApJ, 681, 1129

Bongiorno, A., Merloni, A., Brusa, M., et al. 2012, MNRAS, in press (arXiv:1209.1640)

Bower, R. G., Benson, A. J., Malbon, R., Helly, J. C., Frenk, C. S., Baugh, C. M., Cole, S., & Lacey, C. G. 2006, MNRAS, 370, 645

Boyle, B. J., & Terlevich, R. J. 1998, MNRAS, 293, L49

Brandt, W. N., & Hasinger, G. 2005, ARA&A, 43, 827

Brightman, M., & Ueda, Y. 2012, MNRAS, 423, 70

Brinkmann, W., Laurent-Muehleisen, S. A., Voges, W., Siebert, J., Becker, R. H., Brotherton, M. S., White, R. L., & Gregg, M. D. 2000, A&A356, 445

Brunner, H., Cappelluti, N., Hasinger, G., Barcons, X., Fabian, A. C., Mainieri, V., & Szokoly, G. 2008, A&A, 479, 283

Brusa, M., Zamorani, G., Comastri, A., et al. 2007, ApJS, 172, 353

Brusa, M., Comastri, A., Gilli, R., et al. 2009a, ApJ, 693, 8

Brusa, M., Fiore, F., Santini, P., et al. 2009b, A&A, 507, 1277

Brusa, M., Civano, F., Comastri, A., et al. 2010, ApJ, 716, 348

Brusadin, V. 2003, PhD thesis, Università Roma Tre

Cappelluti, N., Brusa, M., Hasinger, G., et al. 2009, A&A, 497, 635

Cattaneo, A., Dekel, A., Devriendt, J.,Guiderdoni, B., & Blaizot, J. 2006, MNRAS, 370, 1651

Cattaneo, A., & Best, P. N. 2009, MNRAS, 395, 518

Churazov, E., Sazonov, S., Sunyaev, R. A., Forman, W., Jones, C., & Böhringer, H. 2005, MNRAS, 363, L91

Ciliegi, P., Zamorani, G., Hasinger, G., Lehmann, I., Szokoly, G., & Wilson, G. 2003, A&A, 398, 901

Cimatti, A., Daddi, E., Mignoli, M., et al. 2002, A&A, 381, L68

Ciotti, L., & Ostriker, J. P. 2007, AJ, 665, 1038

Ciotti, L., Ostriker, J. P., & Proga, D. 2010, AJ, 717, 708

Cirasuolo, M., Celotti, A., Magliocchetti, M., & Danese, L. 2003, MNRAS, 346, 447

Cocchia, F., Fiore, F., Vignali, C., et al. 2007, A&A, 466, 31

Condon, J. J., Cotton, W. D., Greisen E. W., Yin, Q. F., Perley, R. A., Taylor, G. B., & Broderick, J. J. 1998, AJ, 115, 1693

Condon, J. J., Cotton, W. D., & Broderick, J. J. 2002, AJ, 124, 675

Cowie, L. L., Songaila, A., Hu, E. M., & Cohen, J. G. 1996, AJ, 112, 839

Cowie, L. L., Barger, A. J., Hu, E. M., Capak, P., & Songaila, A. 2004, AJ, 127, 3137

Croom, S. M., Richards, G. T., Shanks, T., et al. 2009, MNRAS, 399, 1755

Croton, D. J., Springel, V., White, S. D., et al. 2006, MNRAS, 367, 864

Daddi, E., Alexander, D. M., Dickinson, M., et al. 2007, ApJ, 670, 173

Della Ceca, R., Maccacaro, T., Caccianiga, A., et al. 2004, A&A, 428, 383

Dey, A., Soifer, B. T., Desai, V., et al. 2008, AJ, 677, 943

Di Matteo, T., Springel, V., & Hernquist, L. 2005, Nature, 433, 604

Dickinson, M., % the GOODS Legacy Team 2001, A&AS, 198, 2501

Dong, X. Y., & De Robertis, M. M. 2006, AJ, 131, 1236

Elbaz, D., Daddi, E., Le Borgne, D., et al. 2007, A&A, 468, 33

Elvis, M., Civano, F., Vignali, C., et al. 2009, ApJS, 184, 158

Fabian, A. C., & Iwasawa, K. 1999, MNRAS, 303, L34

Falcke, H., & Biermann, P. L. 1995, A&A, 293, 665

Falcke, H., Körding, E., & Markoff, S. 2004, A&A, 2004, 414, 895

Fanaroff, B. L., & Riley, J. M. 1974, MNRAS, 167, 31P

Fasano, G., & Franceschini, A. 1987, MNRAS, 225, 155

Ferrarese, L., & Merritt, D. 2000, ApJ, 539, L9

Feruglio, C., Fiore, F., La Franca, F., et al. 2009, A&A, 488, 417

Fiore, F., Brusa, M., Cocchia, F., et al. 2003, A&A, 409, 79

Fiore, F., Grazian, A., Santini, P., et al. 2008, ApJ, 672, 94

Fiore, F., Puccetti, S., Brusa, M., et al. 2009, ApJ, 693, 447

Fiore, F., Puccetti, S., Grazian, A., et al. 2012, A&A, 537, A16

Franceschini, A., Hasinger, G., Miyaji, T., & Malquori, D. 1999, MNRAS, 310, L5

Fukugita, M., & Peebles, P. J. E. 2004, ApJ, 616, 643

Gebhardt, K., Bender, R., Bower, G., et al. 2000, ApJ, 539, L13

Georgantopoulos, I., Georgakakis, A., Rowan-Robinson, M., & Rovilos, E. 2008, A&A, 484, 671

Georgantopoulos, I., Rovilos, E., Xilouris, E. M., Comastri, A., & Akylas, A. 2011, A&A, 526, 86

Georgantopoulos, I. 2012, arXiv:1204.2173

Giacconi, R., Gursky, H., Paolini, F. R., & Rossi, B. B. 1962, Phys. Rev. Lett., 9, 439

Giavalisco, M., Ferguson, H. C., Koekemoer, A. M., et al. 2004, AJ, 600, L93

Gilli, R., Comastri, A., & Hasinger, G., A&A, 463, 79

Goldschmidt, P., Kukula, M. J., Miller, L., & Dunlop, J. S. 1999, ApJ, 511, 612

Graham, A. W. 2007, MNRAS, 379, 711

Graham, A. W., & Worley, C. C. 2008, MNRAS, 388, 1708

Granato, G. L., Silva, L., Monaco, P., Panuzzo, P., Salucci, P., De Zotti, G., & Danese, L. 2001, MNRAS, 324. 757

Granato, G. L., De Zotti, G., Silva, L., Bressan, A., & Danese, L. 2004, ApJ, 600, 580

Grazian, A., Fontana, A., Moscardini, L., et al. 2006, A&A, 453, 507

Grossan, B. A. 1992, PhD Thesis, Massachusetts Institute of Technology

Gültekin, K., Cackett, E. M., Miller, J. M., Di Matteo, T., Markoff, S., & Richstone, D. O. 2009, ApJ, 706, 404

Häring, N., & Rix, H.-W. 2004, ApJ, 604, L89

Hasinger, G., Miyaji, T., & Schmidt, M. 2005, A&A, 441, 417

Hasinger, G. 2008, A&A, 490, 905

Hawkins, M. R. S. 2004, A&A, 424, 519

Heinz, S., & Sunyaev, R. A. 2003, MNRAS, 343, L59

Heinz, S., Merloni, A., & Schwab, J. 2007, ApJ, 658, L9

Hogg, D. W. 1999, arXiv:9905.116

Houck, J. R., Soifer, B. T., Weedman, D., et al. 2005, ApJ, 622, L105

Ilbert, O., Arnouts, S., McCracken, H. J., et al. 2006, A&A, 457, 841

Ilbert, O., Capak, P., Salvato, M., et al. 2009, ApJ, 690, 1236

Ivezić, Ž., Menou, K., Knapp, G. R., et al. 2002, AJ, 124, 2364

Iwasawa, K., Gilli, R., Vignali, C., et al. 2012, 546, 84

Jarvis, M. J., & Rawlings, S. 2004 New Astron. Rev., 48, 1173

Jiang, L., Fan, X., Ivezić, Ž., Richards, G. T., Schneider, D. P., Strauss, M. A., & Kelly, B. C. 2007, ApJ, 656, 680

Koratkar, A., & Blaes, O. 1999, PASP, 111, 1

Körding, E. G., Jester, S., & Fender, R. 2008, MNRAS, 383, 277

Kormendy, J., & Richstone, D. 1995, ARA&A, 33, 581

Krolik, J. H. 1998, *Active Galactic Nuclei*, Princeton Series in Astrophysics

La Franca, F., Gregorini, L., Cristiani, S., de Ruiter, H., & Owen, F. 1994, AJ, 108, 1548

La Franca, F., Franceschini, A., Cristiani, S., & Vio, R. 1995, A&A, 299, 19

La Franca, F., & Cristiani, S. 1997, AJ, 113, 1517

La Franca, F., Fiore, F., Vignali, C., et al. 2002, ApJ, 570, 100

La Franca, F., Fiore, F., Comastri, A., et al. 2005, ApJ, 635, 864

La Franca, F., Melini, G., & Fiore, F. 2010, ApJ, 718, 368

Lampton, M., Margon, B., & Bowyer, S. 1976, ApJ, 208, 177

Laor, A., & Behar, E. 2008, MNRAS, 390, 847

Le Floc'h, E., Aussel, H., Ilbert, O., et al. 2009, ApJ, 703, 222

Li, Z.-Y., Wu, X.-B., & Wang, R. 2008 ApJ, 688, 826

Luo, B., Bauer, F. E., Brandt, W. N., et al. 2008, ApJS, 179, 19

Luo, B., Brandt, W. N., Xue, Y. Q., et al. 2011, AJ, 740, 37

Madau, P., Ferguson, H. C., Dickinson, M. E., Giavalisco, M., Steidel C. C., & Fruchter A. 1996, MNRAS, 283, 1388

Magnelli, B., Elbaz, D., Chary, R. R., Dickinson, M., Le Borgne, D., Frayer, D. T., & Willmer, C. N. A. 2011, A&A, 528, A35

Magorrian, J., Tremaine, S., Richstone, D., et al. 1998, AJ, 115, 2285

Marconi, A., & Hunt, L. K. 2003, ApJ, 589, L21

Marconi, A., Risaliti, G., Gilli, R., Hunt, L. K., Maiolino, R., & Salvati, M. 2004, MNRAS, 351, 169

Marshall, H. L., Tananbaum, H., Huchra, J. P., Zamorani, G., Braccesi, A., & Zitelli, V. 1983, ApJ, 269, 42

Martinez-Sansigre, A., Rawlings, S., Lacy, M., Fadda, D., Marleau, F. R., Simpson, C., Willott, C. J., & Jarvis, M. J. 2005, Nature, 436, 666

Marulli, F., Bonoli, S., Branchini, E., Moscardini, L., & Springel, V. 2008, MN-RAS, 385, 1846

Mathez, G. 1976, A&A, 53, 15

Matute, I., La Franca, F., Pozzi, F., Gruppioni, C., Lari, C., & Zamorani, G. 2006, A&A, 451, 443

Mauch, T., Murphy, T., Buttery, H. J., Curran, J., Hunstead, R. W., Piestrzynski, B., Robertson, J. G., & Sadler, E. M. 2003, MNRAS, 342, 1117

McCracken, H. J., Capak, P., Salvato, M., et al. 2010, ApJ, 708, 202

McNamara, B. R., Wise, M., Nulsen, P. E. J., et al. 2000, ApJ, 534, L135

Menci, N., Fiore, F., Perola, G. C., & Cavaliere, A. 2004, ApJ, 606, 58

Menci, N., Fontana, A., Giallongo, E., & Salimbeni, S. 2005, ApJ, 632, 49

Menci, N., Fiore, F., Puccetti, S., & Cavaliere, A. 2008, ApJ, 686, 219

Merloni, A., Heinz, S., & Di Matteo, T. 2003, MNRAS, 345, 1057

Merloni, A., & Heinz, S. 2007, MNRAS, 381, 589

Merloni, A., & Heinz, S. 2008, MNRAS, 388, 1011

Merloni, A., Bongiorno, A., Bolzonella, M., et al. 2010, ApJ, 708, 137

Merloni, A., & Heinz, S. 2012, arXiv:1204.4265

Merritt, D., & Ferrarese, L. 2001, MNRAS, 320, L30

Middelberg, E., Norris, R. P., Cornwell, T. J., et al. 2008, AJ, 135, 1276

Miller, L., Peacock, J. A., & Mead, A. R. G. 1990, MNRAS, 244, 207

Miller, N. A., Fomalont E. B., Kellermann, K. I., Mainieri, V., Norman, C., Padovani, P., Rosati, P., & Tozzi, P. 2008, ApJS, 179, 114

Monaco, P., Salucci, P., & Danese, L. 2000, MNRAS, 311, 279

Mosleh, M., Williams, R. J., Franx, M., et al. 2012, ApJ, 756, L12

Noeske, K. G., Weiner, B. J., Faber, S. M., et al. 2007, ApJ, 660, L43

Owen, F. N., & Morrison, G. E. 2008, ApJ, 136, 1889

Padovani, P. 1993, MNRAS, 263, 461

Padovani, P., Mainieri, V., Tozzi, P., Kellermann, K. I., Fomalont, E. B., Miller, N., Rosati, P., & Shaver, P. 2009, ApJ, 694, 235

Panessa, F., Barcons, X., Bassani, L., Cappi, M., Carrera, F. J., Ho, L. C., & Pellegrini, S. 2007, A&A, 467, 519

Peacock, J. A. 1983, MNRAS, 202, 615

Peterson, B. M. 1997, *An Introduction to Active Galactic Nuclei*, Cambridge University Press

Plotkin, R. M., Markoff, S., Kelly, B. C., Körding, E., & Anderson, S. F. 2012, MNRAS, 419, 267

Polletta, M., Tajer, M., Maraschi, L., et al. 2007, ApJ, 663, 81

Pozzi, F., Vignali, C., Comastri, A., et al. 2007, A&A, 468, 603

Pozzi, F., Vignali, C., Gruppioni, C., et al. 2012, MNRAS, 423, 1909

Puccetti. S., Fiore, F., D'Elia, V., et al. 2006, A&A, 457, 501

Ranalli, P., Comastri, A., & Setti, G. 2003, 399, 39

Richards, E. A. 2000, ApJ, 533, 611

Risaliti, G., & Elvis, M. 2004, Astrop. and Space Sci. Lib., 308, 187

Rodighiero, G., Vaccari, M., Franceschini, A., et al. 2010, A&A, 515, 8

Sacchi, N. 2008, Ph.D. Thesis, Università Roma Tre

Sacchi, N., La Franca, F., Feruglio, C., et al. 2009, ApJ, 703, 1778

Salvato, M., Hasinger, G., Ilbert, O., et al. 2009, ApJ, 690, 1250

Sanders, D. B., Salvato, M., Aussel, H., et al. 2007, ApJS, 172, 86

Santini, P., Fontana, A., Grazian, A., et al. 2009, A&A, 504, 751

Sazonov, S., Revnivtsev, M., Krivonos, R., Churazov, E., & Sunyaev, R. 2007, A&A, 462, 57

Schinnerer, E., Smolčić, V., Carilli, C. L., et al. 2007, ApJS, 172, 46

Schmidt, M. 1968, ApJ, 151, 393

Scoville, N., Aussel, H., Brusa, M., et al. 2007, ApJS, 172, 1

Seymour, N., Dwelly, T., Moss, D., et al. 2008, MNRAS, 386, 1695

Shankar, F., Cavaliere, A., Cirasuolo, M., & Maraschi, L. 2008, ApJ, 676, 131

Silva, L., Maiolino, R., & Granato, G. L. 2004, MNRAS, 355, 973

Skrutskie, M. F., Cutri, R. M., Stiening, R., et al. 2006, AJ, 131, 1163

Smolčić, V., Zamorani, G., Schinnerer, E., et al. 2009, ApJ, 696, 24

Soltan, A. 1982, MNRAS, 200, 115

Sutherland, W., & Saunders, W. 1992, MNRAS, 259, 413

Tozzi, P., Rosati, P., Nonino, M., et al. 2001, ApJ, 562, 42

Tozzi, P., Mainieri, V., Rosati, P., et al. 2009, ApJ, 698, 740

Treister, E., & Urry, C. M. 2005, ApJ, 630, 115

Treister, E., & Urry, C. M., 2006, ApJ, 652, L79

Treister, E., Urry, C. M., & Virani, S. 2009, ApJ, 696, 110

Treister, E., Urry, C. M., Schawinski, K., Cardamone, C. N., & Sanders, D. B. 2010, ApJ, 722, L238

Trouille, L., Barger, A. J., Cowie, L. L., Yang, Y., & Mushotzky, R. F. 2008, 179, 1

Trump, J. R., Impey, C. D., Elvis, M., et al. 2009, ApJ, 696, 1195

Tueller, J., Mushotzky, R. F., Barthelmy, S., Cannizzo, J. K., Gehrels, N., Markwardt, C. B., Skinner, G. K., & Winter, L. M. 2008, ApJ, 681, 113

Ueda, Y., Takahashi, T., Inoue, H., et al. 1999, ApJ, 518, 656

Ueda, Y., Akiyama, M., Ohta, K., & Miyaji, T. 2003, ApJ, 598, 886

Urry, C. M., & Padovani, P. 1995, PASP, 107, 803

Vanzella, E., Cristiani, S., Dickinson, M., et al. 2005, A&A, 434, 53

Visnovsky, K. L., Impey, C. D., Foltz, C. B., Hewett, P. C., Weymann, R. J., & Morris, S. L. 1992, ApJ, 391, 560

Watanabe, C., Ohta, K., Akiyama, M., & Ueda, Y. 2004, ApJ, 610, 128

Willott, C. J., Rawlings, S., Blundell, K. M., & Lacy, M. 1999, MNRAS, 309, 1017

Wilman, R. J., Miller, L., Jarvis, M. J., et al. 2008, MNRAS, 388, 1335

White, R. L., Becker, R. H., Helfand, D. J., & Gregg, M. D. 1997, ApJ, 475, 479

Wolf, C., Meisenheimer, K., Rix, H.-W., Borch, A., Dye, S., & Kleinheinrich, M. 2003, A&A, 401, 73

Wuyts, S., Labbé, I., Schreiber, N. M. F., Franx, M., Rudnick, G., Brammer, G. B., & van Dokkum, P. G. 2008, ApJ, 689, 653

Xue, Y. Q., Luo, B., Brandt, W. N., et al. 2011, ApJS, 195, 10

Yu, Q., & Tremaine, S. 2002, MNRAS, 965

*"Because my duty
was always to beauty
and that was my crime"*